

**Measurement of the Oscillation Frequency of  $B_s$  Mesons  
in the Hadronic Decay Mode  $B_s \rightarrow \pi D_s(\phi\pi)X$   
with the DØ Detector at the Fermilab Tevatron Collider**

**Gernot A. Weber  
Institut für Physik  
Johannes Gutenberg-Universität Mainz**

A thesis submitted for the degree of  
“Doctor rerum naturalium”  
of the Johannes Gutenberg-Universität in Mainz

Mainz 2009



## Abstract

The standard model (SM) of particle physics is a theory, describing three out of four fundamental forces. In this model the Cabibbo-Kobayashi-Maskawa (CKM) matrix describes the transformation between the mass and weak eigenstates of quarks. The matrix properties can be visualized as triangles in the complex plane. A precise measurement of all triangle parameters can be used to verify the validity of the SM. The least precisely measured parameter of the triangle is related to the CKM element  $|V_{td}|$ , accessible through the mixing frequency (oscillation) of neutral  $B$  mesons, where mixing is the transition of a neutral meson into its anti-particle and vice versa. It is possible to calculate the CKM element  $|V_{td}|$  and a related element  $|V_{ts}|$  by measuring the mass differences  $\Delta m_d$  ( $\Delta m_s$ ) between neutral  $B_d$  and  $\bar{B}_d$  ( $B_s$  and  $\bar{B}_s$ ) meson mass eigenstates. This measurement is accomplished by tagging the initial and final state of decaying  $B$  mesons and determining their lifetime. Currently the Fermilab Tevatron Collider (providing  $p\bar{p}$  collisions at  $\sqrt{s}=1.96$  TeV) is the only place, where  $B_s$  oscillations can be studied.

The first selection of the “golden”, fully hadronic decay mode  $B_s \rightarrow \pi D_s(\phi\pi)X$  at DØ is presented in this thesis. All data, taken between April 2002 and August 2007 with the DØ detector, corresponding to an integrated luminosity of  $\int \mathcal{L} dt = 2.8 \text{ fb}^{-1}$  is used. The oscillation frequency  $\Delta m_s$  and the ratio  $|V_{td}|/|V_{ts}|$  are determined as

$$\begin{aligned}\Delta m_s &= (16.6^{+0.5}_{-0.4}(\text{stat})^{+0.4}_{-0.3}(\text{sys})) \text{ ps}^{-1}, \\ |V_{td}|/|V_{ts}| &= 0.213^{+0.004}_{-0.003}(\text{exp}) \pm 0.008(\text{theor}).\end{aligned}$$

These results are consistent with the standard model expectations and no evidence for new physics is observable.





## Kurzzusammenfassung

Das Standard-Modell der Teilchenphysik formuliert das Zusammenspiel von drei der vier fundamentalen Kräfte. In diesem Modell beschreibt die Cabibbo-Kobayashi-Maskawa-Matrix (CKM-Matrix) die Transformation von Masseneigenzuständen und schwachen Eigenzuständen der Quarks. Diese Matrix kann durch Dreiecke in der komplexen Ebene visualisiert werden. Eine Validierung des Standard-Modells kann durch präzise Messungen aller Dreiecksparameter stattfinden. Der am wenigsten genau gemessene Parameter in diesem Zusammenhang ist das CKM-Matrixelement  $|V_{td}|$ . Es ist zugänglich über die Mischungsfrequenz von neutralen  $B$ -Mesonen, wobei der Begriff Mischung den Übergang von Mesonen in ihre Anti-Teilchen bzw. die umgekehrte Richtung bezeichnet. Die Bestimmung der Massendifferenzen  $\Delta m_d$  und  $\Delta m_s$  zwischen den Masseneigenzuständen von neutralen  $B_d$ - und  $B_s$ -Mesonen ermöglicht die Berechnung der CKM-Matrixelemente  $|V_{td}|$  und  $|V_{ts}|$ . Für diese Messung müssen der Anfangs- und der Endzustand markiert und die Lebensdauer des zerfallenden  $B$ -Mesons bestimmt werden. Momentan ist der Tevatron-Speicherring am Fermilab der einzige Ort, an dem das Studium von  $B_s$ -Oszillationen möglich ist. Dort werden Protonen und Anti-Protonen bei einer Schwerpunktsenergie von  $\sqrt{s}=1,96$  TeV zur Kollision gebracht.

Diese Analyse präsentiert die erste Selektion des hadronischen Zerfallskanals  $B_s \rightarrow \pi D_s(\phi\pi)X$  des DØ-Experiments. Verwendet wird der komplette Datensatz mit einer integrierten Luminosität von  $\int \mathcal{L} dt = 2.8 \text{ fb}^{-1}$ , der zwischen April 2002 und August 2007 aufgezeichnet wurde. Die Oszillationsfrequenz  $\Delta m_s$  und das Verhältnis  $|V_{td}|/|V_{ts}|$  wurden zu

$$\begin{aligned}\Delta m_s &= (16.6^{+0.5}_{-0.4}(\text{stat})^{+0.4}_{-0.3}(\text{sys})) \text{ ps}^{-1}, \\ |V_{td}|/|V_{ts}| &= 0.213^{+0.004}_{-0.003}(\text{exp}) \pm 0.008(\text{theor})\end{aligned}$$

bestimmt. Diese Resultate sind im Einklang mit den Vorhersagen des Standard-Modells und zeigen keine Hinweise auf neue Physik.



## Contents

<b>Introduction</b>	<b>1</b>
<b>1. Beauty in the Standard Model</b>	<b>3</b>
1.1. Symmetries in Physics . . . . .	3
1.2. The Standard Model . . . . .	4
1.2.1. Quarks and Leptons . . . . .	5
1.2.2. Bosons and Interactions . . . . .	5
1.2.3. Mesons and Baryons . . . . .	9
1.2.4. Weak Interactions of Quarks . . . . .	10
1.3. Mixing of Neutral Mesons . . . . .	13
1.4. Production of B Mesons at Hadron Colliders . . . . .	16
1.5. $B_s$ Mixing in the Standard Model . . . . .	19
<b>2. Principle of the Measurement</b>	<b>21</b>
2.1. Signal Selection . . . . .	21
2.2. Initial State Flavor Tagging . . . . .	23
2.3. Measurement of the Proper Decay Time . . . . .	24
2.4. Measurement of $\Delta m_q$ . . . . .	25
2.5. Extraction of $ V_{td} / V_{ts} $ . . . . .	27
<b>3. The Fermilab Tevatron Collider and the DØ Detector</b>	<b>29</b>
3.1. The Fermilab Tevatron Collider . . . . .	29
3.2. The DØ Detector . . . . .	31
3.2.1. Tracking System . . . . .	33
3.2.2. Calorimeter . . . . .	36
3.2.3. Muon System . . . . .	37
<b>4. The DØ Trigger System</b>	<b>39</b>
4.1. Functional Principle of the Three Level Trigger System . . . . .	39
4.1.1. The First Trigger Level . . . . .	41
4.1.2. The Second Trigger Level . . . . .	43
4.1.3. The Third Trigger Level . . . . .	43

4.1.4. Trigger Menu and Trigger Rates . . . . .	45
4.2. Trigger Strategies for $B$ Physics and Trigger Studies . . . . .	46
4.2.1. Level 1 Trigger Studies . . . . .	46
4.2.2. Level 2 Trigger Studies . . . . .	47
4.2.3. Level 3 Trigger Studies . . . . .	48
<b>5. Reconstruction and Monte Carlo Simulation</b>	<b>51</b>
5.1. Reconstruction Software . . . . .	51
5.1.1. d0reco . . . . .	51
5.1.2. BANA and AATrack . . . . .	52
5.2. Track and Vertex Reconstruction . . . . .	52
5.3. Muon Reconstruction . . . . .	54
5.4. Monte Carlo Simulation . . . . .	54
5.5. Monte Carlo Samples . . . . .	56
5.6. Dataset . . . . .	57
<b>6. Signal Selection</b>	<b>59</b>
6.1. Selection of Hadronic $B_s$ Decays . . . . .	59
6.1.1. Selection Principle and Preselection . . . . .	59
6.1.2. Final Selection . . . . .	65
6.1.3. Performance of Selection . . . . .	72
6.2. Selection of Hadronic $B_d$ Decays . . . . .	73
6.2.1. Preselection . . . . .	73
6.2.2. Final Selection . . . . .	73
<b>7. Lifetime Measurement of <math>B_d</math> and <math>B_s</math> Mesons</b>	<b>77</b>
7.1. Lifetime and Decay Length . . . . .	77
7.2. Extraction of the Lifetime Using an Unbinned Maximum Likelihood Fit . . . . .	77
7.3. Input Parameters to the Fit . . . . .	79
7.3.1. K-Factor . . . . .	79
7.3.2. Resolution of the Visible Proper Decay Length . . . . .	79
7.3.3. Background . . . . .	81
7.3.4. Selection Efficiency . . . . .	82
7.4. Results . . . . .	83
7.4.1. Applying the Fit to a Monte Carlo Sample . . . . .	83
7.4.2. Applying the Fit to Data . . . . .	84
7.4.3. Systematic Uncertainties . . . . .	85
7.4.4. Final Results of the Lifetime Measurement . . . . .	86
<b>8. Initial and Final State Flavor Tagging</b>	<b>87</b>
8.1. Opposite Side Tagging Classes . . . . .	87
8.1.1. Muon Tagging . . . . .	87
8.1.2. Secondary Vertex Tagging . . . . .	88
8.1.3. Electron Tagging . . . . .	88
8.1.4. Event Charge Tagging . . . . .	89
8.1.5. Combined Tagging Variable . . . . .	89
8.2. Tagging Performance . . . . .	89
8.2.1. Selection of the Decay $B_d \rightarrow \mu^+ \nu_\mu \bar{D}^0 X$ . . . . .	90
8.2.2. Measurement of the Tagging Performance . . . . .	90

8.2.3. Measurement of the Oscillation Frequency $\Delta m_d$ . . . . .	92
<b>9. Extraction of the Oscillation Frequency <math>\Delta m_s</math></b>	<b>93</b>
9.1. Method to Extract the Oscillation Frequency $\Delta m_s$ by Using an Unbinned Likelihood Fit	93
9.2. Checking the Fit with Monte Carlo Simulation . . . . .	95
9.3. Measurement of $\Delta m_d$ . . . . .	96
9.4. Measurement of $\Delta m_s$ . . . . .	97
9.5. Systematic Uncertainties . . . . .	99
9.6. Final Results for the Measurement of $\Delta m_d$ and $\Delta m_s$ . . . . .	100
9.7. Impact on $ V_{td} / V_{ts} $ . . . . .	100
<b>10. Summary and Outlook</b>	<b>103</b>
<b>A. Muon Trigger Qualities</b>	<b>107</b>
A.1. Level-1 Muon Qualities . . . . .	107
A.2. Level-2 Muon Qualities . . . . .	107
A.2.1. Quality for Stubs . . . . .	107
A.2.2. Quality for Muons . . . . .	108
<b>B. Monte Carlo Files (p20)</b>	<b>109</b>
B.1. dØrunjob Files . . . . .	109
B.2. dØmess Files . . . . .	110
<b>C. Technical Implementation of the Likelihood</b>	<b>111</b>
<b>Bibliography</b>	<b>113</b>
<b>List of Figures</b>	<b>117</b>
<b>List of Tables</b>	<b>120</b>
<b>Acknowledgements</b>	<b>122</b>
<b>Curriculum Vitae</b>	<b>125</b>



## Introduction

“Nearly everything has already been discovered and all that remains is to fill a few holes like the radiation of blackbodies [1]”. Luckily Max Planck was not discouraged by this proposition of his professor Philipp von Jolly at university in the late 19th century. He made revolutionary discoveries and the knowledge, gained in the last 100 years, was very important for the understanding of the universe as it is known today. For example the concept of particle accelerators was developed in the last century. It offered a big field for discoveries and concluded in the standard model (SM) of particle physics, which describes the interaction of fundamental particles quite well and has resisted rigorous testing for the last couple of decades. However, not all phenomena, for example dark matter and the matter-anti-matter asymmetry observed in the universe, can be explained by this model. It is one of the biggest challenges of particle physics to understand the nature of dark matter, which has a much bigger contribution to the universe than the normal matter [2]. Symmetries and conservation laws, which have always been among the main principles of physics, predict the creation of particles and anti-particles in pairs only. Therefore, until about 50 years ago, physics was assumed to be invariant under charge (C) and parity (P) conjugation and did not provide an explanation of how our universe evolved, as obviously today more matter than anti-matter exists. In 1964, however, physicists discovered that the CP symmetry is violated in weak force interactions [3].

The Cabibbo-Kobayashi-Maskawa (CKM) matrix [4], [5] describes the relation between weak and flavor eigenstates of the quarks. The matrix element  $|V_{td}|$  [6] is the least known element. It is accessible by studying the transition of neutral  $B$  mesons to their anti-particles and vice versa, a behavior which is also known as mixing [7]. It is caused by the mass difference between the heavy and light eigenstates. Since the observation of flavor mixing in the  $B_d$  system by the ARGUS collaboration [8] this topic has been studied intensively and was well measured at the  $B$ -factories BaBar [9] and Belle [10]. However, the relationship between  $\Delta m_d$  and  $|V_{td}|$  allows a determination of  $|V_{td}|$  with an accuracy of only 12% [11], as it contains nonperturbative QCD effects. By measuring the mass differences  $\Delta m_d$  and  $\Delta m_s$  and calculating their ratio most of these uncertainties cancel out, allowing a determination of  $|V_{td}|/|V_{ts}|$  with an accuracy of 4% [11]. The Tevatron Collider [12] at the Fermi National Accelerator Laboratory is currently the only place worldwide where mixing in the  $B_s$  system can be observed, allowing to measure the CKM matrix element  $|V_{td}|$  precisely. A deviation of this measurement from the SM prediction would be an evidence of new physics and could help in understanding problems like the existence of dark matter.

Chapter 1 gives a brief introduction to the standard model of particle physics and explains the importance of  $B_s$  mixing. It is followed by the main principles (Chapter 2) of how to measure the oscillation frequency  $\Delta m_s$  at hadron colliders, such as the Fermilab Tevatron, which is described in detail in Chapter 3. The DØ detector, which was used to collect the data the analysis in this thesis is based on is also described in Chapter 3. Afterwards the principles on the identification and recording of interesting  $B$  physics events are discussed in Chapter 4. The reconstruction of the events is presented in Chapter 5, where the used Monte Carlo simulation and the software packages provided by the DØ  $B$  physics group are also introduced. For further measurements the signal has to be selected (Chapter 6) out of the recorded dataset. In order to determine the oscillation frequency a lifetime measurement has to be performed (Chapter 7) and the initial and final states have to be tagged (Chapter 8). The extraction of the oscillation frequency  $\Delta m_s$  and the measurement of the CKM element ratio  $|V_{td}|/|V_{ts}|$  is presented in Chapter 9, where consistency checks and systematic uncertainties are shown. Finally, a summary and an outlook for future experiments are given in chapter 10.



## Beauty in the Standard Model

The standard model (SM) of particle physics describes the state-of-the-art knowledge of the fundamental forces and elementary particles of matter. An overview of symmetries, as they appear in nature is briefly given (Section 1.1). It is followed by an explanation of the elementary particles: quarks and leptons (Section 1.2.1). Afterwards, the fundamental forces and their force carriers – the bosons – are described in detail. The interaction of quarks is introduced in Section 1.2.4, which leads to a theoretical description of the CKM<sup>1</sup> matrix. The main principles of neutral meson mixing are explained in Section 1.3, while the specialties and the measurement at hadron colliders will be described afterwards in Section 1.4.

### 1.1. Symmetries in Physics

Conservation laws like the conservation of energy or momentum have always been very important in physics and are directly related to symmetries appearing in nature. Even the most simple creatures, like the single-celled radiolarian (left-hand side of Figure 1.1) have a symmetric shape. Another example is the baryon octet (right-hand side of Figure 1.1), where the baryons are ordered by the quantum numbers isospin  $I_3$  and strangeness  $S$  and build a simple symmetric shape. In 1915 Emmy Noether postulated a theorem [13], which stated that “every symmetry gives a conserved quantity”. This means, that every physical experiment that has the same outcome regardless of place or time has a Lagrangian, which is symmetric under continuous translations in space and time. This leads to the conservation laws of linear momentum and energy within this system

$$\frac{\partial}{\partial q} \mathcal{L}(q, \dot{q}, t) = 0 \quad \text{and} \quad \frac{\partial}{\partial t} \mathcal{L}(q, \dot{q}, t) = 0. \quad (1.1)$$

Similarly, a system that behaves the same regardless of its orientation in space exhibits conservation of angular momentum. The most important discrete symmetries<sup>2</sup> are the parity transformation (P), the time inversion (T) and the charge conjugation (C). They deal with the questions, respectively, of

<sup>1</sup>Cabibbo-Kobayashi-Maskawa

<sup>2</sup>A discrete symmetry is a symmetry under the transformations of a group, with a discrete topology.

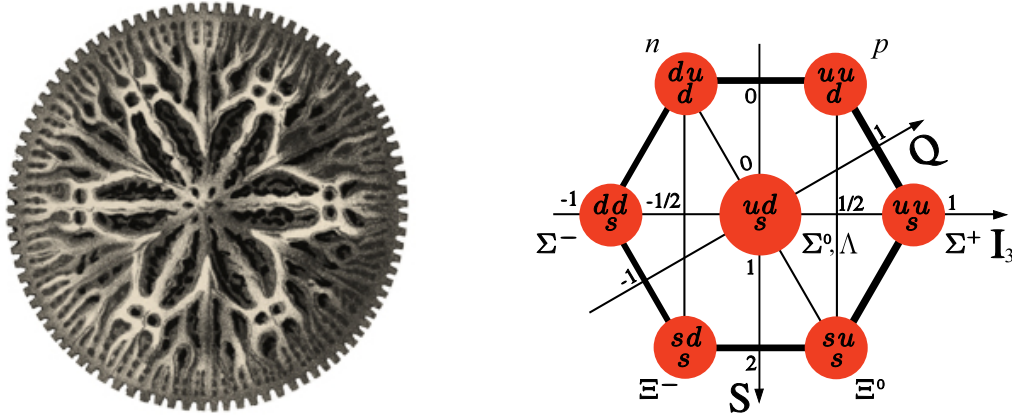


**Figure 1.1:** Symmetries in nature. On the left side a radiolarian is shown, a single-celled organism living on the bottom of the sea and occurring in amazing variety. The baryon octet as an example of symmetries in particle physics is shown on the right.

whether a particle behaves in a different way if its spatial configuration is reversed (P), if the direction of time is made to run backwards instead of forward (T), or if matter particles are changed to antimatter (C).

By expanding the invariant from  $n$ -dimensional Lie groups to infinite dimensional groups, this theory evolves to a gauge theory<sup>3</sup> for the standard model. Therefore, the invariance of particle fields under local gauge transformations and the underlying symmetry groups are very important. The symmetry group in the standard model is  $SU(3)_C \times SU(2)_L \times U(1)_Y$ . The group  $SU(3)_C$  describes the strong interaction (Section 1.2.2) and its interaction particles – the gluons – which couple to the color charge  $C^4$ . The electroweak unification is accomplished under an  $SU(2)_L \times U(1)_Y$  gauge group.

## 1.2. The Standard Model

The standard model is a theory, describing three out of four fundamental forces. It was excessively tested during the last few decades and nearly all these impressively precise measurements were correctly predicted by the model. Today, there is only one jigsaw piece still undiscovered, the Higgs boson, which is predicted by the standard model and explains the difference between the massless photon, which mediates electromagnetism, and the relatively massive  $W$  and  $Z$  bosons, which mediate the weak force. However, there are still missing parts. The standard model does not attempt to explain gravity, and it is unknown how to combine quantum field theory which is used for the standard model with general relativity which is the best physical model of gravity. Phenomena like the matter-anti-matter asymmetry or the existence of dark matter are also not explainable by the standard model.

<sup>3</sup>Gauge theory is a quantum field theory where the Lagrangian is invariant under certain transformations.

<sup>4</sup>The color charge explains how quarks could coexist inside some hadrons in otherwise identical states and still satisfy the Pauli exclusion principle.

Family	Charge	1st generation	2nd generation	3rd generation
Quarks	$+\frac{2}{3}$	u	c	t
		up	charm	top
		$m = (1.5 \text{ to } 3.0) \text{ MeV}/c^2$	$m = (1.25 \pm 0.09) \text{ MeV}/c^2$	$m = (174.2 \pm 3.3) \text{ GeV}/c^2$
	$+\frac{2}{3}$	d	s	b
		down	strange	beauty
		$m = (3 \text{ to } 7) \text{ MeV}/c^2$	$m = (95 \pm 25) \text{ MeV}/c^2$	$m = (4.20 \pm 0.07) \text{ GeV}/c^2$
Leptons	0	$\nu_e$	$\nu_\mu$	$\nu_\tau$
		electron-neutrino	muon-neutrino	tau-neutrino
		$m < 225 \text{ eV}/c^2$	$m < 0.19 \text{ MeV}/c^2$	$m < 18.2 \text{ MeV}/c^2$
	-1	e	$\mu$	$\tau$
		electron	muon	tau
		$m = (0.511 \pm 4e^{-8}) \text{ MeV}/c^2$	$m = (105.7 \pm 9e^{-6}) \text{ MeV}/c^2$	$m = (1776.99^{+0.29}_{-0.26}) \text{ MeV}/c^2$

**Table 1.1:** Overview of all fermions, which are classified into two families. Each family has three generations. All masses are world-averages [6].

### 1.2.1. Quarks and Leptons

For much of the 20th century it was believed, that matter is built of electrons, protons and neutrons as elementary particles. As it turned out, this is true for electrons, but protons and neutrons showed a sub-structure in deep inelastic scattering experiments [14]. In 1969 Richard Feynman postulated the parton model to explain this behavior [15]. Later on these particles were called quarks by Gell-Mann and Ne’eman [16]. Nowadays six different quarks are known. Their characteristics lead to a classification into three generations (Table 1.1), where all generations consist of two quarks, having either an electrical charge of  $+\frac{2}{3}$  for up-type quarks or  $-\frac{1}{3}$  for down-type quarks. The last quark – the top-quark – was found in 1995 at the Fermilab Tevatron Collider [17], [18].

It turned out that this classification is also true for the electron, having two similar particles – the muon and the tau – which are all combined into the leptons, all having charge  $-1$ . All three charged leptons have partners with neutral charge – the neutrinos. Table 1.1 shows an overview of all quarks and leptons, which are also known as fermions. All fermions are spin- $\frac{1}{2}$  particles. There is an anti-particle for every fermion, which has the same mass, but negative additive quantum numbers, like charge, lepton and baryon number.

### 1.2.2. Bosons and Interactions

In the standard model the three fundamental forces – electromagnetic, weak and strong – are used to describe the interactions between particles. The weak interaction is responsible for some phenomena at the scales of the atomic nucleus, such as beta decay. It is the only known interaction in which parity is not conserved. While it also violates  $CP^5$ , it does conserve  $CPT^6$ . Electromagnetism and weak interactions are unified in the electroweak interaction. The strong interaction keeps the positive protons in the nucleus in place.

<sup>5</sup> $CP$ : Application of the charge and parity operator one after another.

<sup>6</sup> $CPT$ : In addition to  $CP$ , the time operator is also taken into account.

## The Strong Interaction

The strong interaction, which is described by QCD<sup>7</sup> relies on the symmetry group  $SU(3)_C$ , where the  $C$  characterizes the color charge. This quantum number was introduced by Oscar W. Greenberg [19] to explain how quarks could coexist inside some hadrons in otherwise identical states and still satisfy the Pauli exclusion principle. The Lagrange density  $\mathcal{L}_{QCD}$  of the strong interaction can be written as

$$\mathcal{L}_{QCD} = \bar{q}\gamma_\mu D^\mu q - G_{\mu\nu}^a G_a^{\mu\nu}, \quad (1.2)$$

with the covariant derivative

$$D_\mu = i\partial_\mu - g_s T^a \cdot G_\mu^a \quad (1.3)$$

and the field intensity

$$G_{\mu\nu}^a = \partial_\mu G_\nu^a - \partial_\nu G_\mu^a - g_s f_{abc} G_\mu^b G_\nu^c, \quad (1.4)$$

where  $G_\mu^a$  are the gluon fields. The coupling strength is characterized as  $g_s$  and  $f_{abc}$  ( $a, b, c = 1, 2, \dots, 8$ ) are the structural constants of the strong interaction. The color charge appears in triplets and the quarks as well as the gluons carry color charge. The gluons are represented in a color octet and can interact with themselves. Based on this self interaction, the coupling constant increases with small quantum scales. Therefore quarks and gluons are not observed as free particles. They only appear color neutral in mesons, which are structures build of a quark and an anti-quark, or in baryons, made up of three differently colored quarks. Because of the strength of the coupling only effective theories or phenomenological methods can be used for small momentum transfers. On the other hand, at small distances the coupling strength nearly disappears, therefore a perturbative ansatz can be used.

## The Electroweak Interaction

Although the electromagnetic and weak force appear very different at everyday low energies, the theory describes them as two different aspects of the same force. They merge into a single electroweak force above the unification energy ( $\mathcal{O}(100 \text{ GeV})$ ). The relevant symmetry group for the electroweak interaction is a combination of the special unitary group  $SU(2)_L$  and the unitary group  $U(1)_Y$ . As only left-handed<sup>8</sup> fermions take part in weak interactions, the index  $L$  is used. Left-handed fermions can be illustrated as isospin-doublets with the weak isospin  $|\vec{T}| = \frac{1}{2}$  and therefore can appear in the states  $T_3 = \pm \frac{1}{2}$ . In contrast the right-handed fermions are singlet states with the weak isospin  $|\vec{T}| = T_3 = 0$ . The hyper-charge  $Y$  is the generator of the group  $U(1)_Y$ . The hyper-charge combines the electric charge with the third isospin component and can be calculated through the Gell-Mann-Nishijima relation  $Q/e = T_3 + Y/2$  [20], [21]. Within a multiplet, the hyper-charge for all particles is identical.

As the Lagrange density  $\mathcal{L}_{EW}$  needs to be invariant under transformations of the group  $SU(2)_L \times U(1)_Y$ , three vector-fields are obtained, which form an iso-triplet and couple to the weak isospin with the coupling strength  $g$ . Additionally there is a single vector-field  $B_\mu$ , which couples with  $g'$  to the hyper-charge. Therefore, the Lagrange density is

$$\mathcal{L}_{EW} = \bar{\psi}\gamma_\mu D^\mu \psi - \frac{1}{4} [W_{\mu\nu} W^{\mu\nu} + B_{\mu\nu} B^{\mu\nu}], \quad (1.5)$$

<sup>7</sup>Quantum Chromo Dynamics

<sup>8</sup>Left-handed refers to the chirality. A system is left-handed, if the directions of spin and momentum are opposite and right-handed, if both vectors have the same direction.

with the covariant derivative

$$D_\mu = i\partial_\mu - gT \cdot W_\mu + g'YB_\mu \quad (1.6)$$

and the field intensity tensors

$$W_{\mu\nu} = \partial_\mu W_\nu - \partial_\nu W_\mu - gW_\mu \times W_\nu, \quad (1.7)$$

$$B_{\mu\nu} = \partial_\mu B_\nu - \partial_\nu B_\mu. \quad (1.8)$$

The third component  $W_\mu^3$  of the gauge field  $SU(2)_L$  mixes with the  $U(1)_Y$  gauge field  $B_\mu$ , whereby the physical fields

$$\begin{pmatrix} A_\mu \\ Z_\mu \end{pmatrix} = \begin{pmatrix} \cos\theta_W & \sin\theta_W \\ -\sin\theta_W & \cos\theta_W \end{pmatrix} \cdot \begin{pmatrix} B_\mu \\ W_\mu^3 \end{pmatrix} \quad (1.9)$$

are built, which can be identified with the photon and the  $Z^0$  boson [22], [23]. The angle  $\theta_W$  was introduced by Glashow and Weinberg in 1961 and is called weak mixing angle. The world average of this angle is  $\sin^2\theta_W = 0.2228 \pm 0.0004$  [6]. To express the superposition of states by a rotational matrix is a very elegant mathematical concept, which will reoccur a couple of times later on. The remaining fields  $W_\mu^1$  and  $W_\mu^2$  are the charged gauge bosons

$$W_\mu^\pm = \frac{1}{\sqrt{2}}(W_\mu^1 \mp W_\mu^2). \quad (1.10)$$

The neutral eigenstates  $A_\mu$  and  $Z_\mu$  couple to left-handed as well as right-handed fermions, whereas the charged gauge bosons  $W_\mu^\pm$  couple only to particles having a non-disappearing isospin  $|\vec{T}| \neq 0$ . Therefore a coupling to right-handed fermions is not possible. The coupling strengths  $g$  and  $g'$  obey the equation

$$g \sin\theta_W = g' \cos\theta_W = e, \quad (1.11)$$

with the elementary charge  $e$ . This is directly derived from the claim, that the photon field  $A_\mu$  has to couple to charged leptons with the strength  $e$  of the electromagnetic interaction. The coupling of the  $Z^0$  boson is

$$-i \frac{g}{\cos\theta_W} \gamma^\mu \frac{1}{2} (c_V^f - c_A^f \gamma^5), \quad (1.12)$$

where the vector coupling  $c_V^f$  and the axial coupling  $c_A^f$  are given by the third component of the isospin  $T_3^f$  and through the charge  $q_f$  of a fermion  $f$

$$c_V^f = T_3^f - 2 \sin\theta_W q_f, \quad (1.13)$$

$$c_A^f = T_3^f. \quad (1.14)$$

### Spontaneous Symmetry Breaking

The electroweak and the strong gauge theory are exact for massless particles only. But the gauge bosons  $Z^0$ ,  $W^+$  and  $W^-$  and leptons and quarks do have masses. To solve this difficulty, Peter Higgs introduced the Higgs mechanism [24] in 1964. The Lagrange density from Equation 1.5 remains gauge invariant, if an additional term

$$\mathcal{L}_{Higgs} = (D_\mu \Phi)^\dagger (D^\mu \Phi) - V(\Phi) \quad (1.15)$$

is added, where  $\Phi$  is a complex scalar field with two components

$$\Phi(x) = \begin{pmatrix} \Phi^+ \\ \Phi^0 \end{pmatrix} = \frac{1}{\sqrt{2}} \begin{pmatrix} \Phi_1 + i\Phi_2 \\ \Phi_3 + i\Phi_4 \end{pmatrix} \quad (1.16)$$

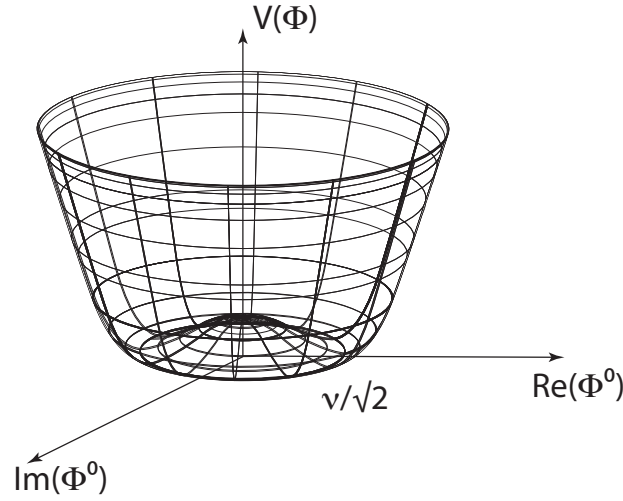


**Figure 1.2:** The Higgs potential. Due to its shape it is also called Mexican hat potential.

and the potential  $V(\Phi)$  is given by

$$V(\Phi) = \mu^2 \Phi^\dagger \Phi + \lambda (\Phi^\dagger \Phi)^2. \quad (1.17)$$

By choosing the parameters  $\mu^2 < 0$  and  $\lambda > 0$ , a potential with a set of degenerate ground states is obtained as shown in Figure 1.2. A possible vacuum expectation value is

$$\langle \Phi \rangle = \frac{1}{\sqrt{2}} \begin{pmatrix} 0 \\ v \end{pmatrix}. \quad (1.18)$$

By expanding this vacuum expectation value around the minimum, the equation

$$\Phi(x) = \frac{1}{\sqrt{2}} \begin{pmatrix} 0 \\ v + H(x) \end{pmatrix} \quad (1.19)$$

is obtained. Using Equation 1.18 and the covariant derivation leads to

$$D_\mu \langle \Phi \rangle = \left[ \frac{ig}{2} \begin{pmatrix} W_\mu^3 & W_\mu^1 - iW_\mu^2 \\ W_\mu^1 + iW_\mu^2 & -W_\mu^3 \end{pmatrix} + \frac{ig'}{2} B_\mu \right] \frac{1}{\sqrt{2}} \begin{pmatrix} 0 \\ v \end{pmatrix}. \quad (1.20)$$

Inserting this Equation into the Lagrange density  $(D_\mu \langle \Phi \rangle)^\dagger (D_\mu \langle \Phi \rangle)$  provides further quadratic terms, which are equivalent to gauge boson masses

$$M_W^2 = \frac{1}{4} v^2 g^2, \quad (1.21)$$

$$M_Z^2 = \frac{1}{4} v^2 (g^2 - g'^2) \quad \text{and} \quad (1.22)$$

$$M_\gamma^2 = 0. \quad (1.23)$$

In combination with Equation 1.11 this leads to a relationship between the  $Z^0$  and  $W^\pm$  masses

$$\frac{M_W}{M_Z} = \cos \theta_W. \quad (1.24)$$

With the exception of mass, all Higgs parameters are given by theory. The Higgs boson has not been observed yet. Via direct searches, the LEP experiments set a lower limit for the Higgs mass of  $m_H \geq 114.4 \text{ GeV}/c^2$  (95% CL) [25]. Searches for the Higgs boson are also performed at the Fermilab Tevatron Collider [26], where sensitivity to SM cross-sections are just being reached. The Large Hadron Collider (LHC) [27], which will begin operation soon, was built to find the Higgs boson no matter what its mass (it is expected to be found within the TeV-scale).

The masses of the fermions originate from the Higgs field  $\Phi$  in the same way as the masses of the weak gauge bosons. The interaction of the Higgs field with the fermions is described through a Yukawa term in the Lagrange density

$$\mathcal{L}_{Yukawa} = \bar{\Psi}'_L \Phi_i C_i \Psi'_R + h.c., \quad (1.25)$$

where  $\Psi'_{R,L} = \frac{1}{2}(1 \pm \gamma_5)\Psi'$  are right-handed and left-handed fermion-fields and  $C_i$  is an arbitrary complex matrix with the weak isospin components  $i = 1, 2$ . Therefore, the fermion mass terms are

$$\mathcal{L}_{mass} = -(\bar{u}', \bar{c}', \bar{t}')_R M_u \begin{pmatrix} u' \\ c' \\ t' \end{pmatrix}_L - (\bar{d}', \bar{s}', \bar{b}')_R M_d \begin{pmatrix} d' \\ s' \\ b' \end{pmatrix}_L - (\bar{e}', \bar{\mu}', \bar{\tau}')_R M_l \begin{pmatrix} e' \\ \mu' \\ \tau' \end{pmatrix}_L + h.c. \quad (1.26)$$

with non-diagonal mass matrices  $M_u$ ,  $M_d$  and  $M_l$ , proportional to the vacuum expectation value  $\langle \Phi \rangle$  of the Higgs field and the Yukawa couplings. Neutrinos don't have a corresponding mass term in  $\mathcal{L}_{mass}$  as no right-handed fields exist in the standard model. Thus,  $M_l$  is a diagonal matrix and thus the mass eigenstates  $l_{L,R}$  correspond to the weak eigenstates  $l'_{L,R}$  where  $l$  is either an electron, a muon or a tau.

### 1.2.3. Mesons and Baryons

As mentioned in Section 1.2.2, quarks can not exist as free particles [19]. The elementary particles, which let quarks interact, are called gluons. Gluons are vector bosons with a spin of 1. While massive spin-1 particles have three polarization states, massless gauge bosons like the gluon have only two polarization states because gauge invariance requires the polarization to be transverse. In quantum field theory, unbroken gauge invariance requires that gauge bosons have zero mass (experiment limits the gluon's mass to less than a few  $\text{MeV}/c^2$  [28]). The gluon has negative intrinsic parity and zero isospin. It is its own antiparticle. A confined state of quarks has to be neutral in color, leading to either bound states of a quark and an anti-quark, the so-called mesons, or states with three quarks with each having a different color – the baryons.

The proton (made up of two up and one down quark) and the neutron (made up of one up and two down quarks), representatives of the baryons were known for a long time, although they were expected to be elementary particles. As there are not only bound states of the first quark generation, five of the six quarks lead to a variety of mesons and baryons<sup>9</sup>. The first observed meson was the pion consisting of the two lightest quarks ( $|\pi^+\rangle = |u, \bar{d}\rangle$ ,  $|\pi^-\rangle = |d, \bar{u}\rangle$ ). Table 1.2 shows an overview of some mesons, playing a role in the analysis discussed later.

<sup>9</sup>No bound state of the top quark is known so far, as it has a very short lifetime.

Meson	Quark content	Mass (MeV/c <sup>2</sup> )	Lifetime (s)
$\pi^0$	$(u\bar{u} - d\bar{d})/\sqrt{2}$	$134.9766 \pm 0.0006$	$(8.4 \pm 0.6) \times 10^{-17}$
$\pi^+, \pi^-$	$(u, \bar{d}), (\bar{u}, d)$	$139.57018 \pm 0.00035$	$(2.6033 \pm 0.0005) \times 10^{-8}$
$K^+, K^-$	$(u, \bar{s}), (\bar{u}, s)$	$493.677 \pm 0.016$	$(1.2385 \pm 0.0024) \times 10^{-8}$
$K_S$	$(d, \bar{s})$	$497.648 \pm 0.022$	$(0.8953 \pm 0.0005) \times 10^{-10}$
$K_L$	$(d, \bar{s})$	$497.648 \pm 0.022$	$(5.114 \pm 0.021) \times 10^{-8}$
$D^+, D^-$	$(c, \bar{d}), (\bar{c}, d)$	$1869.3 \pm 0.4$	$(1040 \pm 7) \times 10^{-15}$
$D^0$	$(c, \bar{u})$	$1864.5 \pm 0.4$	$(410.1 \pm 1.5) \times 10^{-15}$
$D_s^+, D_s^-$	$(c, \bar{s}), (\bar{c}, s)$	$1968.2 \pm 0.5$	$(500 \pm 7) \times 10^{-15}$
$B^+, B^-$	$(u, \bar{b}), (\bar{u}, b)$	$5279.0 \pm 0.5$	$(1.638 \pm 0.011) \times 10^{-12}$
$B_d$	$(d, \bar{b})$	$5279.5 \pm 0.5$	$(1.530 \pm 0.009) \times 10^{-12}$
$B_s$	$(s, \bar{b})$	$5367.5 \pm 1.8$	$(1.466 \pm 0.059) \times 10^{-12}$
$B_c^+, B_c^-$	$(c, \bar{b}), (\bar{c}, b)$	$6286 \pm 5$	$(0.46^{+0.18}_{-0.16}) \times 10^{-12}$

**Table 1.2:** Overview of mesons with their quark content, mass and lifetime. All values are world-averages [6].

### 1.2.4. Weak Interactions of Quarks

The interactions between different quarks arise from the Yukawa coupling of the quarks to the Higgs field. The following subsections are devoted to a theoretical description of this topic, which was introduced by Nicola Cabibbo and its historical development.

#### Light Quark Coupling

In 1963 Cabibbo introduced a model [29], which describes the coupling between quarks of different generations. However, experiments showed a discrepancy. This dilemma was solved in 1970 by Glashow, Iliopoulos and Maiani. They introduced the  $c$ -quark<sup>10</sup>, which built a doublet with the  $s$ -quark and solved the problem. This solution is called GIM-mechanism [30] and was confirmed in 1974, when the  $J/\Psi$  resonance [31], [32] was found. The  $J/\Psi$  is a bound  $c\bar{c}$  state. Even before this particle was found, Kobayashi and Maskawa introduced a third generation of quarks made up of the beauty ( $b$ ) and top ( $t$ ) quark, extending Cabibbo's two-family description of quark weak and mass eigenstates. The  $b$ -quark was discovered in 1977 [33] (a more sophisticated historical overview can be found in [34]), while the top-quark was found in 1995 at Fermilab [17], [18].

#### The CKM Matrix

By using Equation 1.26, the physical mass eigenstates  $\Psi$  can be used instead of the gauge eigenstates  $\Psi'$ . Therefore, the mass matrix  $M_i$  is diagonalized by a bi-unitary transformation

$$\bar{\Psi}'_{iL} M_i \Psi'_{iR} = \bar{\Psi}'_{iL} U_{iL}^* M_i^{diag} U_{iR} \Psi'_{iR} = \bar{\Psi}_{iL} M_i^{diag} \Psi_{iR}, (i = u, d), \quad (1.27)$$

<sup>10</sup>charm-quark: as it solved the problem in a charming way.



with the unitary matrices  $U_{iL}$ ,  $U_{iR}$  and the mass eigenstates  $\Psi_{iL,R} = U_{iR,L} \Psi'_{iR,L}$ . By introducing the CKM-matrix

$$V_{CKM} = U_{uL}^* U_{dL} \quad (1.28)$$

$$= \begin{pmatrix} V_{ud} & V_{us} & V_{ub} \\ V_{cd} & V_{cs} & V_{cb} \\ V_{td} & V_{ts} & V_{tb} \end{pmatrix} \quad (1.29)$$

$$= \begin{pmatrix} c_{12}c_{13} & s_{12}c_{13} & s_{13}e^{i\delta_{13}} \\ -s_{12}c_{23} - c_{12}s_{23}s_{13}e^{i\delta_{13}} & c_{12}c_{23} - s_{12}s_{23}s_{13}e^{i\delta_{13}} & s_{23}c_{13} \\ s_{12}s_{23} - c_{12}c_{23}s_{13}e^{i\delta_{13}} & -c_{12}s_{23} - s_{12}c_{23}s_{13}e^{i\delta_{13}} & c_{23}c_{13}\hat{a} \end{pmatrix} \quad (1.30)$$

(with  $s_{ij} \equiv \sin\theta_{ij}$  and  $c_{ij} \equiv \cos\theta_{ij}$ ) the weak charged current can be written as a function of the physical quark fields. If the CKM matrix has complex entries, then the CP symmetry is broken. The strength of this violation is proportional to the Jarlskog invariant

$$J = c_{12}c_{23}c_{13}^2 s_{12}s_{23}s_{13} \sin\delta_{13}, \quad (1.31)$$

where the parameters must fulfill the requirement

$$\delta_{13} \neq 0, \pi \quad \text{and} \quad \theta_{ij} \neq 0, \frac{\pi}{2}. \quad (1.32)$$

Otherwise  $J$  vanishes. A commonly used parametrization of the CKM matrix is the Wolfenstein parametrization. It is based on the observation, that the diagonal elements are close to 1 with progressively smaller elements away from the diagonal. By defining the variable set

$$\lambda \equiv s_{12}, \quad A \equiv s_{23}/\lambda^2 \quad \text{and} \quad \rho + i\eta \equiv s_{13}e^{i\delta_{13}}/A\lambda^3, \quad (1.33)$$

which are experimentally found to be  $\lambda \approx 0.22$ ,  $A \approx 0.8$  and  $\sqrt{\rho^2 + \eta^2} \approx 0.4$ , the CKM-matrix becomes

$$V_{CKM} = \begin{pmatrix} 1 - \frac{\lambda^2}{2} & \lambda & \lambda^3 A(\rho - i\eta) \\ -\lambda & 1 - \frac{\lambda^2}{2} & \lambda^2 A \\ \lambda^3 A(1 - \rho - i\eta) & -\lambda^2 A & 1 \end{pmatrix} \quad (1.34)$$

and the Jarlskog invariant can be expressed as  $J = A^2 \lambda^6 \eta \approx (7 \times 10^{-5})\eta$ . A convenient way to illustrate the CKM matrix are the unitarity triangles.

### The Unitarity Triangles

Due to the unitarity of the CKM matrix  $V_{CKM}$  ( $V_{CKM}^\dagger V_{CKM} = 1$ ) the following six Equations

$$V_{ud}V_{us}^* + V_{cd}V_{cs}^* + V_{td}V_{ts}^* = 0, \quad (1.35)$$

$$V_{us}V_{ub}^* + V_{cs}V_{cb}^* + V_{ts}V_{tb}^* = 0, \quad (1.36)$$

$$V_{ud}V_{ub}^* + V_{cd}V_{cb}^* + V_{td}V_{tb}^* = 0, \quad (1.37)$$

$$V_{ud}V_{cd}^* + V_{us}V_{cs}^* + V_{ub}V_{cb}^* = 0, \quad (1.38)$$

$$V_{cd}V_{td}^* + V_{cs}V_{ts}^* + V_{cb}V_{tb}^* = 0, \quad (1.39)$$

$$V_{ud}V_{td}^* + V_{us}V_{ts}^* + V_{ub}V_{tb}^* = 0 \quad (1.40)$$

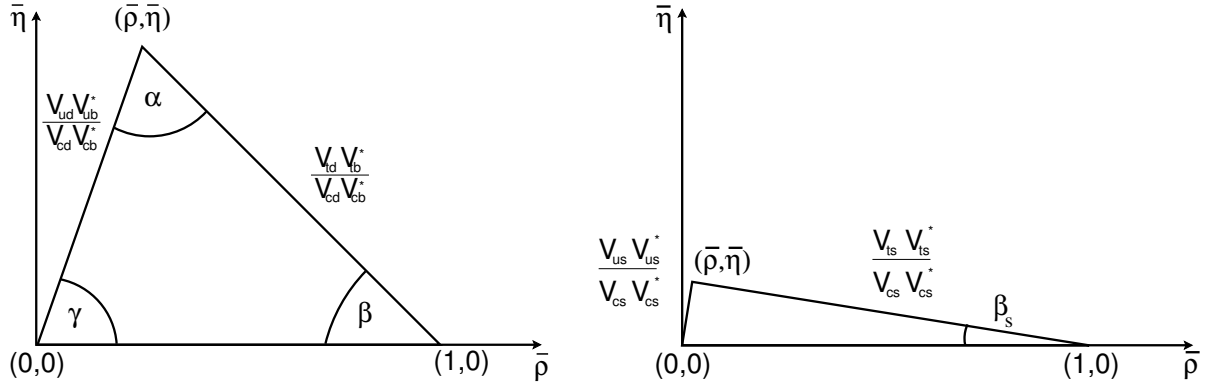


**Figure 1.3:** Left: Unitarity triangle from Equation 1.37, Right: Squashed unitarity triangle (Equation 1.36). The approximation  $\bar{\rho} = \rho(1 - \lambda^2/2 + \dots)$  is commonly used for illustration purposes (the same applies for  $\bar{\eta}$ ) [6].

are valid. By using the Wolfenstein parametrization they can be visualized as triangles in the complex plane  $(\rho, \eta)$  as illustrated in Figure 1.3 for Equation 1.37. The three angles of this triangle are

$$\alpha = \arg \left[ -\frac{V_{td} V_{tb}^*}{V_{ud} V_{ub}^*} \right] = \tan^{-1} \left( \frac{\bar{\eta}}{\bar{\eta}^2 + \bar{\rho}(\bar{\rho} - 1)} \right), \quad (1.41)$$

$$\beta = \arg \left[ -\frac{V_{cd} V_{cb}^*}{V_{td} V_{tb}^*} \right] = \tan^{-1} \left( \frac{\bar{\eta}}{1 - \bar{\rho}} \right), \quad (1.42)$$

$$\gamma = \arg \left[ -\frac{V_{cd} V_{cb}^*}{V_{ud} V_{ub}^*} \right] = \tan^{-1} \left( \frac{\bar{\eta}}{\bar{\rho}} \right), \quad (1.43)$$

using the approximation  $\bar{\rho} = \rho(1 - \lambda^2/2 + \dots)$  and  $\bar{\eta} = \eta(1 - \lambda^2/2 + \dots)$ . A detailed explanation of this approximation can be found in Chapter 11.1 of [6]. This unitarity triangle is unique, as its three sides are all of the same order  $\mathcal{O}(\lambda^3)$ . All the unitarity triangles, however, have the same area, which is proportional to the magnitude of  $CP$ -violation. Conventionally, the real side of the triangle from Equation 1.37, is normalized to one using

$$\bar{\rho} + i\bar{\eta} \equiv -\frac{V_{ud} V_{ub}^*}{V_{cd} V_{cb}^*} \quad (1.44)$$

and results in side lengths

$$R_b \equiv \sqrt{\bar{\rho}^2 + \bar{\eta}^2} = \frac{1 - \lambda^2/2}{\lambda} \left| \frac{V_{ub}}{V_{cb}} \right|, \quad (1.45)$$

$$R_t \equiv \sqrt{(1 - \bar{\rho}^2) + \bar{\eta}^2} = \frac{1}{\lambda} \left| \frac{V_{td}}{V_{cb}} \right| \quad (1.46)$$

At the Tevatron  $B_s$  mesons are produced and Equation 1.36 becomes relevant. It is often referred as the *squashed triangle* (Figure 1.3), as one side is much shorter than the other two. The angle

$$\beta_s = \arg \left[ -\frac{V_{ts} V_{tb}^*}{V_{cs} V_{cb}^*} \right] \quad (1.47)$$

is of the order of one degree. As it is dominated by penguin topologies<sup>11</sup> [35], it is much more sensitive to physics beyond the standard model (new physics) [36] in  $B_s$ - $\bar{B}_s$  mixing, which will be

<sup>11</sup>Penguin topologies are a certain class of Feynman diagrams. John Ellis was the first to refer this name, due to their shape.

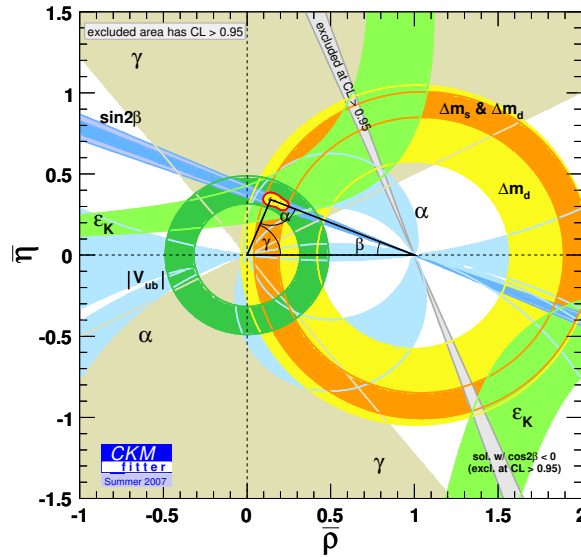


**Figure 1.4:** Experimental constraints on the unitarity triangle [37] in the  $\bar{\rho}, \bar{\eta}$  plane. The experimental uncertainties are shown as colored bands. An outlook about the expectation of the experimental uncertainties is given in Chapter 10.

described in the next section. Figure 1.4 shows the experimental constraints on the unitarity triangle. As can be seen,  $R_t$  is the least well-measured of the sides. How to measure all CKM matrix elements and which physical processes are used is described in detail in Chapter 11.2 of [6].

### 1.3. Mixing of Neutral Mesons

The transition of a neutral meson into its anti-particle and vice versa is called mixing or oscillation. This behavior was first proposed by Gell-Mann and Pais [38] in 1955 for the  $K-\bar{K}^0$  system. Shortly after the two weak eigenstates  $K_S$  and  $K_L$  were found by Ledermann and his coworkers [39], [40].

First evidence of the mixing of neutral  $B$  mesons was found by the UA1 collaboration [41] at CERN and in 1987 mixing of  $B_d$  mesons was observed by the ARGUS [8] collaboration at DESY, where the production  $e^+e^- \rightarrow Y(4S) \rightarrow B_d \bar{B}_d$  ended up in the final state of two  $B_d$  mesons (Figure 1.5). In principle this process should be possible for all neutral meson systems. In fact, it was observed for neutral  $D$  mesons at BaBar in March 2007 [42]. Figure 1.6 shows the corresponding Feynman box diagrams for the mixing of  $B_{d,s}^0$  systems. These diagrams also reveal the fact, that the CKM-matrix element  $|V_{td}|$  and thus the least known length  $R_t$  of the unitarity triangle is accessible through mixing. In the following, the main principle of mixing will be described for both  $B_s$  and  $B_d$  mesons, therefore  $B^0$  will be used for the following theoretical description.

A  $B^0$  or  $\bar{B}^0$  meson, initially produced in a flavor (gauge) eigenstate, evolves into a superimposition of  $B^0$  and  $\bar{B}^0$ . The evolution in time is given by a Schrödinger-like Equation

$$i \frac{d}{dt} \begin{pmatrix} |B^0\rangle \\ |\bar{B}^0\rangle \end{pmatrix} = \left( M - i \frac{\Gamma}{2} \right) \begin{pmatrix} |B^0\rangle \\ |\bar{B}^0\rangle \end{pmatrix}, \quad (1.48)$$

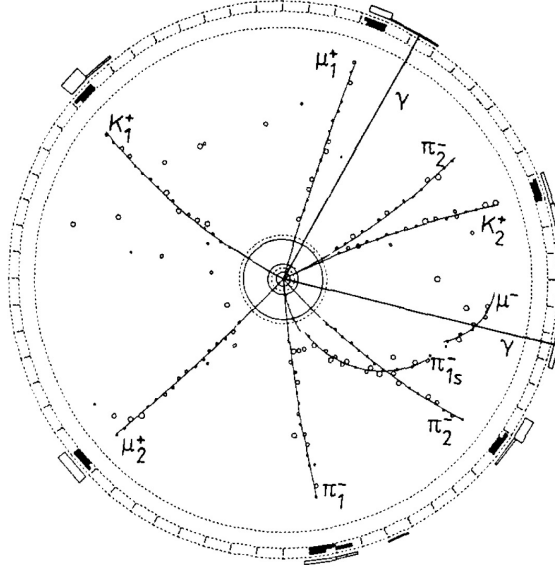


**Figure 1.5:** ARGUS event display of the first observed  $B_d \bar{B}_d$  mixing event [8]. The event is shown as a projection to a plane perpendicular to the cylindrical shaped detector. As  $b\bar{b}$  quarks are always created in pairs, it was expected to observe a  $B_d$  in combination with a  $\bar{B}_d$  meson. But the event display shows the decays  $B_d \rightarrow D^{*-}(\pi^- \bar{D}^0)\mu^+\nu_\mu$ ,  $\bar{D}^0 \rightarrow K^+\pi^-$  and  $B_d \rightarrow D^{*-}(\pi^0 D^-)$ ,  $D^- \rightarrow K^+\pi^-\pi^-$ . Hence, the  $\bar{B}_d$  meson must have mixed.

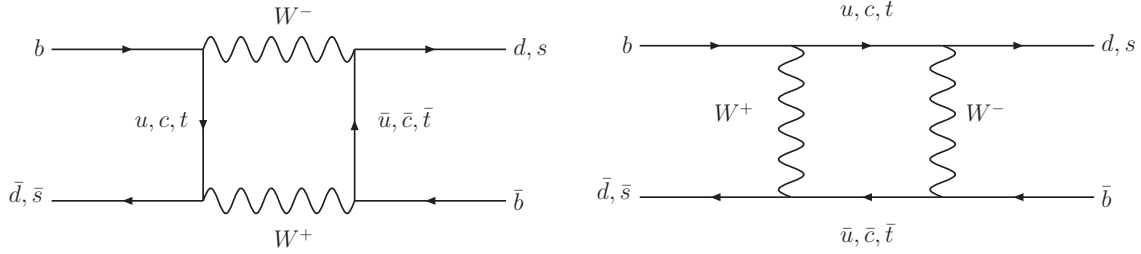


**Figure 1.6:** Feynman graphs for  $B_{d,s}^0 \bar{B}_{d,s}^0$  mixing. Quarks are shown as straight lines, while bosons are illustrated by wave-lines.

where  $M$  and  $\Gamma$  are time-independent Hermetian  $2 \times 2$  matrices. Because of  $CPT$  invariance the following applies:

$$M = M_{11} = M_{22} \quad \text{and} \quad \Gamma = \Gamma_{11} = \Gamma_{22}, \quad (1.49)$$

which implies that the  $B^0$  meson and its anti-particle have the same mass and decay width. But as the non-diagonal elements are non-zero the weak (flavor) eigenstates and the mass eigenstates are different. The mass eigenstates are superpositions of the weak eigenstates

$$|B_L\rangle = p|B^0\rangle + q|\bar{B}^0\rangle, \quad (1.50)$$

$$|B_H\rangle = p|B^0\rangle - q|\bar{B}^0\rangle, \quad (1.51)$$

where  $B_L$  is the light eigenstate.  $B_H$  is the heavy eigenstate and  $|p|^2 + |q|^2 = 1$ . The mass eigenstates evolve independently in time

$$|B_L(t)\rangle = e^{-(iM_L + \Gamma_L/2)t} |B_L\rangle, \quad (1.52)$$

$$|B_H(t)\rangle = e^{-(iM_H + \Gamma_H/2)t} |B_H\rangle. \quad (1.53)$$

Using the relation 1.50 this can be converted to

$$|B^0(t)\rangle = \frac{1}{2p} \left[ e^{-(iM_L - \Gamma_L/2)t} |B_L\rangle + e^{-(iM_H - \Gamma_H/2)t} |B_H\rangle \right], \quad (1.54)$$

$$|\bar{B}^0(t)\rangle = \frac{1}{2p} \left[ e^{-(iM_L - \Gamma_L/2)t} |B_L\rangle - e^{-(iM_H - \Gamma_H/2)t} |B_H\rangle \right]. \quad (1.55)$$

By applying the Equations

$$g_{\pm}(t) \equiv \frac{1}{2} \left( e^{-iM_L t} e^{-\Gamma_L t/2} \pm e^{-iM_H t} e^{-\Gamma_H t/2} \right) \quad (1.56)$$

with the average mass and width

$$m = \frac{M_H + M_L}{2} = M_{11} \quad \text{and} \quad \Gamma = \frac{\Gamma_L + \Gamma_H}{2} = \Gamma_{11} \quad (1.57)$$

and the mass and width difference

$$\Delta m = M_H - M_L \quad \text{and} \quad \Delta \Gamma = \Gamma_L - \Gamma_H \quad (1.58)$$

the mass eigenstates can be eliminated in favor of the flavor eigenstates

$$|B^0(t)\rangle = g_+(t)|B^0\rangle + \frac{q}{p} g_-(t)|\bar{B}^0\rangle, \quad (1.59)$$

$$|\bar{B}^0(t)\rangle = \frac{p}{q} g_-(t)|B^0\rangle + g_+(t)|\bar{B}^0\rangle. \quad (1.60)$$

Solving the eigenvalue problem leads to

$$\left| \frac{q}{p} \right|^2 = \left| \frac{2M_{12}^* - i\Gamma_{12}^*}{2M_{12} - i\Gamma_{12}} \right|. \quad (1.61)$$

If  $CP$  were conserved, the relative phases between  $M_{12}$  and  $\Gamma_{12}$  would vanish and  $|q/p| = 1$ . In the case of  $CP$  violation it would become  $|q/p| \neq 1$ . The fraction  $|q/p|$  is measurable directly through the asymmetry.

The oscillation frequency can be found from measurements of the time evolution of oscillated and non-oscillated events

$$A(t) = \frac{N_{osc.}(t) - N_{non-osc.}(t)}{N_{osc.}(t) + N_{non-osc.}(t)} = \cos(\Delta m_s t), \quad (1.62)$$

where  $N_{osc.}(t)$  is the number of oscillated events  $B^0 \rightarrow \bar{B}^0$ ,  $\bar{B}^0 \rightarrow B^0$  and  $N_{non-osc.}(t)$  is the number of non-oscillated events  $B^0 \rightarrow B^0$ ,  $\bar{B}^0 \rightarrow \bar{B}^0$ . Figure 1.7 shows the challenge in measuring  $\Delta m_s$ , which is about 40 times larger than  $\Delta m_d$ . Measuring this much more rapid oscillation puts stringent requirements on an experiment's proper time resolution.

The least known length of the unitarity triangle is  $R_t$ . As it is proportional to the CKM matrix element  $|V_{td}|$  ((Equation 1.46), the length can be measured through  $B_d$  mixing [11]

$$\Delta m_d = const \times f_{B_d}^2 B_{B_d} |V_{tb}^* V_{td}|^2, \quad (1.63)$$

where  $const$  is a known constant factor,  $f_{B_d}^2$  is the  $B_d$  decay constant and  $B_{B_d}$  is the bag parameter<sup>12</sup>

$$\langle \bar{B}_q | \left[ \bar{\Psi}_b^i (V - A) \Psi_q^i \right] \left[ \bar{\Psi}_b^i (V - A) \Psi_q^i \right] | B_q \rangle \equiv \frac{8}{3} m_{B_q} f_{B_q}^2 \quad \text{with} \quad q = d, s. \quad (1.64)$$

<sup>12</sup>The bag model provides a useful phenomenological description of quarks being confined inside hadrons. The bag parameter is equivalent to a volume term in this model.

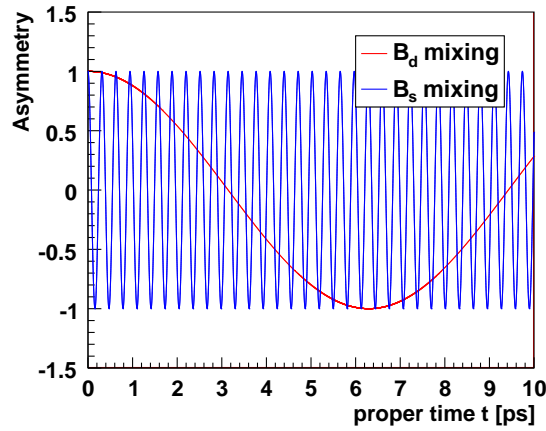


**Figure 1.7:** Comparing the mixing frequency of  $B_d$  and  $B_s$  mesons. Shown is the asymmetry as a function of the proper time.  $\Delta m_s$  is about 40 times larger than  $\Delta m_d$ .

In this equation  $(\bar{b}q)_{V-A}$  is the  $V-A$  current involving  $b$  and  $q = d, s$  quarks. The frequency  $\Delta m_d$  was precisely measured at the  $B$ -factories BaBar and Belle to be  $\Delta m_d = (0.507 \pm 0.005) \text{ ps}^{-1}$  [6]. Thus, the CKM matrix element  $|V_{td}|$  should be known precisely as well. But there are large uncertainties in the order of 20% from lattice calculations [11] of  $f_{B_d}^2 B_{B_d}$  and thus, the extraction of  $|V_{td}|$  has also large uncertainties. By measuring the mass differences  $\Delta m_d$  and  $\Delta m_s$  and calculating their ratio most of the uncertainties cancel out

$$\frac{\Delta m_s}{\Delta m_d} = \frac{m_{B_s}}{m_{B_d}} \xi^2 \frac{|V_{ts}|^2}{|V_{td}|^2}. \quad (1.65)$$

The constant  $\xi = 1.210^{+0.047}_{-0.035}$  has approximately 4% uncertainties left from lattice calculations [11].

## 1.4. Production of B Mesons at Hadron Colliders

Two criteria have to be fulfilled to observe and measure the mixing frequency: the collision energy must be high enough to create  $B_s$  mesons and the Lorentz-boost of the  $B_s$  mesons has to be large enough to allow reconstruction of  $B_s$  flight lengths. As the collisions of the  $B$ -factories BaBar and Belle happen at the  $\Upsilon(4S)$  resonance ( $\sqrt{s} = 10.5 \text{ GeV}$ ) the first of these criteria is not met – although the Belle collaboration tuned the accelerator complex to do some measurements at the  $\Upsilon(5S)$  resonance ( $\sqrt{s} = 10.8 \text{ GeV}$ ), which has a mass high enough to decay into  $B_s$  mesons. Nevertheless, only a small sample of  $B_s$  mesons was produced. Therefore, the hadron collider Tevatron ( $\sqrt{s} = 1.96 \text{ TeV}$ ) is currently the only place to study  $B_s$  oscillations worldwide.

Hadron colliders produce a rich spectrum of  $B$  physics as all  $B$  hadrons are produced; not only charged and neutral  $B$  mesons as at the  $B$  factories, but also  $B_s$  mesons and  $b$ -baryons. The second advantage is the  $b$  quark production cross section, which is about 1 nb at the  $\Upsilon(4S)$  resonance while it is about  $50 \mu\text{b}$  [6] for  $p\bar{p}$  collisions at the center of mass energy of the Fermilab Tevatron Collider. This is an enormous cross section which is about 50,000 times larger at the Tevatron than at the  $B$  factories (Table 1.3). Contrary to  $e^+e^-$  colliders like LEP, where the initial state is completely known because of the pointlike electrons, at hadron colliders the substructure of the colliding particles has

Experiment	Process	$\sqrt{s}$	$\sigma$
LEP, SLC	$e^+e^- \rightarrow Z \rightarrow b\bar{b}$	$Z$	7 nb
PEP-II, KEK-B	$e^+e^- \rightarrow \Upsilon(4s) \rightarrow B\bar{B}$	$\Upsilon(4s)$	1 nb
Tevatron	$p\bar{p} \rightarrow b\bar{b}$	1.96 TeV	150 $\mu$ b
LHC	$p\bar{p} \rightarrow b\bar{b}$	14 TeV	400-500 $\mu$ b (expected)

**Table 1.3:** Overview of the production cross section of  $b\bar{b}$  pairs of past, current and future experiments. As it can be seen only the Tevatron and the upcoming LHC provide a center-of-mass energy, which is high enough to produce  $B_s$  mesons.

to be taken into account. In the case of the Fermilab Tevatron Collider protons and anti-protons are collided. To understand the kinematics of hadron collider collisions is a challenging task, as the total momentum is not split equally between all partons. Hence, a parton distribution function (PDF) [43]  $f_i^a(x)$  has to be used to express the probability that a parton  $i$  carries the  $x$ -th part of the total momentum. Most of the momentum is carried by the gluons, while valence and sea quarks carry only a small fraction of it.

At leading order, heavy quarks are produced only through quark-anti-quark annihilation (Figure 1.8 a) and gluon-gluon fusion (Figure 1.8 b-d). While  $t$  quarks are primarily created through quark-anti-quark annihilation, the gluon-gluon fusion is the dominating process to produce  $b$  quarks. The  $b\bar{b}$  quark pairs are produced back-to-back in leading order and carry the same transverse momentum in the observer's frame. A non-negligible fraction of  $b$  quark production arises from next-to-leading-order processes, where virtual gluons or quarks are emitted. This includes matrix elements of the real emission process (Figure 1.9 a), as well as interferences of virtual matrix elements in leading order (Figure 1.9 b), gluon splitting (Figure 1.9 c) or flavor excitation (Figure 1.9 d).

The process of building  $b$  hadrons out of the  $b$  and  $\bar{b}$  quarks is called hadronization (Figure 1.10 I-III). The  $b$  quarks are produced through inelastic scattering of the partons in the proton and anti-proton (Figure 1.10 I). In the resulting process of hadronization or fragmentation the  $b$  hadrons are created (Figure 1.10 II). As this process can not be described by perturbative models, a set of free parameters has to be used, where the parameters are fitted to match the experimental data. One of these models is the Lund string model [44] (Figure 1.10). If two quarks depart one another they expand a string between them. Eventually the string breaks and another quark anti-quark pair with different color materializes. This process repeats and color neutral states are produced either as mesons or baryons. As there is hardly any transfer of momentum the hadrons carry only a small transverse momentum compared to the primary parton. Hence the direction of the particle jets and the total momentum reflects that of the fragmented parton. The fragmentation function  $f(z)$  describes the distribution of the longitudinal momentum  $p_L$  of the produced hadron relative to the original parton. The fragmentation of heavy quarks is well described by the Peterson fragmentation function [45]

$$f_{\text{Peterson}}(z) = N \left[ z \left( 1 - \frac{1}{z} - \frac{\epsilon}{1-z} \right)^2 \right], \quad (1.66)$$

where the parameter  $z$  is defined as normalized momentum fraction

$$z = \frac{(E + p_L)_{\text{hadron}}}{(E + p_L)_{\text{parton}}}, \quad (1.67)$$

and  $N$  is a normalization constant. The Peterson fragmentation constant  $\epsilon_q$  ( $q = b, c$ ) was determined experimentally as  $\epsilon_b \approx 0.006$  [46] and  $\epsilon_c \approx 0.06$  [47]. Average  $b$  hadrons carry about 70% of the original  $b$  quark momentum, while this fraction is about 50% for  $c$  hadrons.

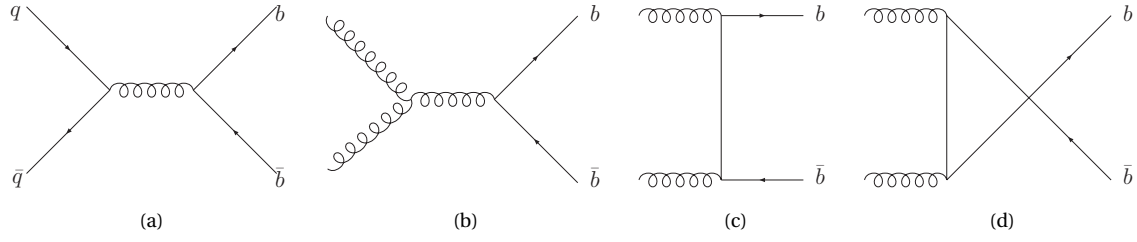


**Figure 1.8:**  $b\bar{b}$  quark production in leading order: (a) quark anti-quark annihilation, (b-d) gluon-gluon fusion. Quarks are shown as straight lines, while gluons are illustrated by curly-lines.

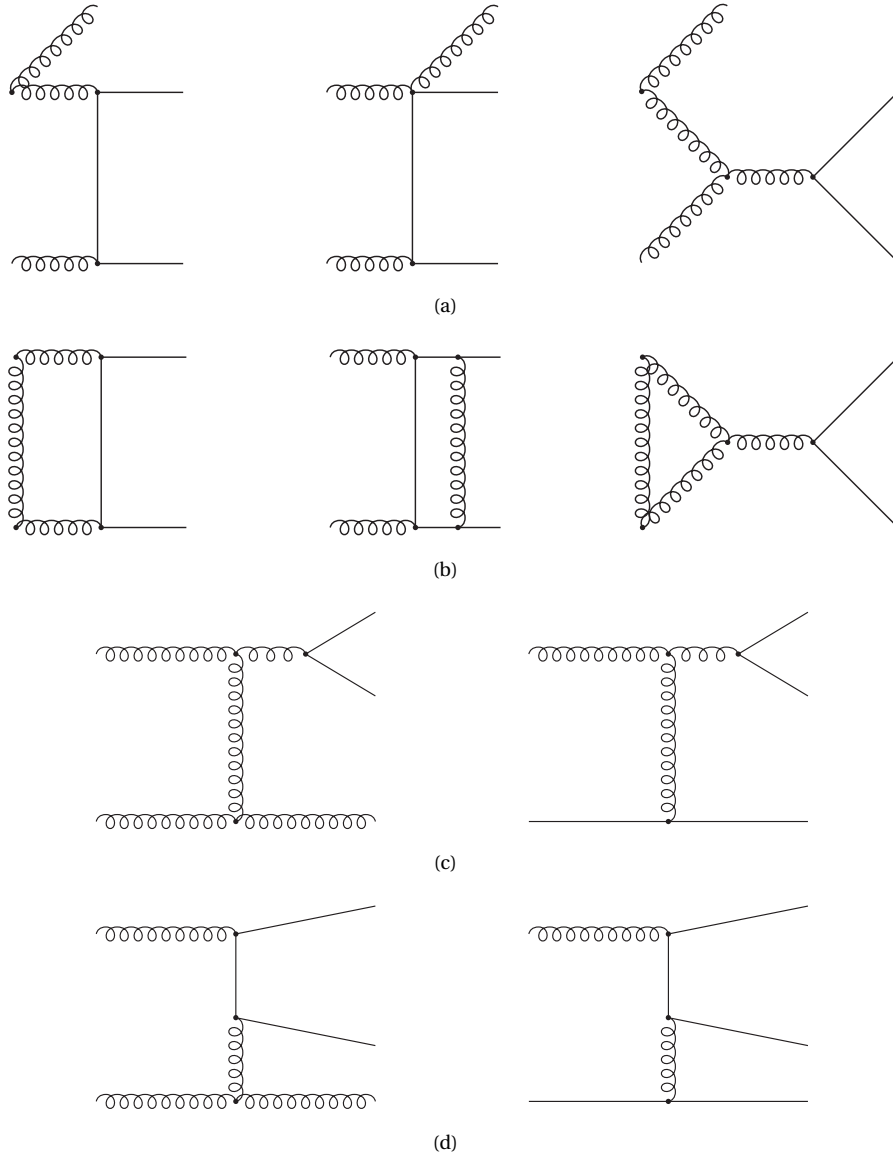


**Figure 1.9:**  $b\bar{b}$  quark production at next-to-leading order level. (a) emission of gluons, (b) virtual gluon exchange, (c) gluon splitting, (d) flavor excitation. Quarks are shown as straight lines, while gluons are illustrated by curly-lines.



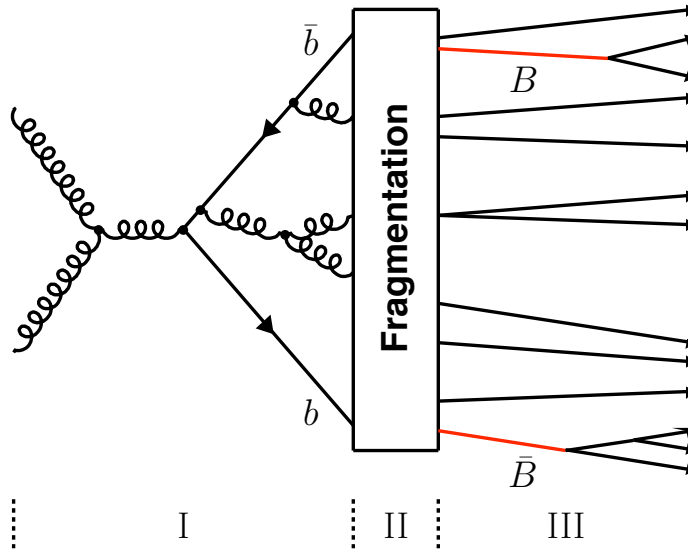


**Figure 1.10:** Schematic view of the production of  $b$  hadrons through gluon-gluon fusion. The  $b$  quarks are produced through inelastic scattering of the partons in the proton and anti-proton (I). In the resulting process of hadronization or fragmentation the  $b$  hadrons are created (II). Finally the decay of short-living hadrons begins (III).

At this stage the decay of short-lived hadrons begins (Figure 1.10 III). Depending on which interaction is involved there are two kinds of decays. For the strong and electromagnetic interaction excited hadron states decay into states with lower energy. The excited states have a short lifetime ( $\mathcal{O}(10^{-22}\text{ s})$ ) and thus have a non-detectable decay length. The lowest mass carrying a specific flavor mesons and baryons only decay through the weak interaction and therefore have a longer lifetime ( $\mathcal{O}(10^{-12}\text{ s})$ ) for mesons or baryons containing heavy quarks. Other hadrons like kaons and pions live even longer and are considered as stable particles as they usually do not decay within the detector.

If the original  $\bar{b}$ -quark generates  $u\bar{u}$ ,  $d\bar{d}$ ,  $s\bar{s}$  or  $c\bar{c}$  pairs during the fragmentation process  $B^+$ ,  $B_d$ ,  $B_s$ ,  $B_c^+$ -mesons or  $b$  baryons are created. The lighter the quarks the more probable is their creation. Hence the production of  $B_s$  mesons is suppressed due to their mass ( $\mathcal{B}(\bar{b} \rightarrow B^+) = \mathcal{B}(\bar{b} \rightarrow B_d) = (39.8 \pm 1.2)\%$ ,  $\mathcal{B}(\bar{b} \rightarrow B_s) = (10.4 \pm 1.4)\%$  [48]).

## 1.5. $B_s$ Mixing in the Standard Model

Symmetries and conservation laws are important in physics. The standard model is a theoretical framework, providing an explanation of elementary particles and their force carriers. It was successful over many years and no inconsistencies are known so far. The hunt for the last missing particle – the Higgs boson – is still ongoing. However, it does not include all forces like gravity and does not provide an explanation for phenomena, like matter-anti-matter asymmetry<sup>13</sup>.

An explanation for matter-anti-matter asymmetry involves  $CP$  violation. The CKM matrix connects the weak eigenstates with the flavor eigenstates and can be visualized through unitarity triangles.

<sup>13</sup>At least not in the order of magnitude the effect occurs.

The area of the triangles are proportional to  $CP$  violation. By over-constraining the unitarity triangle parameters it is possible to check the consistency of the standard model or find evidence of new physics. The least known matrix element is  $|V_{td}|$ , which is accessible through the oscillation of  $B$  mesons. While this oscillation frequency is well-known for  $B_d$  mesons, it is not possible to calculate  $|V_{td}|$  precisely, due to large uncertainties. A solution is to measure the oscillation frequency of  $B_s$  mesons. It is a very challenging task, as  $\Delta m_s$  is about 40 times higher than  $\Delta m_d$ . The Fermilab Tevatron Collider is currently the only place world wide to study  $B_s$  oscillations.

## Principle of the Measurement

A precise measurement of the oscillation frequency of  $B_s$  mesons is essential to determine the matrix element  $|V_{td}|$  of the CKM matrix. Oscillation, in this context, is the transition of a  $B_s$  meson into its anti-particle – the  $\bar{B}_s$  meson – and vice versa.  $B_s$  mesons are produced with a branching ratio of  $\mathcal{B}(\bar{b} \rightarrow B_s) = (10.3 \pm 1.4)\%$  [48]. They have a mass of  $m_{B_s} = (5367.5 \pm 1.8) \text{ MeV}/c^2$  [6] and a mean lifetime of  $\tau = (1.466 \pm 0.059) \text{ s}$  [6]. Hence, the decay length is  $c\tau = 439 \pm 18 \mu\text{m}$  [6]. A decay into  $D_s^- + X$  can be observed with a branching ratio of  $(94 \pm 30)\%$  [6].

The principle of the measurement of  $\Delta m_s$  is described in the following sections. At first a signal sample has to be selected from the data (Section 2.1) by a cut based analysis. In order to determine, whether the  $B_s$  has oscillated or not, the identity of the  $B_s$  meson ( $B_s$  or  $\bar{B}_s$ ) at its production and decay (the “initial” and “final” states) have to be known. The final state can be identified through the observed decay channel. To determine the initial state of the  $B_s$  meson, flavor tagging is used (Section 2.2). In combination with the measurement of the visible proper decay length (Section 2.3) the oscillation frequency is determined through an unbinned Log-likelihood fit (Section 2.4). Combining this measurement with other experimental and theoretical input,  $|V_{td}|/|V_{ts}|$  can be determined (Section 2.5).

### 2.1. Signal Selection

Considering the production cross section  $\sigma(p\bar{p} \rightarrow bX : |y| < 0.1) = (29.4 \pm 0.6 \text{ (stat)} \pm 6.2 \text{ (sys)}) \mu\text{b}$  [49], about  $10^{11}$   $b$  quark events were produced in the dataset of  $2.8 \text{ fb}^{-1}$ . The measurement of the cross section includes a cut on the rapidity, which is defined as

$$y = \frac{1}{2} \ln \frac{E + p_L}{E - p_L}, \quad (2.1)$$

where  $p_L$  is the component of the momentum along the beam direction. However, only a small fraction of these events passed the fast, online selection referred to as the “trigger” and were recorded for further analysis. Additionally, it is not possible at DØ to trigger directly on the signal topology,  $B_s \rightarrow \pi D_s(\phi\pi)X$ , shown in Figure 2.1. Data for this sample were collected by requiring a high  $p_T$

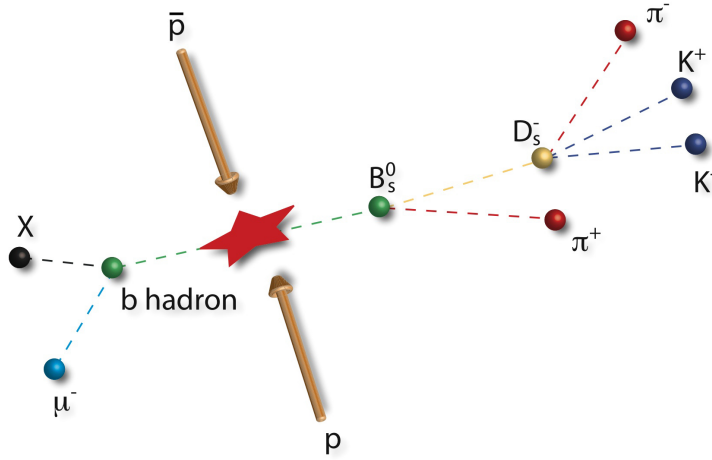


**Figure 2.1:** Decay of a  $B_s$  meson into  $\pi^+ D_s^- (\phi \pi^-)$  on the signal side and a  $b$  hadron, which decays into  $\mu$ +anything on the opposite side.

muon identified at the trigger level from the other B meson in the event ( $\mathcal{B} \approx 11\%$ ). As mentioned above, the signal consists of a  $B_s$  decaying<sup>1</sup> into a  $D_s^-$  and at least an additional pion ( $\mathcal{B} < 13\%$  [6]). The  $D_s^+$  decays into a pion and a  $\phi$  ( $\mathcal{B}(D_s^+ \rightarrow \pi^+ \phi) = (4.4 \pm 0.6)\%$  [6]), while the  $\phi$  instantaneously decays into two kaons ( $\mathcal{B}(\phi \rightarrow K^+ K^-) = (49.2 \pm 0.6)\%$  [6]). Taking into account the branching ratios of the decay  $B_s \rightarrow \pi D_s (\phi \pi) X$  and the muon on the opposite side, about 5700 hadronic decays are expected in the whole dataset<sup>2</sup> – without any detector, trigger or selection efficiencies.

Many decay modes contribute to the  $B_s \rightarrow \pi D_s (\phi \pi) X$  final state. As it is not possible to distinguish between a  $D_s^+$  and a  $D_s^{*+}$  meson within the detector or trigger system ( $D_s^{*+}$  decays into a  $D_s^+$  and a photon with a branching fraction of  $\mathcal{B} = (94.2 \pm 0.7)\%$  [6]), both decays are considered. Sometimes not all particles of a decay are reconstructed. Hence, decays with additional particles will also be selected, like  $B_s \rightarrow D_s^- \pi^+ \pi^- \pi^+$ . The same applies for decays, with a  $\rho$  meson, as this particle decays with a probability of nearly 100% into two pions [6] or with an  $a_1$ , which decays into  $\pi + X$ . Additionally an electron may be misidentified as a pion and can appear as signal candidate. A more detailed view on the signal selection and a list with the exact cuts, used to select the decay from data is described in Chapter 6.

As already stated in Section 1.3, the base distributions for the probability of oscillated  $P^{osc}$  and non-oscillated  $P^{nos}$  events as a function of the true proper time, are given by

$$P^{nos/osc}(t) = \frac{1}{2} e^{-\frac{ct_{B_s}}{c\tau}} [1 \pm \cos(\Delta m_s t)]. \quad (2.2)$$

<sup>1</sup>In the following only one charge correlation is taken into account. Nevertheless, also the charge conjugated states are selected in this analysis.

<sup>2</sup>For this calculation a more recent measurement of the branching ratio of ( $\mathcal{B}(B_s \rightarrow D_s^- \pi^+) = 3.2 \pm 0.9 \cdot 10^{-3}$  [50]) is used, as only an upper limit is given in [6].

## 2.2. Initial State Flavor Tagging

Ideally one would simply determine the initial and the final state of the  $B_s$  mesons to conclude, whether the event has mixed or not. However, in the real world some events are misidentified. While the final state of the  $B_s$  mesons is fixed by the charges of the decay products, the determination of the initial state requires more sophisticated methods. The quality of the tagging method is quantified by the dilution,  $\mathcal{D}$ , which is the asymmetry between the number of correct  $N_{\text{correct}}$  and wrong  $N_{\text{wrong}}$  tagged events

$$\mathcal{D} \equiv \frac{N_{\text{correct}} - N_{\text{wrong}}}{N_{\text{correct}} + N_{\text{wrong}}}. \quad (2.3)$$

The dilution is related to the tagging purity,  $\eta$

$$\eta = \frac{N_{\text{correct}}}{N_{\text{tagged}}}. \quad (2.4)$$

via  $\mathcal{D} = 2\eta - 1$ .

In principle there are two different techniques to determine the initial flavor state of the  $B_s$  meson. If the quark flavor is evaluated through secondary processes on the signal side itself, the method is called same side tagging (SST). For same side tagging the charge correlation of the beauty quark and its fragmentation products is used. It is very likely to have a highly energetic  $K^+$  in close proximity to the  $B_s$  meson (or a  $K^-$  in the case of a  $\bar{B}_s$ ). The same applies for pions, which are produced in  $B^\pm$  and  $B_d$  decays ( $\pi^+$  for  $B^-$  and  $B_d$  and  $\pi^-$  for  $B^+$  and  $\bar{B}_d$ ).

Another option is to take advantage of the fact that beauty quarks are produced as  $b\bar{b}$  pairs in  $p\bar{p}$  collisions, and to identify the charge of the  $b$  hadron on the non-signal side (opposite side). The  $b$  quark of the  $B_s$  meson on the signal side has to be the anti-particle of the  $b$  quark from the  $b$  hadron on the opposite side and therefore tags the initial state. This technique is called opposite side tagging (OST). As the hadronic decay requires a muon on the opposite side to trigger on, every event has an OST. Therefore, the SST technique is not used in this analysis and is not discussed in the following.

The dilution in case of an OST muon is close to one, as the muon charge is easily determinable. Nevertheless, the hadronic decay modes have low statistics, as they require an opposite side  $B \rightarrow \mu X$  decay ( $\mathcal{B} \approx 11\%$ ). A more detailed view of all OST methods and their combination is discussed in Chapter 8.

Including effects of dilution, the probability to observe events with opposite sign (OS) and same sign (SS) initial and final state tags becomes

$$P^{OS/SS}(t) = \frac{1}{2} e^{-\frac{ct_{B_s}}{c\tau}} [1 \pm \mathcal{D} \cos(\Delta m_s t)]. \quad (2.5)$$

If  $\mathcal{D} \approx 1$  OS events contain unmixed, while SS events contain mixed,  $B_s$  mesons. Figure 2.2(a) shows the oscillation probability versus the visible proper decay length for  $\mathcal{D} = 0.57$ . These probabilities still assume the accurate determination of the proper decay time  $t_{B_s}$  and an infinite detector resolution. Figure 2.2(a) shows the oscillation probability versus the visible proper decay length.

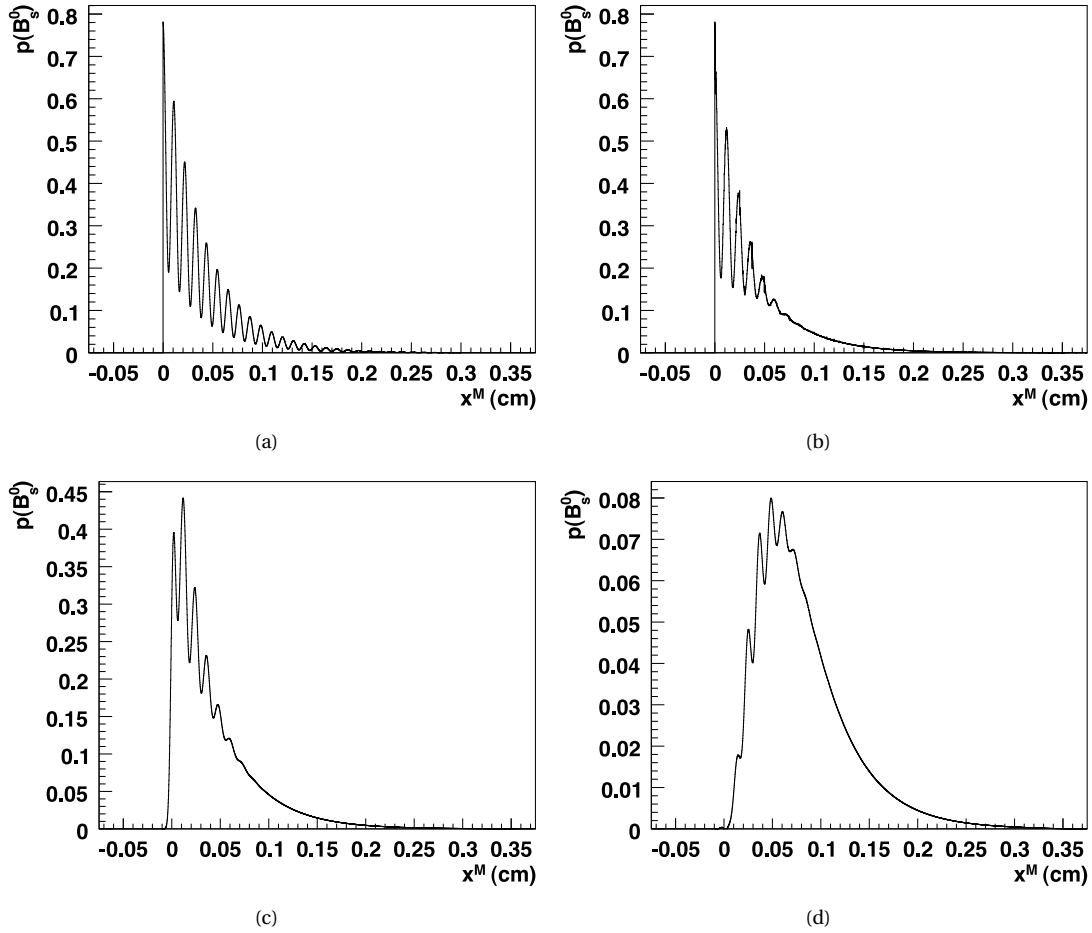


**Figure 2.2:** Effect of the  $k$ -Factor, the resolution and selection efficiency on the probability to observe an oscillation. The probability is plotted versus the visible proper decay length. (a) Probability of an oscillation taking into account the dilution only. (b) Same as (a) plus the  $k$ -Factor uncertainty. (c) Same as before plus smearing due to the resolution. (d) Same as (c) plus effects of the selection efficiency.

### 2.3. Measurement of the Proper Decay Time

By measuring the decay length  $L^B$ , which is the distance between the production vertex and the decay vertex, it is possible to determine the proper decay time  $t_{B_s}$

$$x^M \equiv ct_{B_s} = \frac{L^B}{\beta\gamma} = L^B \frac{m(B_s)c}{p(B_s)}, \quad \text{with } \beta = \frac{v_{B_s}}{c}, \quad (2.6)$$

where  $x^M$  is the visible proper decay length and  $\gamma$  is the Lorentz boost factor. The mass of the  $B_s$  meson is given by  $m(B_s)$  and  $p(B_s)$  is its momentum. It is easier to measure the momentum of the  $B_s$  meson in the transverse plane, the projection

$$x^M = L_{xy}^B \frac{m(B_s)c}{p_T(B_s)} \quad (2.7)$$

is used. Partly reconstructed events are also considered in the signal selection, so a correction for the missing momentum of non-reconstructed particles is necessary. Obviously only the measured

momentum  $p_T(B_{\text{meas}})$  can be used for the determination of the decay time

$$x_{\text{meas}}^M = L_{xy}^B \frac{m(B_s)c}{p_T(B_{\text{meas}})}. \quad (2.8)$$

The correction factor to the real momentum is called the  $k$ -Factor and is defined as

$$k = \frac{p_T(B_{\text{meas}})}{p_T(B_s)}. \quad (2.9)$$

It is used to compensate for the missing momentum of particles, which are not reconstructed. It is determined through Monte Carlo studies. A more detailed explanation on the determination of the  $k$ -Factor is described in section 7.3.1. The visible proper decay length is given by

$$x^M = x_{\text{meas}}^M \cdot k. \quad (2.10)$$

As the momentum of the not detected particles and therefore, the  $k$ -Factor is not known exactly, a probability density function (PDF),  $\rho(k)$ , is applied. This width of this PDF introduces an effective uncertainty on the measurement of the proper decay time of the event. This uncertainty is much smaller for the hadronic decay modes considered here, where few particles are missed, than for the semimuonic decay modes considered in other  $D\bar{O}$  analyses which all have, at least, a missing neutrino. These predicted distributions of measured visible proper decay lengths (Equation 2.5) then become

$$P_k^{OS/SS}(x_{\text{meas}}^M) = \int_0^\infty P^{OS/SS}(x_{\text{meas}}^M \cdot k, \Delta m_s) \rho(k) dk. \quad (2.11)$$

The effect of the  $k$ -Factor on the oscillation probability is illustrated in Figure 2.2(b). In that figure,  $x^M$  is assumed to be measured with infinite precision. However, in the real world, this is not the case; the  $D\bar{O}$  detector has a finite resolution and there is a non-zero uncertainty involved in the measurement of  $x_{\text{meas}}^M$  for each event. The deviation of a measured value of  $x^M$  from its true value is modeled by a Gaussian distribution with standard deviation,  $\sigma_x^M$ . The oscillation probabilities, as a function of  $x_{\text{meas}}^M$  then become

$$P_{k,\sigma}^{OS/SS}(x_{\text{meas}}^M) = \int_{-\infty}^{+\infty} G(x_{\text{meas}}^M - x^M; \sigma_{x_{\text{meas}}^M}) \int_0^{+\infty} \rho(k) P^{OS/SS}(x_{\text{meas}}^M \cdot k) dk dx_{\text{meas}}^M. \quad (2.12)$$

The influence of the resolution on the probability of a pure  $B_s$  state is shown in Figure 2.2(c) assuming  $\sigma_{x^M} = 30.7 \mu\text{m}$ . Finally, the signal selection includes lifetime biasing cuts, which are dependent on the proper decay length  $x_{\text{meas}}^M$ . To take this effect into account Monte Carlo samples are used and an efficiency,  $\epsilon(x_{\text{meas}}^M)$ , is determined by comparing the distributions with the lifetime biasing cuts with the distributions without lifetime biasing cuts. This variable is mostly referred as selection efficiency at  $D\bar{O}$  and is marked as  $\epsilon(x^M)$  in this analysis

$$P_{k,\sigma_{x_{\text{meas}}^M},\epsilon}^{OS/SS}(x_{\text{meas}}^M) = \epsilon(x_{\text{meas}}^M) \int_{-\infty}^{+\infty} G(x_{\text{meas}}^M - x^M; \sigma_{x_{\text{meas}}^M}) \int_0^{+\infty} \rho(k) P^{OS/SS}(x_{\text{meas}}^M \cdot k) dk dx_{\text{meas}}^M. \quad (2.13)$$

Using an  $\epsilon(x_{\text{meas}}^M)$  similar to that found in MC, the oscillation probability distribution changes as illustrated in Figure 2.2(d).

## 2.4. Measurement of $\Delta m_q$

As stated in Equation 1.62 the oscillation frequency  $\Delta m_q$  is accessible by measuring the asymmetry of oscillated and not-oscillated particles. The direct relation between  $\Delta m_q$  and the asymmetry  $A(t)$  is given by

$$A(t) = (2\eta - 1) \cos(\Delta m_q t) = \mathcal{D} \cos(\Delta m_q t). \quad (2.14)$$

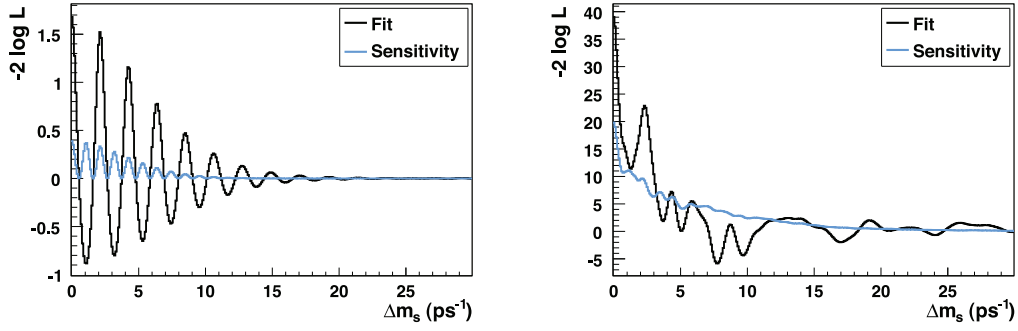


**Figure 2.3:** Black curve: likelihood as a function of  $\Delta m_s$ , blue line: sensitivity. Left: single event. Right: sum over multiple events.

The oscillation frequency is proportional to the dilution  $\mathcal{D}$  and it is not possible to tag the initial state perfectly. Hence, the oscillation in Figure 1.7 diminishes for higher proper decay lengths. Because of the limited vertex resolution and the higher oscillation frequency of  $B_s$  mesons compared to  $B_d$  mesons, this method is only applicable for the measurement of  $\Delta m_d$ .

Another method to obtain the oscillation frequency is the unbinned Log-likelihood fit [51]. For each event the probability that an event has oscillated or not is calculated for a fixed oscillation frequency  $\Delta m_q$  by taking into account the tag, the decay length, the decay length uncertainty, transverse momentum and other event variables. This allows the probability density function for a single event  $i$  to be defined for the assumed  $\Delta m_q$

$$\mathcal{L}_i = -2 \log \frac{P_i^{osc}}{P_i^{osc} + P_i^{nos}}. \quad (2.15)$$

This definition has to be used, as there are about 50% statistical uncertainties on the background shape. It utilizes a projection of the oscillation. This reduces all other effects like background and lifetime to a second order problem, but reduces the sensitivity. However, calculating an event-by-event estimate of the non-oscillating-oscillating asymmetry is the only feasible way to deal with the low statistics in this channel. A more detailed view on this topic can be found in [52]. The probability of the data being consistent with a true oscillation frequency at the assumed  $\Delta m_q$  is found by summing over the probabilities of all single events

$$\log \mathcal{L} = \sum_i \log \mathcal{L}_i. \quad (2.16)$$

If  $\log \mathcal{L}$  is calculated at a variety of different values for assumed  $\Delta m_q$ , a distribution, where the maxima and minima of the single-event distributions cancel out at improbable  $\Delta m_q$ -values and sum up at more probable values. This behavior is illustrated in Figure 2.3 in the case of  $B_s$  oscillations. Another quantity, which is useful in this context is the sensitivity. It describes the ability to distinguish between oscillation and non-oscillation and is the difference between null hypothesis and oscillation probability. The confidence level for a measurement can be determined by checking the crossing of the sensitivity with the  $-2 \log \mathcal{L} = 1$  value for 68% C.L. (confidence level) and at  $-2 \log \mathcal{L} = 2.71(3.84)$  for a C.L. of 90% (95%).

A third method to determine the most probable value of the oscillation frequency is the amplitude scan [53]. The fit to the reconstructed proper time distribution of oscillated and non-oscillated is



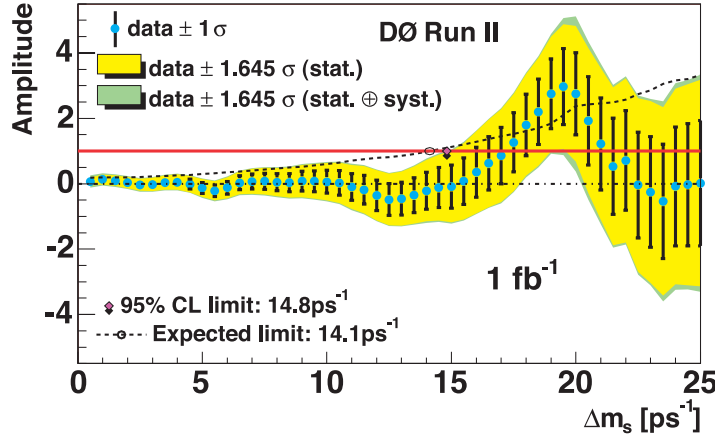


**Figure 2.4:** Amplitude scan for the semileptonic mode  $B_s \rightarrow \mu \nu_\mu D_s(\phi\pi)$  [54]. The blue points represent data with an uncertainty bar of  $1\sigma$ . The yellow band shows the statistical uncertainties, while the green band shows the statistical plus the systematical uncertainties.

performed for a fixed frequency  $\Delta m_q$  of the oscillated term, while its amplitude  $\mathcal{A}$  is left as free parameter. A certain region of  $\Delta m_q$  is scanned and for each value the amplitude is calculated. An amplitude  $\mathcal{A} = 1$  indicates the most probable value for the oscillation frequency. An amplitude scan for the semileptonic mode  $B_s \rightarrow \mu \nu_\mu D_s(\phi\pi)$  [54] is shown in Figure 2.4. However, this method can make no claims about frequency values above the determined sensitivity, but can set lower limits on  $\Delta m_q$ . This ability and the ease with which results from many analyses can be combined for world averages are the two main advantages of using the amplitude method. There is a direct relation between the amplitude scan and the already described likelihood fit

$$-\Delta \log \mathcal{L} = \frac{1 - 2\mathcal{A}}{2\sigma_{\mathcal{A}}}, \quad (2.17)$$

where  $\mathcal{A}$  is the amplitude value and  $\sigma_{\mathcal{A}}$  its uncertainty.

## 2.5. Extraction of $|V_{td}|/|V_{ts}|$

The relation between the oscillation frequency  $\Delta m_d$  for the  $B_d \bar{B}_d$  system,  $\Delta m_s$  for the  $B_s \bar{B}_s$  system and the unitarity triangle side length  $|V_{td}|/|V_{ts}|$  is given by:

$$\frac{|V_{td}|}{|V_{ts}|} = \xi \sqrt{\frac{\Delta m_d}{\Delta m_s} \frac{M_{B_s}}{M_{B_d}}}, \quad (2.18)$$

where  $M_{B_s} = (5367.5 \pm 1.8) \text{ MeV}/c^2$  [6] is the mass of the  $B_s$  meson and  $M_{B_d} = (5279.5 \pm 0.5) \text{ MeV}/c^2$  [6] is the mass of the  $B_d$  meson. The oscillation frequency  $\Delta m_d = (0.507 \pm 0.005) \text{ ps}^{-1}$  is well measured, while  $\xi = 1.210^{+0.047}_{-0.035}$  [11] is a ratio of  $B_s$  and  $B_d$  non-perturbative decay parameters, which are calculated on the lattice with hadronic uncertainties of  $\approx 4\%$ . As the measured variables are uncorrelated, the uncertainty on the measurement of the side length  $|V_{td}|/|V_{ts}|$  is obtained by error propagation

of Equation 2.18:

$$\Delta \frac{|V_{td}|}{|V_{ts}|} = \sqrt{\left( \left( \frac{\Delta m_d}{\Delta m_s} \frac{M_{B_s}}{M_{B_d}} \right)^{\frac{1}{2}} \Delta \xi \right)^2 + \left( \frac{1}{2} \left( \frac{\Delta m_d}{\Delta m_s} \frac{M_{B_s}}{M_{B_d}} \right)^{-\frac{1}{2}} \xi \frac{1}{\Delta m_s} \frac{M_{B_s}}{M_{B_d}} \Delta(\Delta m_d) \right)^2 + \dots} \quad (2.19)$$

$$+ \left( -\frac{1}{2} \left( \frac{\Delta m_d}{\Delta m_s} \frac{M_{B_s}}{M_{B_d}} \right)^{-\frac{1}{2}} \xi \frac{\Delta m_d}{(\Delta m_s)^2} \frac{M_{B_s}}{M_{B_d}} \Delta(\Delta m_d) \right)^2.$$

The LEP experiments at CERN obtained a lower limit of  $\Delta m_s > 14.4 \text{ ps}^{-1}$  (95% C.L.) [55] only. Thus, the measurement of  $\Delta m_s$  is essential to gain further knowledge about  $|V_{td}|/|V_{ts}|$ . The selection of the hadronic mode  $B_s \rightarrow \pi D_s(\phi\pi)X$  is needed for an accurate measurement of  $\Delta m_s$ , as it is fully reconstructable and therefore provides a good measurement of the visible proper decay length, leading to a lower uncertainty, due to the lower  $k$ -Factor. Another advantage at DØ is the efficient muon-trigger, which can be used to select muons on the opposite side, providing an initial state flavor tag at the same time. Therefore the dilution for those events is close to one. The big challenge for these decays is given by the low statistics after reconstruction and event selection. As already mentioned, the Tevatron is currently the only place to study  $B_s$  meson mixing. In the next chapter, the accelerator and the DØ detector are described.

## The Fermilab Tevatron Collider and the DØ Detector

The Fermilab Tevatron collider is currently the only place to study  $B_s$  oscillations worldwide. The two experiments DØ<sup>1</sup> and CDF<sup>2</sup> are located at the Tevatron. DØ operation started in 1992 with the first data taking period ending in 1995 (RunI) having accumulated a dataset of  $\int \mathcal{L} dt = 125 \text{ pb}^{-1}$ . In 2002, after a major upgrade of the collider and the detectors of the experiments, the current data taking period started (RunII). It was interrupted by a shutdown of four months in 2006 for an upgrade to the accelerator and the detectors. The period before the shutdown (RunIIa) ended with  $\int \mathcal{L} dt = 1.3 \text{ fb}^{-1}$  collected. The post-shutdown data taking (RunIIb) is still ongoing. By January 2009 an integrated luminosity of  $\int \mathcal{L} dt = 5.69 \text{ fb}^{-1}$  has been delivered and the DØ detector recorded  $\int \mathcal{L} dt = 4.99 \text{ fb}^{-1}$ . The following chapter will describe the Tevatron collider and the DØ experiment. However, the trigger and data acquisition system is not described on the following pages, but in Chapter 4, which deals with strategies to trigger on events containing hadronic  $B_s$  candidates.

### 3.1. The Fermilab Tevatron Collider

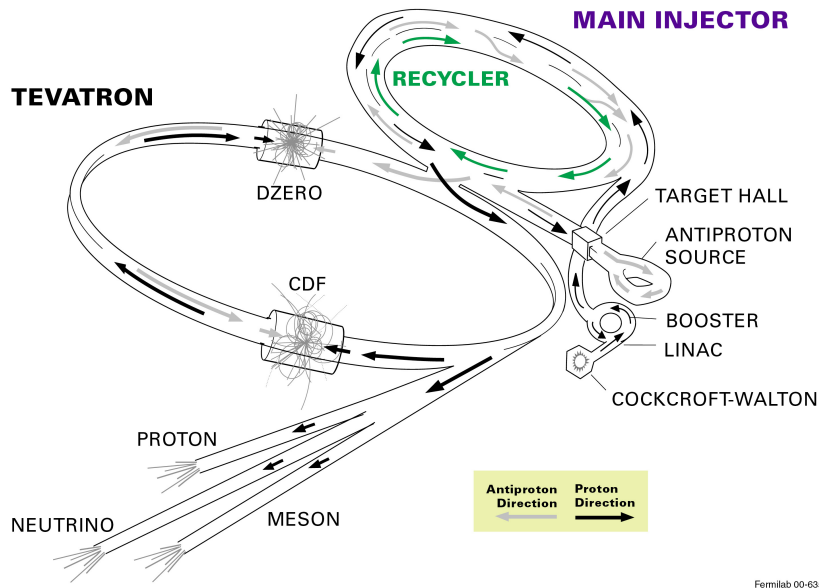
The Tevatron collider [57] is located at the Fermi National Accelerator Laboratory (Fermilab) in Batavia, Illinois, which is about 40 miles west of the city of Chicago, Illinois. Figure 3.1 shows an aerial view of the Fermilab and a schematic view of the accelerator complex. The Tevatron's main collider has a circumference of 6.28 km and provides proton-anti-proton collisions at a center of mass energy of  $\sqrt{s} = 1.96 \text{ TeV}$  at two interaction points, where the two detectors DØ and CDF are located. The acceleration is achieved through several stages. The first stage is a 750 keV Cockcroft-Walton pre-accelerator [58], which ionizes hydrogen gas and accelerates the negative ions. Afterwards the ions are passed into a 150 m long linear accelerator which uses oscillating electrical fields to accelerate the ions to 400 MeV. By passing the ions through a carbon foil, electrons are removed and the charged protons move into the Booster. The Booster is a synchrotron with a circumference of 475 m, accelerating the protons to an energy of 8 GeV, which are then passed into the Main Injector. There are two operational modes. Either the protons are further accelerated to 150 GeV and filled into the collider, or the protons are accelerated to 120 GeV and extracted onto a nickel target

<sup>1</sup>The DØ experiment is named after the intersection DØ of the collider ring

<sup>2</sup>Collider Detector at Fermilab



FERMILAB'S ACCELERATOR CHAIN



Fermilab 00-635

**Figure 3.1:** Top: aerial view of the Tevatron [56] with the two experiments DØ and CDF; Bottom: schematic view of the accelerator chain [56].

over a period of 2.5 s, producing a range of particles including anti-protons which can be collected and stored in the accumulator ring. After the injection to the main ring these anti-protons and the protons are accelerated to their nominal energies of 980 GeV in opposite directions. Each beam has a structure of three so-called super-bunches. The super-bunches themselves show another sub-structure of 12 bunches, consisting of  $27 \cdot 10^{10}$  protons and  $3.4 \cdot 10^{10}$  anti protons per bunch. The spacing between the bunches is 396 ns. Table 3.1 shows an overview of typical Tevatron RunII machine parameters. At the interaction points the beams are collimated to an area of  $\sigma_a \approx 5 \cdot 10^{-5} \text{ cm}^2$  leading to an instantaneous luminosity of

$$\mathcal{L} = \frac{N_p N_{\bar{p}} n_B f}{4\pi\sigma_a}, \quad (3.1)$$

Parameter	Value
circumference Tevatron (main ring)	6.28 km
beam energy after injection	150 GeV
beam energy Tevatron (main ring)	980 GeV
maximum instantaneous luminosity	$312 \cdot 10^{30} \text{ cm}^{-2} \text{ s}^{-1}$
maximum instantaneous luminosity ( <i>design</i> )	$200 \cdot 10^{30} \text{ cm}^{-2} \text{ s}^{-1}$
bunches per beam	36
bunch spacing	396 ns
protons per bunch	$27 \cdot 10^{10}$
anti-protons per bunch	$3.4 \cdot 10^{10}$
transverse emittance of proton beam	$20\pi \text{ mm mrad}$
transverse emittance of anti-proton beam	$20\pi \text{ mm mrad}$
longitudinal size of proton beam	0.63 m
longitudinal size of anti-proton beam	0.54 m
half-life of beam	9-10 h

**Table 3.1:** Typical parameters for the Tevatron in RunII.

where  $N_p$  ( $N_{\bar{p}}$ ) are the number of protons (anti-protons) within one bunch,  $n_B$  is the number of bunches and  $f$  is the collision frequency. Figure 3.2 shows the integrated luminosity accumulated since the start of RunII in April 2002 until today. As indicated by the plateaus, there were four major shutdowns, during the summer months of each year. These are scheduled maintenance and upgrade shutdowns. Throughout operation the accelerator complex was better understood and upgraded, allowing to deliver higher luminosities and thus, the gradient of the integrated luminosity rises. As the number of events is given by the production cross section times the luminosity, a large data set is important for precise measurements or discoveries and searches, like the search for the Higgs boson.

During a shutdown between February and June 2006 the accelerator as well as the detector got a major upgrade. The purpose of the accelerator upgrade was to achieve higher luminosities, while the upgrades to the detector included major changes to the tracking system and the trigger, which will be discussed in the next sections. Since the upgrade of the collider, the luminosities achieved exceed the design luminosity by a factor of 1.5.

### 3.2. The DØ Detector

The DØ detector is one of the two detectors at the Tevatron. It offers the possibility to detect and measure a wide spectrum of physics, like performing searches for the Higgs boson or studying  $B$  physics. Figure 3.3 shows a schematic view of the detector and its sub components. The main purpose of the detector is to detect all kinds of particles in  $p\bar{p}$  collisions. This includes very short-lived particles, which are reconstructed through their decay products as well as long-lived particles, which are directly detected.

The detector is typical of symmetric high-energy experiments. The tracking system, which is described in detail in Section 3.2.1, is located directly around the beam pipe. It consists of a silicon microstrip tracker (SMT) and a central fiber tracker (CFT). Around the tracking system is a superconducting solenoid magnet, which provides a magnetic field of 2 T. The purpose of the inner detectors and the magnet is to detect charged particle tracks and measure their momenta. The tracking

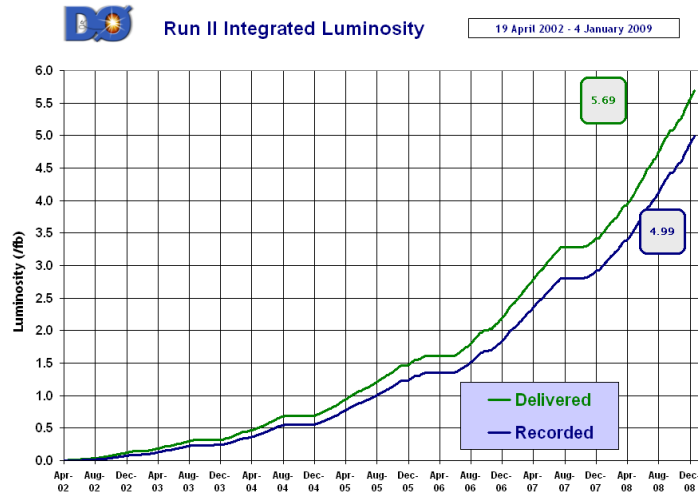


**Figure 3.2:** The integrated luminosity since the start of RunII in April 2002 is shown [59]. The two curves represent the luminosity delivered by the accelerator as well as the luminosity recorded by the DØ detector. The difference between the curves is due to data taking efficiencies, e.g. when a new trigger pre-scale file has to be loaded and the run is paused or when problems with the detector occur. Both curves are comparable to the integrated luminosity delivered to and recorded by the CDF experiment [60].

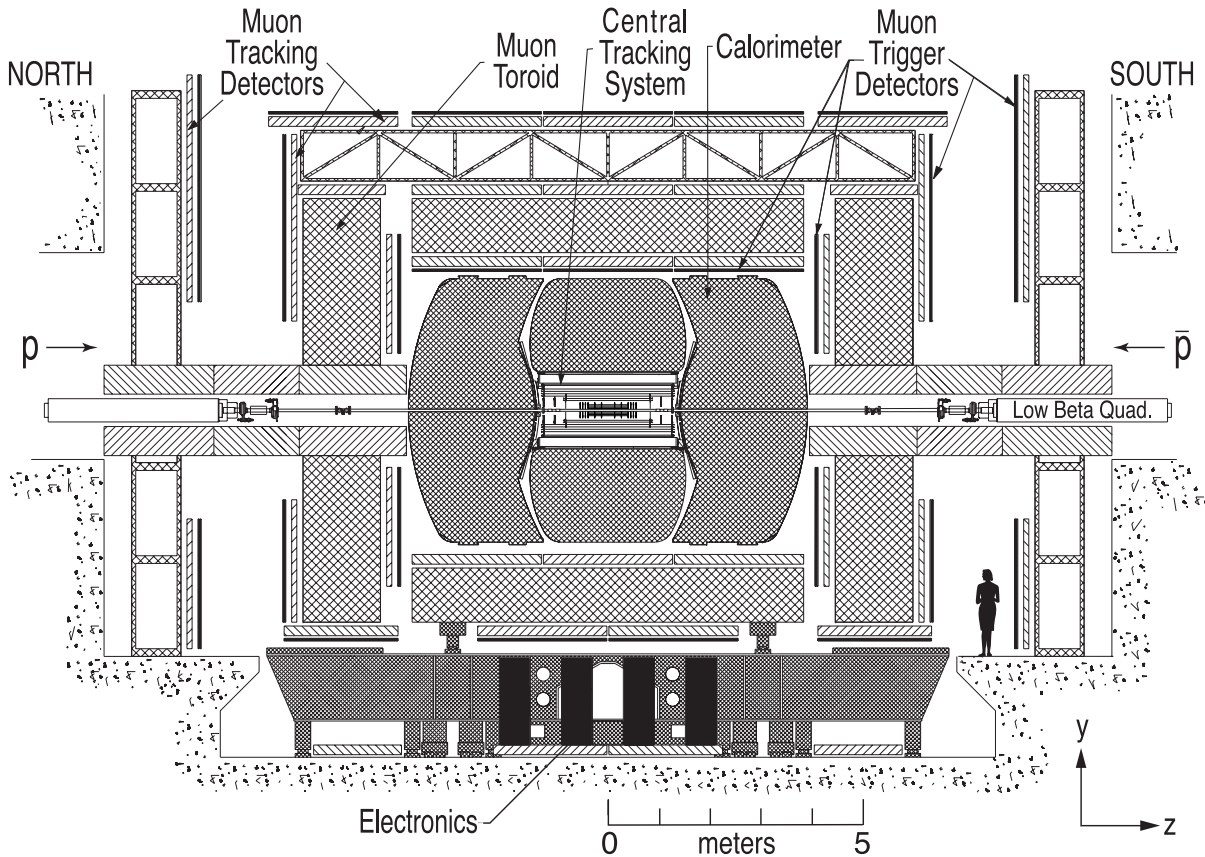


**Figure 3.3:** Schematic view of the DØ detector [61]. In the center of the detector is the tracking system, consisting of SMT, CFT and a solenoid magnet. It is surrounded by a calorimeter, which uses liquid argon as active material and uranium as absorber material. The muon system encloses the calorimeter. It is made up of three layers of muon chambers, where in between the first and the second layer a toroid magnet is positioned.

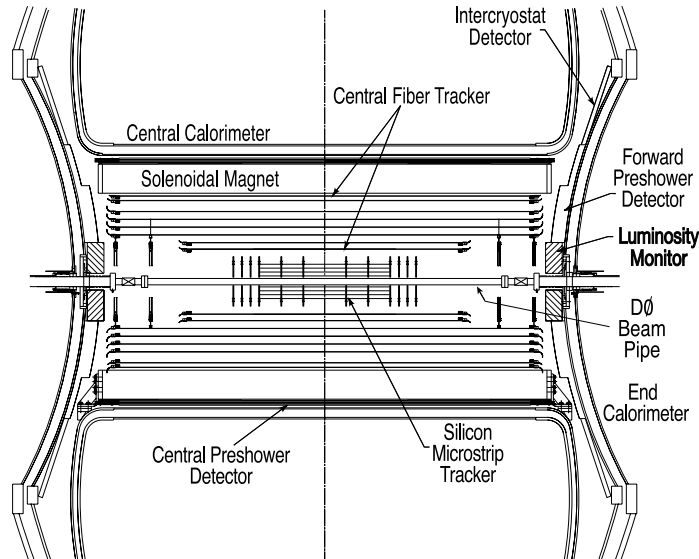


**Figure 3.4:** Magnified view of the DØ tracking system [61]. The beam pipe is located in the center and surrounded by the SMT and CFT. These detectors are embedded in a solenoidal magnet. In the forward region are the forward preshower detector and the luminosity monitors.

system is enclosed by a pre-shower detector and the electromagnetic and hadronic calorimeters (Section 3.2.2). A first layer of muon chambers (Section 3.2.3) surrounds the calorimeter. A second magnet (Section 3.2.3), which creates a toroidal field, is placed around this muon layer. The muon tracking system is completed by two more layers of muon chambers. All the data from the detectors is passed to a three level trigger system and finally to data acquisition (Chapter 4).

The coordinate system used at DØ is centered at the nominal interaction point of both beams. In a cartesian coordinate system the  $z$ -axis is in the direction of the protons in the beam pipe. The  $y$ -axis points upward and the  $x$ -axis is defined to result in a right-handed coordinate system. But usually the coordinate tuple  $r, \phi, \eta$  is used, where  $\phi$  is the azimuth angle and  $\eta$  is the pseudo rapidity, which is given by the polar angle  $\theta$  through the equation:

$$\eta = -\ln \left( \tan \frac{\theta}{2} \right). \quad (3.2)$$

The origin of  $\eta = 0$  is in the center of the detector, where the positive direction is defined in the direction of the proton beam. For the azimuth angle  $\phi = 0$  is pointing upwards. Only the parts relevant for this analysis are described in detail in the following sections. The complete detector is described in detail elsewhere [62].

### 3.2.1. Tracking System

The main purpose of the tracking system is a good measurement of tracks and vertices. A detailed schematic view of the tracking system is shown in Figure 3.4. It consists of the silicon microstrip tracker and central fiber tracker, which reside inside a solenoid magnet. It provides a resolution on the position of the primary interaction vertex of  $35 \mu\text{m}$  and of  $10 \mu\text{m}$  on the impact parameter measured for high  $p_T$  tracks in the transverse plane.



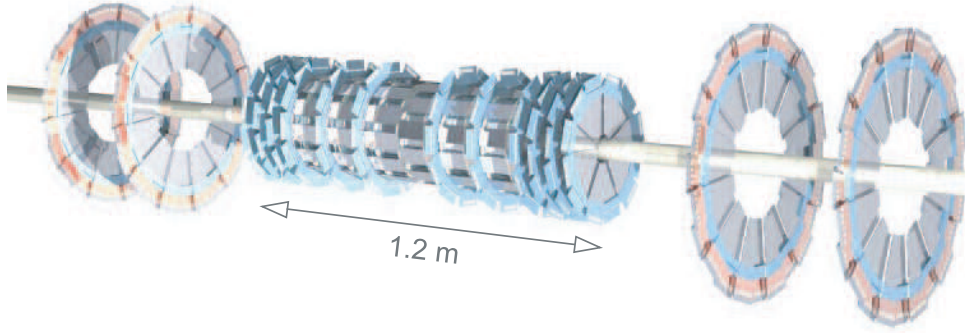


**Figure 3.5:** Schematic three-dimensional view of the silicon microstrip tracker [61]. Shown is the barrel structure in the center of the detector with the surrounding F-Discs. In the forward and backward directions are the larger H-Discs.

	Central Barrels (4)	Outer Barrels (2)	F-Discs	H-Discs
Number of modules	216	216	144	96
Pitch ( $\mu\text{m}$ )	50/153.5 (1,3) 50/62.5 (2,4)	50 (1,3) 50/62.5 (2,4)	50/62.5	40 (inner) 80 (outer)
Length (cm)	12 (1,3) 6 (2,4)	6	7.9	7.6 (inner) 6.3 (outer)
Inner radius (cm)	2.7 (1,3) 4.6 (2,4)	2.7 (1,3) 4.6 (2,4)	2.6	9.5
Outer radius (cm)	7.6 (1,3) 10.5 (2,4)	7.6 (1,3) 10.5 (2,4)	10	26

**Table 3.2:** Overview of the components of the silicon microstrip tracker. The barrel is divided into six parts, where four parts build the central barrel and two parts the outer barrel. If silicon chips are mounted on both sides the pitch is given for both sides. For the barrels (1,3) is related to layers one and three, while (2,4) means layers two and four. The inner H-discs have slightly different dimensions. They are marked as inner and outer, related from the center of the detector.

### Silicon Microstrip Tracker

The high-resolution SMT (Figure 3.5) is located directly around the beam pipe in the center of the detector. It provides three-dimensional tracking with a good acceptance for high  $p_T$  tracks. Within the barrel it consists of four double-sided layers of silicon. The innermost layer has an inner radius of 2.7 cm, while the outer radius is 10.5 cm. The barrel region is divided into six modules, each having a length of 12 cm.

Between each module and at the end of the barrel are 12 so-called F-discs, built from double-sided silicon and having a radial dimension of 2.6–10.5 cm (see table 3.2 for details). To also obtain information in the forward direction up to  $|\eta| < 3$  two H-discs are centered on each side around the beam pipe with a distance of 110 cm and 120 cm in between the discs. The H-discs are made of single-sided silicon. A spatial resolution of  $16\mu\text{m}$  is achieved in the  $r - \phi$  plane, by combining the information of two layers. About 800000 channels have to be read-out to obtain the whole data of the SMT.

For RunIIb another layer was put directly next to the beam pipe. It is called Layer0 [63], [64] and it is made of two silicon layers. The dimensions during construction were limited by the beam



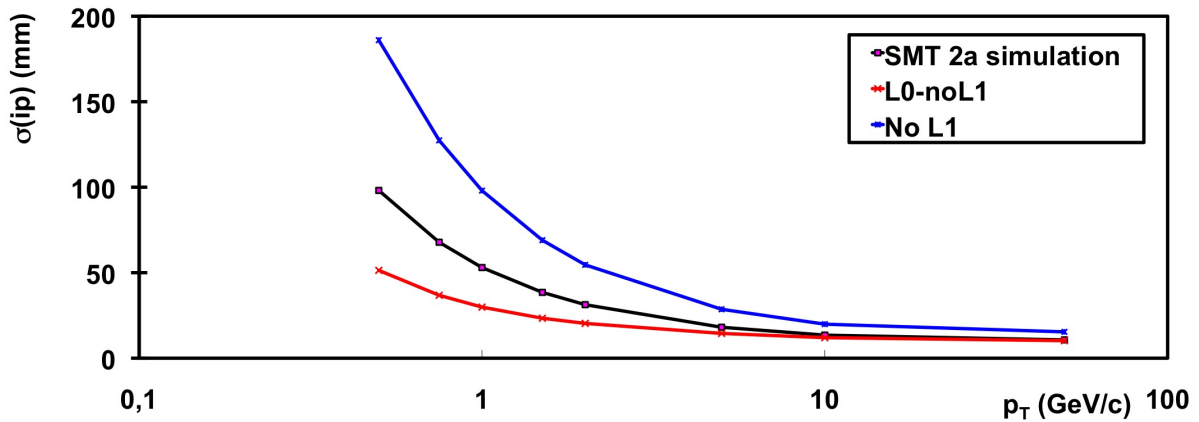


**Figure 3.6:** The three lines show simulations of the impact parameter resolution as a function of the transverse momentum of the tracks. The black line with the squared markers shows the performance of the RunIIa detector. The other two lines correspond to simulations with total loss of the innermost layer-1 of the RunIIa detector, due to radiation damage: one with the addition of Layer-0 (triangles) and one without (circles). [63].

pipe diameter of  $d=30.48$  mm and an aperture with a diameter of  $d=44.04$  mm. Its purpose is to significantly increase the impact parameter resolution, as shown in Figure 3.6, where the tracking performance of the RunIIa tracking system is compared with the resolution, as it is obtained with the additional tracking layer. Furthermore, it counteracts the degradation of the tracking system, due to dead channels caused by radiation.

### Central Fiber Tracker

The SMT is surrounded by the CFT and covers a region of  $|\eta| < 2$ . It is built of scintillating polystyrene fibers with a diameter of  $835 \mu\text{m}$ . The scintillating fibers are assembled into ribbons consisting of 256 fibers in two layers (Figure 3.7), each layer shifted by half a fiber width to avoid gaps. The ribbons build a barrel around the SMT, where always two cylindrical structures build a layer. One of these layers is in parallel to the beam axis, the other layer has an angle of  $\pm 3^\circ$  with respect to the beam axis. There are eight layers, labelled from A-H. The sign of the twist is alternating. An overview of all layers is given in Table 3.3. A more detailed explanation on the functional principle of fiber trackers can be found in [65].

### Solenoid Magnet

To obtain a measurement of the particle momentum the tracks must be bent in a magnetic field. This is achieved by a solenoid magnet with a 2 T magnetic field, surrounding the tracking system. The magnet has a length of 2.8 m and consists of two layers of coils having a radius of 0.6 m. During its operation it is cooled down to 2.8 K to achieve a superconducting state and it is energized with 4.7 kA. The relative fluctuations of the magnetic field inside the tracking volume are smaller than 0.5%. This uniformity is achieved without an iron core by using two different kinds of conductors at the end of the coils with high current density. The material of the solenoid magnet in combination with the cryostat wall comprises 1.1 interaction lengths.

Layer	Radius (cm)	Number of fibers	Fiber separation ( $\mu\text{m}$ )	Active length (m)
A	20.04	2560	982.4	1.66
Au	20.22	2560	990.3	1.66
B	24.93	3200	978.3	1.66
Bv	25.13	3200	985.1	1.66
C	29.87	3840	976.1	2.52
Cu	30.05	3840	980.9	2.52
D	34.77	4480	974.4	2.52
Dv	34.95	4480	979.3	2.52
E	39.66	5120	971.7	2.52
Eu	39.86	5120	976.3	2.52
F	44.56	5760	970.0	2.52
Fv	44.74	5760	974.3	2.52
G	49.49	6400	969.8	2.52
Gu	49.67	6400	973.3	2.52
H	51.97	7040	926.1	2.52
Hv	52.15	7040	927.8	2.52

**Table 3.3:** Number of fibers and location of all eight layers of the CFT. Each layer consists of two sub-layers with a twist of  $\pm 3^\circ$ . The sign is given by  $u = +3^\circ$  and  $v = -3^\circ$ .

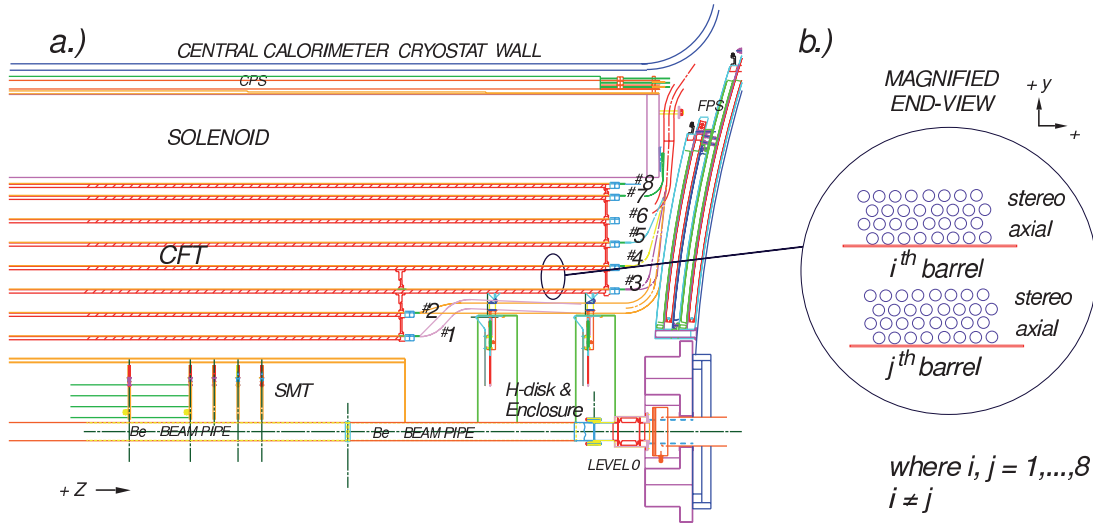


**Figure 3.7:** Schematic view of the CFT. The left-hand side figure shows the side view on the CFT, while the right-hand side figure shows the front view to illustrate the mounting of the fibers [61].

### 3.2.2. Calorimeter

The DØ calorimeter is made up of three parts: the central calorimeter (CC) and two end caps (ECS and ECN). Each of these by itself is divided into three parts, namely an electromagnetic, a fine and a coarse hadronic calorimeter. An inter-cryostat detector is located between CC and ECS and between CC and ECN. Liquid Argon is used as active material and uranium is used as absorber material to generate particle showers. The CC has a thickness of 7.2 interaction lengths  $\lambda_0$ .

The calorimeter of the DØ detector is not used in this analysis and thus is not described here. Refer to [62] for a detailed description. For the hadronic mode the only purpose is to act as block of matter and shield all kind of particles to ensure that only muons and neutrinos penetrate the muon system located around the calorimeter.

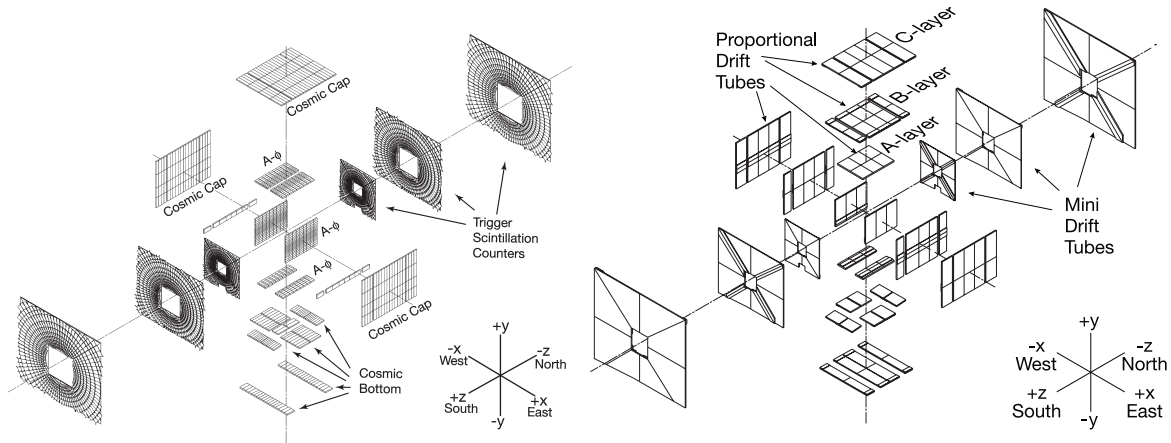


**Figure 3.8:** Illustration of the DØ muon system. Left plot: scintillators, Right plot: proportional drift tubes [61].

### 3.2.3. Muon System

The DØ muon system (Figure 3.8) is composed of a central region (CF), covering  $|\eta| < 1.5$ , and a forward region (EF), extending the coverage up to  $|\eta| < 2.0$ . Both regions consist of three layers labeled A, B and C. While the A-layer follows directly the calorimeter and is inside the toroidal magnetic field, the outer two layers are outside of this magnet. This allows a momentum measurement of the muons, which is independent of the tracking system.

#### Muon System Layers

The central muon chambers consist of proportional drift tubes (PDT), which are filled with a gas-mixture of 84 % argon, 8 % freon ( $\text{CF}_4$ ) and 8 % methane ( $\text{CH}_4$ ). Each tube consists of an aluminum casing with an anode wire made out of tungsten and coated with gold. Voltages of 5 kV and 2.5 kV are connected to the anode and the cathode. Depending on the position 14 or 24 tubes build a muon chamber having a length between 191 cm and 579 cm. The A-layer consists of four layers of drift tubes per chamber, while the B-layer and the C-layer have three layers each. Additionally, there is another layer of muon scintillators in the central region in front of the A-layer and behind the C-layer. Scintillators are often used in muon systems due to their fast signal response.

As support structures are necessary to keep the calorimeter in place, it is not possible to cover the whole central detector region. As a result there are some chambers missing in the  $\phi$ -region  $4^\circ < \phi < 5^\circ$ .

The forward region of the muon system is built of mini drift tubes (MDT). Their walls are made of plastic, have a cross section of  $10 \times 10 \text{ mm}^2$  and are filled with the same gas mixture as the PDTs. The layer structure is the same as in the central region. Each layer in the forward region has another layer of scintillators with a segmentation of  $0.1 \times 0.08$  in  $\eta \times \phi$ . The drift chambers in forward direction achieve a resolution of  $\approx 350 \mu\text{m}$ . An efficiency plot for the differently sized muon trigger scintillation counters is shown in Figure 3.9.

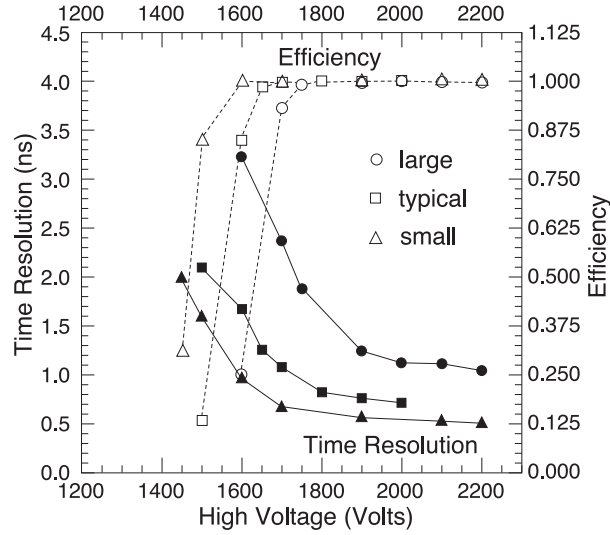


**Figure 3.9:** Time resolution and detection efficiency of muon trigger scintillation counters. Large counters are  $60 \times 60 \text{ cm}^2$ ; typical counters are  $24 \times 34 \text{ cm}^2$ ; small counters are  $17 \times 24 \text{ cm}^2$  [61].

### Toroid Magnet

The toroid magnet [66] consists of three parts, which are located between the A-layer and the B-layer of the muon system. The toroid magnet is divided into a central magnet and one magnet in each forward direction. The central magnet is centered around the beam pipe at a distance of 317.5 cm. Both forward toroid magnets are in a distance of  $447 \text{ cm} < |z| < 600 \text{ cm}$  from the center of the detector. All three parts are energized by a current of 1.5 kA. The magnetic field generated by the iron in the central toroid has an average of 1.8 T and the average magnetic field of the forward magnets is 1.75 T.

## The DØ Trigger System

The collision energy of  $\sqrt{s} = 1.96 \text{ TeV}$  allows to produce all kind of  $b$  hadrons (e.g.  $B_s$ ,  $B_c$  and  $\Lambda_b$ ) at the Fermilab Tevatron Collider and thus provides the possibility to measure various  $B$  physics processes, in particular the discovery of new physics and  $B_s$  mixing. However, at a hadron collider, the inelastic cross section is 3 orders of magnitude larger than the  $b\bar{b}$  cross section, with a  $p_T$  spectrum which is approximately the same. Figure 4.1 compares the  $p_T$  spectrum of  $B_d$  decay products and minimum bias events in Monte Carlo. The challenge of developing highly efficient triggers is obvious – the  $p_T$  distribution is shifted just a little bit to higher  $p_T$  values, compared to the minimum bias events. Figure 4.2 shows an event display of a signal candidate and demonstrates the difficulty of separating interesting from non-interesting events, due to the high amount of particle tracks.

Another limitation is the maximum tape storage rate. During RunIIa the detector collision rate of 2.5 MHz had to be reduced to a data acquisition rate to tape of 50 events per second. This limit has been raised to 100 Hz during an upgrade for RunIIb. Of course, all physics groups share the output rate to tape. Certain physics phenomena have different signatures and therefore different trigger requirements. They are in competition each time the trigger list changes. In the beginning of RunIIa, when the data acquisition rate was limited to 50 Hz about 2-3 Hz were reserved for  $B$  physics events. However, with RunIIb the rate to tape was increased by a factor of two and the situation is more relaxed and there is no explicit bandwidth allocation anymore.

### 4.1. Functional Principle of the Three Level Trigger System

The DØ trigger system uses three levels<sup>1</sup>. A schematic view of the trigger system is shown in Figure 4.3. The data of the detector is stored in a buffer and passed to the Level 1 trigger in parallel. The buffers are required, as the trigger decision takes some time. If the trigger decision is positive, a Level 1 accept is called by the trigger framework and the content of the buffer is passed to Level 2. The Level 1 accept rate is limited to approximately 1.5 kHz. If the trigger decision is negative, the contents of the corresponding Level 1 buffer are discarded. The same mechanism is used at Level 2:

<sup>1</sup>Actually, there is also a Level 0, which consists of the luminosity monitors mounted symmetrically around the beam pipe, on the inside of the end calorimeters. Its purpose is to trigger on inelastic  $p\bar{p}$  collisions.

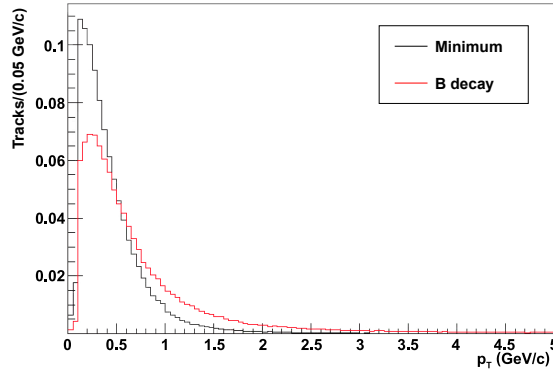


**Figure 4.1:** A comparison of the  $p_T$  spectrum of  $B_d$  decay products and minimum bias events in Monte Carlo [67]. The challenge of developing highly efficient triggers is obvious – the  $p_T$  distribution is shifted just a little bit to higher  $p_T$  values, compared to the minimum bias events.

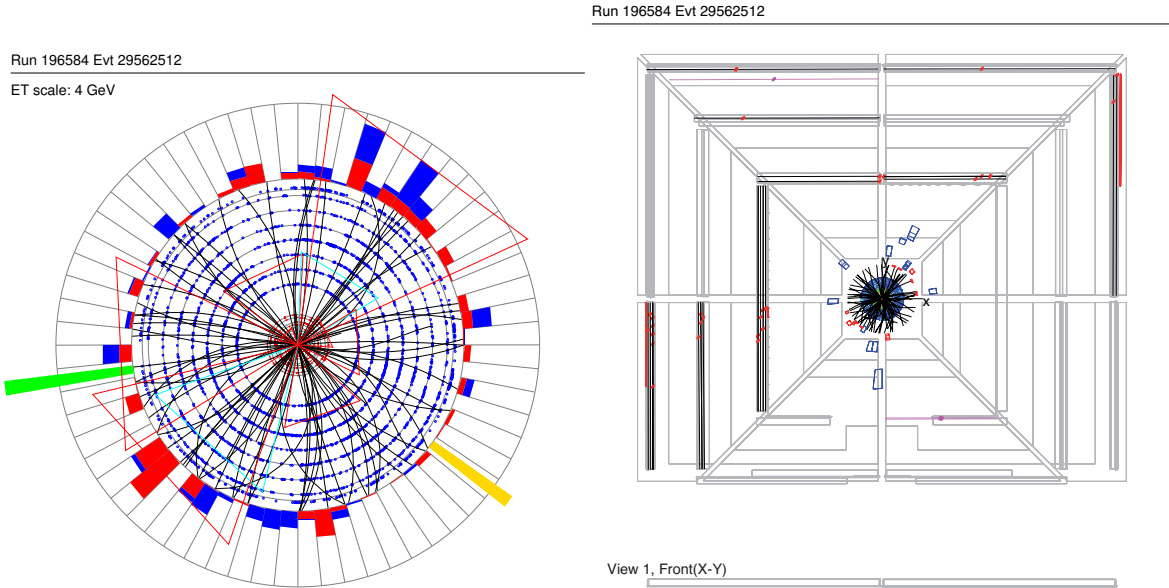


**Figure 4.2:** DØ event display [68]. Left: Projection end view (along the direction of motion of the proton beam) of the collision, with charged particle tracks in the silicon detector, the energy deposited in the calorimeters, and possibly hits in the muon detectors. The inner part, with the concentric circles, shows the locations, to scale, of the tracking detectors. Hits are shown as small circles. The outer concentric ring is a histogram of deposited energies, summed over the eta range shown. Right: View of the muon system in the x-y plane. The large grey areas are the outlines of the various outer muon detectors. Red marks represent the positions of detectors activated by particles.

if any Level 2 trigger condition is matched, the corresponding buffer contents are passed to Level 3 with an average rate of 800 Hz. Candidates fulfilling the requirements of Level 1 and Level 2 are sent to a farm of Level 3 PCs, which run sophisticated algorithms to reduce the rate to 50 Hz (this limitation was raised to 100 Hz during the RunIIb upgrade). The overall coordination and control of the DØ triggering is handled by the COOR package [69]. COOR interacts directly with the trigger framework (Level 1 and Level 2) and with the data acquisition (DAQ) supervising system for the Level 3 triggers.

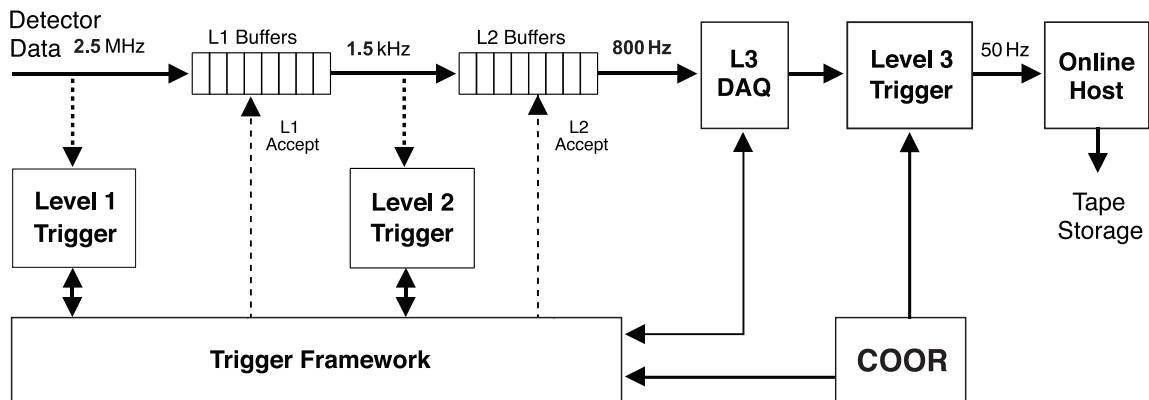


**Figure 4.3:** The DØ three level trigger system (slightly adapted from [61]). The input rate from the detector of 2.5 MHz had to be reduced to a data acquisition rate of 50 Hz during RunIIa and is now at 100 Hz. The first two trigger levels are implemented in hardware, while the last stage runs on a PC-Farm. On each level trigger decisions are made and only if an event is accepted, it is passed to the next trigger level.

As it is not possible to trigger on tracks coming from displaced vertices at DØ, the task of triggering hadronic  $B_s$  decays is very challenging. The only way to trigger these decays is through a muon. However, the wide muon chamber coverage up to  $|\eta| < 2$  allows for very efficient triggering on semimuonic decays. Since no muons are present for hadronic  $B_s$  decays, the muon can only stem from the  $B_s$  decay on the other side, as illustrated in Figure 2.1. Because this muon also tags the initial state of the  $B_s$  meson, the success of these channels depends on the optimization of the muon triggers [70] at all three stages.

#### 4.1.1. The First Trigger Level

The first level is a pure hardware trigger, where the logic is programmed into FPGAs<sup>2</sup>. The decision is based on four sub-components: the Level 1 muon trigger (L1MUO), central track trigger (L1CTT), calorimeter trigger (L1CAL) and forward proton trigger (L1FPD). These components are illustrated in the middle column of Figure 4.4. The muon trigger receives the information from the muon chambers. The Level 1 central track trigger reads out the data from the CFT, while the Level 1 calorimeter trigger obtains its information from the calorimeter and the forward proton trigger gets the information from the forward proton detector.

The Level 1 muon trigger was designed to identify muon candidates and to report them to the trigger framework. For this purpose segments of the muon chambers (Section 3.2.3) are combined into a grid. The A-layer has a segmentation of 9 segments in the  $z$  direction and of  $4.5^\circ$  in  $\phi$  for the proportional drift tubes (which is the same segmentation as for the central track trigger in  $\phi$ ). The scintillation trigger counters also have a segmentation of  $4.5^\circ$  in  $\phi$ , but of  $\approx 0.11$  in  $\eta$ . If a muon candidate is accepted at Level 1, this event will be processed by the next trigger level. To build the muon candidate and/or logical modules are used, which combine information of the 3-layer muon chambers and the central fiber tracker (CFT). This information is processed and combined into regional triggers. Finally, global muon trigger decisions are formed and passed to the trigger

<sup>2</sup>FPGA = Field Programmable Gate Array

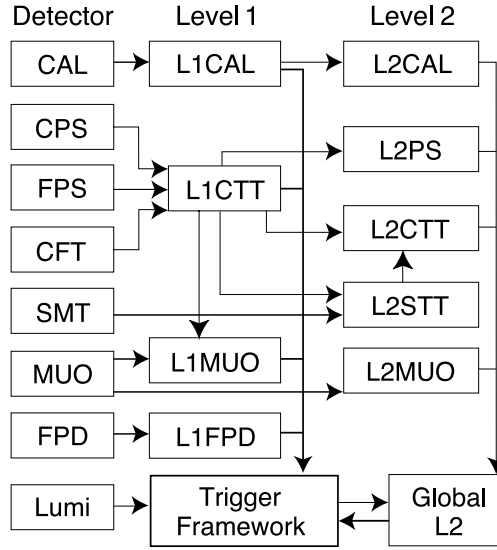


**Figure 4.4:** This flowchart [61] shows the signal paths of the detector sub-components to the corresponding Level 1 and Level 2 components. Each component of the Level 1 trigger matches one component of the Level 2 trigger. Additionally, Level 2 has the information of the SMT available (L2STT). The information of the luminosity monitors, which is also known as Level 0, the information of all Level 1 components plus the global trigger decision of Level 2 is passed to the trigger framework.

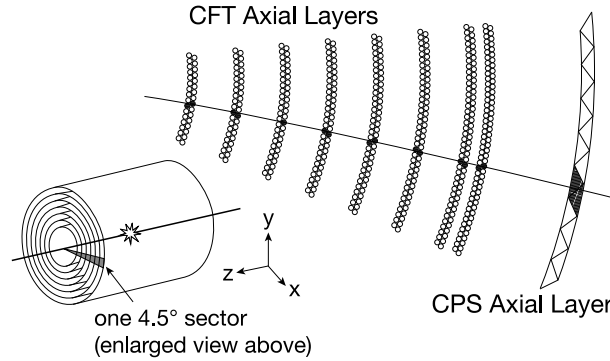


**Figure 4.5:** The central track trigger is divided into 80 sectors, each covering a region of  $4.5^\circ$  [61].

framework. Level 1 can perform selections by multiplicities,  $p_T$  thresholds, regions, scintillator timing, wire hits or additional options like opposite/same sign of tracks, mass ranges or layer (A, B or C) hits. For the central track trigger a region of  $|\eta| < 2$  of the CFT is used and divided into 80 sectors (Figure 4.5), which match the  $\phi$  segmentation of the muon chambers. To operate the trigger in RunIIa four thresholds for the transverse momentum  $p_T$  were programmed into the FPGAs ( $p_T > 1.5, > 3, > 7, > 11 \text{ GeV}/c$ ). This has changed for RunIIb. Two more thresholds were added and the stepping has changed to  $p_T > 3, > 3.75, > 5, > 5.7, > 8, > 13 \text{ GeV}/c$ . A more detailed view of all changes for RunIIb is given in [71].

At this stage trigger decisions are based on simple kinematic attributes, like transverse momentum. The output rate of Level 1 is 1500 Hz. Due to the short time limit it is not possible to use any information of the SMT, which data is passed directly to the second trigger level.



### 4.1.2. The Second Trigger Level

All data from Level 1 is re-defined at Level 2. This is illustrated in Figure 4.4. Each component of the Level 1 trigger matches one component of the Level 2 trigger. Additionally, Level 2 has the information of the SMT (L2STT) available. This trigger stage has a finer granularity and the complete time information available – including calibrations. Therefore, it improves the Level 1 correlation between muon scintillators and wire hits. The information of all sub-components is combined in the Level 2 global trigger. At this stage a quick reconstruction of physical objects is possible and a trigger decision is based on these objects. It has to happen within  $100\mu\text{s}$  (due to the reduced input rate at Level 2 the time-frame for the trigger decision is longer) and the rate is reduced to 800 Hz. This stage is implemented in FPGAs, DSPs and micro processors. The processing of muons at Level 2 happens in three stages, where each stage has a time budget of  $30\mu\text{s}$ :

1. The second level input computer (SLIC) cards receive fast calibrated data from the front end and Level 1 output. Level 1 objects are transformed into Level 2 format and the front end data is processed into A-layer and BC-layer individual track segments.
2. All segments found are passed to the Alpha pre-processor. It searches for A+BC-layer matches, calculates momenta, assigns a track quality (see section A.2 for definitions of loose and tight muons at Level 2) and adds a time stamp (prompt, slow, out of time). This time stamp classifies the coincidence of the hits in the muon chamber layers.
3. The Level 2 global system collects data from all Level 2 subsystems. It is the first DAQ instance which has access to the whole event and can base trigger decisions on correlations of different Level 2 objects.

The Level 2 muon trigger is not just a rejection tool, but is also an essential pre-processing stage for Level 3, as the third trigger level will not unpack and scan the full muon detector readout, but will only unpack those modules in the neighborhood of tracks reported by Level 2.

### 4.1.3. The Third Trigger Level

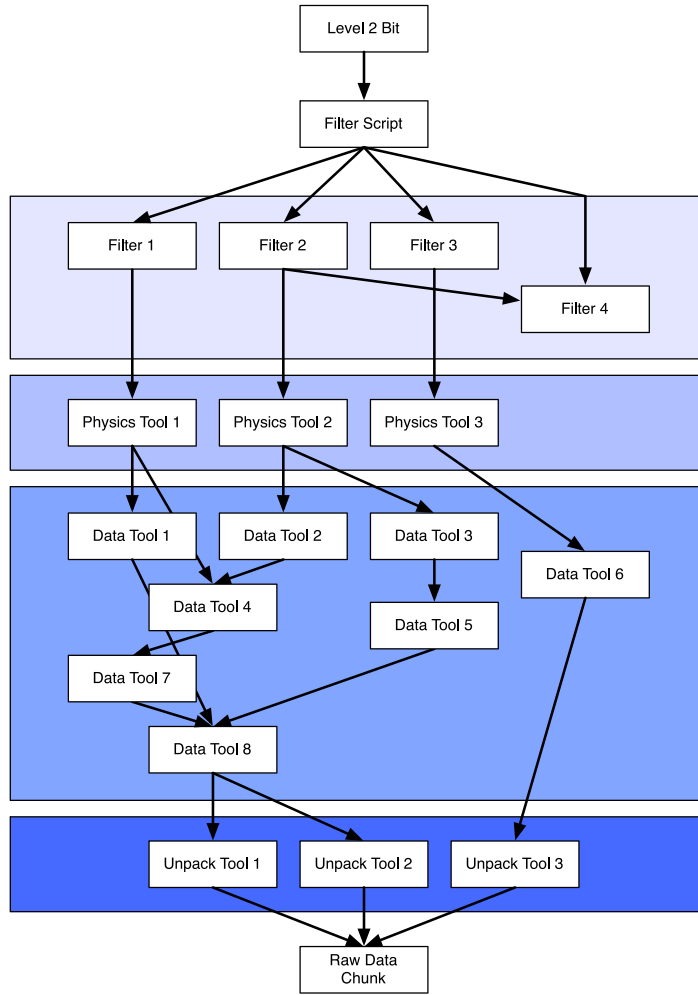
If the Level 2 global trigger accepts an event it is passed to the third and last stage of the DØ trigger system. This trigger level consists of C++ programs running on a PC-farm. It allows easy scaling of the trigger power by adding further machines to the cluster. In principle the C++ programs use filters to apply simple kinematic cuts and afterwards use subroutines, called “physics tools” to identify electrons, jets, tracks etc. These objects are combined in the “data tools” and physical objects like invariant masses are built, upon which trigger decisions can be based.

Figure 4.6 illustrates the hierarchy of the Level 3 framework. Each Level 2 trigger bit relies on at least one Level 3 filter script<sup>3</sup> and the total amount of scripts is only limited by computing power. Each filter script can run several filters<sup>4</sup>, which are most likely physics tools<sup>5</sup>: cuts are applied on properties assigned to particles. But also relational filters are possible, which compare the output of other filters and set a Level 3 trigger bit depending on their result. Physics tools run in general at least one data tool. They provide the tracking, vertexing and clustering computations. Data tools can call other tools and their results are cached to optimize the performance, if a data tool is called multiple times. The only way to access raw detector data is to call an unpack tool, as these are the only instances which can unpack the data and provide the information.

<sup>3</sup>Filter script is the DØ trigger group terminology for Level 3 trigger.

<sup>4</sup>This is a collection of tools which are run when a particular trigger bit is set and decide whether or not to pass the event.

<sup>5</sup>These are the objects responsible for creating the physics objects which are then used to pass or fail the event. The functionality of the tools differs slightly from Level 2 to 3 but in essence, these tools use input data in conjunction with the tool's parameters, to create physics objects.



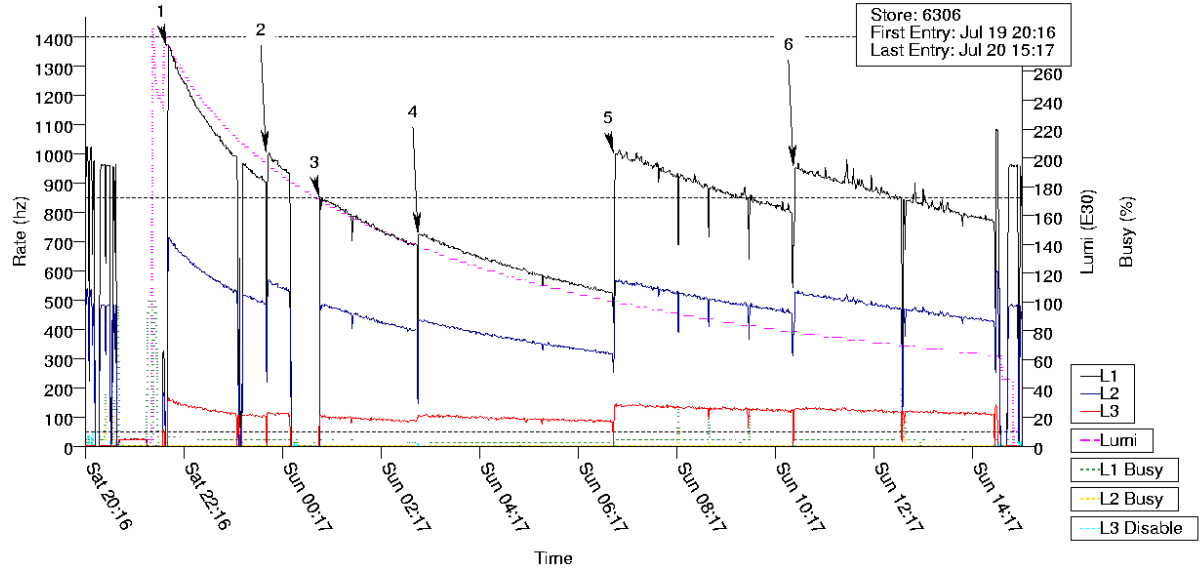
**Figure 4.6:** Level 3 flowchart (adapted from [72]). Each Level 2 trigger bit relies on at least one filter script, which can call several subroutines to identify particles, jets and tracks to apply trigger conditions or build physical objects like invariant masses. If a result is needed for other filters, it can be cached into a data tool. Unpack tools are the only instances which can directly unpack and access the raw data.

The Level 3 muon trigger has the full detector information available and analyzes interesting regions defined by Level 2. It utilizes the aspects of the offline muon reconstruction and assigns tracks from the central fiber tracker and silicon microstrip tracker to tracks from the muon chambers. In principle the definition of a muon follows the following constraints:

- one muon with two wire hits or one scintillator hit in the A-layers,
- two wire hits and one scintillator hit in BC-layers,
- a central track match with  $p_T$  cut.

But also physical objects<sup>6</sup> like invariant masses or trigger constraints like impact parameter cuts can be implemented as trigger decisions. The script runner takes a trigger list as input and initializes all

<sup>6</sup>An object is a collection of parameters. Each object type has a structure which lists all its parameters and, possibly, their default, minimum and maximum values. To use C/C++ terminology: an object can be considered as an instance of a class or struct.



	Run	Duration (h)	inst. Lumi ( $10^{30} \text{ cm}^{-2} \text{ s}^{-1}$ )	Tape Rate (Hz)	Presages File
1	244016	2.00	283.8	111.8	260-300E30
2	244017	0.49	198.6	103.5	150-200E30
3	244025	1.99	173.1	88.0	150-200E30
4	244026	3.97	140.1	88.9	100-150E30
5	244027	3.64	101.0	101.1	80-100E30
6	244028	4.08	79.5	0	60-80E30

**Figure 4.7:** Trigger rates for all three trigger levels. During a store the luminosity drops from the highest instantaneous luminosity value directly after beam injection to the lowest value, before the beam is dumped (magenta line). The trigger rates for Level 1 (black line), Level 2 (blue line) and Level 3 (orange line) are monitored. The rates are continuously monitored. If they have dropped below a certain value, a new run is started and the appropriate trigger menu is loaded (indicated as steps 1-6 in the figure and the table). This results in an increase of the trigger rate and ensures the maximum allowed rate is stored to tape. The table shows typical numbers for a span of time for a run, the instantaneous luminosity at the beginning of a run, the averaged tape rate during a run and the used prescale file, which are named after their operational luminosity region.

required tools. If a Level 2 bit is set, it executes the dependent filter scripts. In the case all filters are passed, the event passes that trigger. Any event passing at least one Level 3 trigger is written out.

#### 4.1.4. Trigger Menu and Trigger Rates

For the event selection 128 trigger conditions are defined on Level 1. These triggers are combined with different Level 2 triggers and filters on Level 3. The configuration including all triggers used for data acquisition is called trigger list or trigger menu. In principle the number of triggers is only limited by the CPU power on Level 3. All data accepted by Level 3 are passed to the so-called Collector/Router and then distributed to the relevant subsystems. The data used for data analysis e.g. are passed to the data-logger. All of this raw data is copied to hard-drives and stored to magnetic tapes later. The data are partially passed to the data-distributor in parallel, which allows the online monitoring of the detector.

It is a challenging task to get a newly developed trigger into the trigger menu. In addition to a certification process for each trigger including the code stability verification, the trigger rates at all three trigger levels have to be taken into account. As some Level 3 triggers have the same requirements at Level 1 and Level 2 this is not a trivial task. Additionally the trigger rates have a luminosity dependency. Therefore a trigger menu can include different prescales<sup>7</sup>,  $p_T$  thresholds or even triggers for certain luminosity ranges. Each time a new run starts during a store<sup>8</sup>, the trigger rates are checked. If they have dropped below a certain value (the trigger rates drops during a store, due to the decreasing luminosity), a new trigger menu is loaded. This results in an increase of the trigger rate and ensures the maximum allowed rate is stored to tape. Figure 4.7 shows the trigger rates for all trigger levels as a function of time.

## 4.2. Trigger Strategies for $B$ Physics and Trigger Studies

Compared to the CDF RunII detector, which allows a trigger rate of 40 kHz at Level 1 [73], the DØ trigger system has to discard more events at this stage and hence many possible candidates are not passed to more sophisticated methods at higher trigger levels. There are two properties which can be used to distinguish  $B$  physics signal events from the continuum. Due to the  $B$  lifetime the tracks from the decay products are displaced from the primary vertex. Assuming the background is from QCD processes the background tracks should all be compatible with the primary vertex. Another possibility to reject uninteresting events and thus, to reduce the trigger rate is the usage of invariant mass requirements of the decay products.

As already mentioned, at DØ the only reasonable triggers for hadronic  $B$  decays at Level 1 and Level 2 are single muon triggers to trigger on the muon on the opposite side. The big advantage of the CDF RunII trigger system is the possibility to trigger on displaced vertices at the second trigger level (seeded by a two-track trigger on Level 1), which allows to collect large samples of hadronic events. Not until the third trigger level it is possible to use this type of trigger at DØ.

### 4.2.1. Level 1 Trigger Studies

In the course of upgrading the detector for RunIIb the Level 1 muon trigger underwent minor upgrades, e.g. the number of programmable  $p_T$  thresholds was raised from four to six. This is very important as it allows to define triggers with low  $p_T$  thresholds for runs with low luminosity, while higher  $p_T$  thresholds provide enough reduction at higher luminosities and keeping enough flexibility in between the high instantaneous luminosity at the beginning of a store and the low luminosities shortly before the beam is dumped at the end of a store. Two options were considered for RunIIb to keep the trigger rates low:

- Raising the muon quality requirement: Depending on the number of hits in the three muon layers, a muon candidate is categorized as loose, medium or tight muon. An exact definition about the requirements is given in Appendix A.1. In RunIIa mostly loose muons were required on Level 1. Hence, raising the quality requirement from loose to medium would reject many events for RunIIb, which were accepted for RunIIa.

---

<sup>7</sup>This technique randomly selects each  $n$ -th event, depending on the prescale factor  $n$ .

<sup>8</sup>The span of time between injecting the beams into the collider and dumping the beam, when the instantaneous luminosity has decreased under a certain level is called store.

Data Sample	#events	Muon Quality		Muon Cut	
		loose→tight		$p_T : (5 \rightarrow 5.7) \text{ GeV}/c$	
		Efficiency	Rejection	Efficiency	Rejection
$D_s(\phi\pi)\mu$	22k	98.6%	12.8%	81.6%	32.6%
$D_s e$	1.8k	97.1%	12.8%	84.3%	32.6%
$J/\Psi \rightarrow \mu\mu$	3k	96.3%	12.8%	69.9%	32.6%

**Table 4.1:** Overview of the signal efficiency for different gold-plated event samples for changing the muon quality assignment from loose to tight and for raising the muon  $p_T$  threshold at Level 1. The  $J/\Psi$  sample was used as a control sample, as these decays are triggered by di-muon triggers.

- Raising the transverse momentum requirement: One of the most important single muon triggers in RunIIa had a  $p_T$  threshold of  $5 \text{ GeV}/c$ . Raising this threshold would also reduce the number of fake events.

A third option, which can be used at Level 1 but is avoided as much as possible, is prescaling. This method is non-selective, as it does not rely on any physics input, but it randomly discards events and decreases the rate to a wanted limit. Of course a higher rejection of muon candidates influences the signal efficiencies also. In the context of this thesis trigger studies for the RunIIb upgrade were performed and both options were considered and compared. The results are shown in Table 4.1. Three different gold-plated data samples were taken into account: a signal sample of semimuonic  $B_s$  decays,  $B_s$  decays with an electron (which are triggered by the opposite side muon) and  $J/\Psi \rightarrow \mu\mu$  decays as a cross-check, as these decays should usually be selected by a di-muon trigger. For all three samples the efficiency was determined by comparing the number of events which pass the RunIIa trigger requirement with the requirements considered for RunIIb. The number obtained has to be compared to the rejection rate. It turned out that raising the muon quality keeps a signal efficiency between 96% and 99%, by reducing the background by 12.8%. Although raising the transverse momentum threshold results in a higher rejection of fake muons ( $\approx 33\%$ ), this option was dropped, as it also cuts away a significant amount of signal events (18%-30%).

#### 4.2.2. Level 2 Trigger Studies

For the RunIIb upgrade trigger studies were also performed for the second trigger level. On this trigger level more sophisticated methods are possible as trigger requirement. The following solutions were considered:

- Raising the transverse momentum requirement: This option is similar to the one described above in the Level 1 trigger studies section. However, Level 2 has the information of the CTT and the STT available. Contrary to RunIIa, where the STT information was used only, it was considered to use the CTT information, if the determination fails for the STT.
- Raising the track fit requirement: The Level 2 muon trigger allows to trigger on track parameters, as the fit quality  $\chi^2$ . For this solution the same option of utilizing the CTT information is possible, like just described.
- Raising the muon quality: This is the same principle as described above for Level 1. However, the exact requirements on hits in the muon layers are different, as shown in Appendix A.2.

Figure 4.8 shows the results for the first two solution approaches. The left-hand side shows the number of events passing the trigger requirement as a function of the transverse momentum threshold. The red line indicates the number of events in the gold-plated sample. The blue curve represents the status for RunIIa, where the information of the STT was considered only. The green distribu-

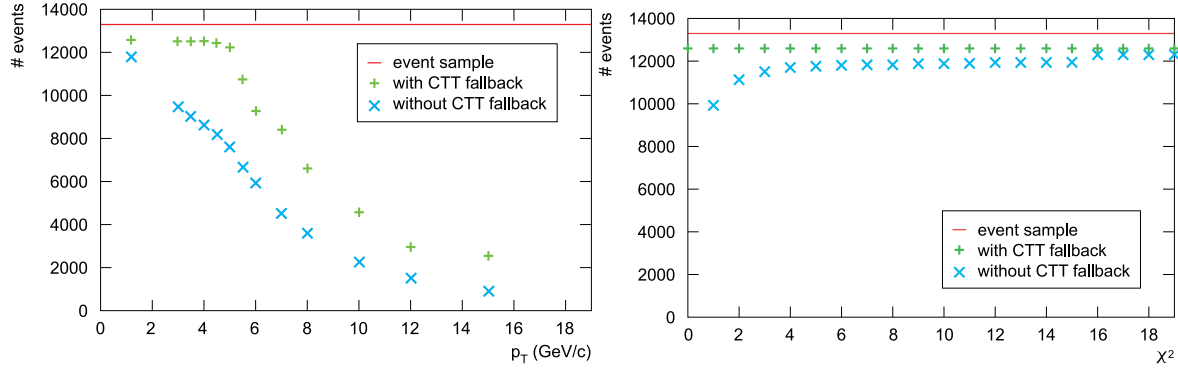


**Figure 4.8:** Comparison between gold-plated event sample (red), the solution with CTT fallback (green) and without CTT fallback (blue). The latter case corresponds to the setup as used in RunIIa. CTT fallback in this context means, that the tracking information of the CTT is used, if the SMT fails to fit the track. Left: Shown is the number of events passing the trigger requirement as a function of the transverse momentum threshold. Right: The number of events passing the trigger requirements as a function of  $\chi^2$  is shown at a fixed value of  $p_T = 1.2$  GeV/c.

Data Sample	#events	Muon Quality loose→tight	
		Efficiency	Rejection
$D_s(\phi\pi)\mu$	22k	92.7%	6.6%
$D_s e$	1.8k	97.1%	6.6%
$J/\Psi \rightarrow \mu\mu$	3k	94.9%	6.6%

**Table 4.2:** Overview of the signal efficiency for different gold-plated event samples for changing the muon quality assignment from loose to tight at Level 2.

tion is obtained using the CTT fit, if the STT fails. As it can be seen, the green curve is closer to the original number of events, which means the efficiency is higher. The rejection rate and thus, the background reduction rate at a value of  $p_T = 5.5$  GeV/c were determined as 64%, while the efficiency loss is about 30%. The right-hand side plot shows the same studies for a  $\chi^2$  at a fixed value of  $p_T = 1.2$  GeV/c. In this case both curves have a high efficiency and the CTT fallback solution shows hardly any impact on the efficiency. As it is shown in Table 4.2 the background rejection rate for raising the muon quality turned out to be the same as the loss in efficiency ( $\approx 7\%$ ). This behavior is similar to prescaling on Level 1, but prescaling on Level 1 is easier to implement and much more flexible. Hence, this option was dropped.

#### 4.2.3. Level 3 Trigger Studies

The same sample with semimuonic  $B_s$  decays as for the Level 1 trigger studies was analyzed to determine, which trigger was called and which trigger decision was fulfilled in the end. Mostly  $B_s$  decays are triggered by single muon triggers. This can be seen in Table 4.3. The most important triggers in this context are:

- ML1\_TMM3\_VX: Requires a primary vertex with  $|z| < 35$  cm, and at least one track matched muon with  $p_T > 3$  GeV/c.
- ML1\_TMM4\_VX: Requires a primary vertex with  $|z| < 35$  cm, and at least one track matched muon with  $p_T > 4$  GeV/c.

Trigger name	called	fired
ML1_TMM5_VX	16850	10203
ML1_TMM4_VX	8132	6195
MM1_TMM_IMP_2IPV	20686	5200
MUJ2_JT20_TK10	14031	5106
MM1_IPTMM5_IMP_V	20686	4688
MUJ1_JT25_LM3	13995	4492
ML1_TMM_2IP_IMP_V	19539	4223
ML1_IPTMM_IMP_V	19539	4150
MM1_JT25	20158	4110
ML1_TMM3_VX	4380	3894
MUJ1_2JT12_LMB_V	13995	3817
MM1_TMM_IMP_3IPV	20686	3808

**Table 4.3:** A gold-plated  $B_s \rightarrow D_s^- \mu$  sample was studied. This is a list of the trigger names, which were called the most by the Level 2 framework and which trigger requirements were actually fulfilled (fired).

- ML1\_TMM5\_VX: Requires a primary vertex with  $|z| < 35$  cm, and at least one track matched muon with  $p_T > 5$  GeV/c.
- ML1\_IPTMM\_IMP\_V: Requires 2 tracks with  $p_T > 0.5$  GeV/c, of opposite sign, that give an invariant mass commensurate with the  $\phi$  particle, and a primary vertex with  $|z| < 35$  cm, and at least one track matched medium muon with  $p_T > 4$  GeV/c and with an IP significance  $> 3.0$ .
- ML1\_TMM\_2IP\_IMP\_V: Requires 2 with tracks  $p_T > 0.5$  GeV/c, of opposite sign, that give an invariant mass commensurate with the  $\phi$  particle, and a primary vertex with  $|z| < 35$  cm, and two tracks with  $p_T > 1.5$  GeV/c) with IP Sig.  $> 3$ , and at least one track matched muon with  $p_T > 4$  GeV/c.

However, one would assume, that the trigger with the least transverse momentum requirement records the most events. This is not the case, as single muon triggers with low transverse momentum cuts must have higher prescales. Level 3 allows more sophisticated methods to trigger events, as the complete detector information is available and physical objects like invariant masses could be determined. An impact parameter significance tool had been developed and used during the RunIIa period. The impact parameter significance will have a Gaussian distribution centered around zero and with a standard deviation of one, if a track is associated to the primary vertex. By requiring several tracks with an impact parameter significance above a certain threshold, background events can be rejected at trigger level. In combination with another tool, providing the invariant mass of two objects and having a mass window around the  $\phi$  mass, it is possible to record hadronic  $B_s$  decays very efficiently. This is indicated by the the triggers ML1\_IPTMM\_IMP\_V and ML1\_TMM\_2IP\_IMP\_V, which require a certain invariant mass and impact parameter significance of the tracks. To determine the efficiencies of the impact parameter triggers, the information of a comparable single muon trigger was used and the additional requirements were added offline. By dividing one distribution by the other, the efficiency of the Level 3 online code can be checked.

Figure 4.9 shows the turn-on curves for the impact parameter trigger. Comparing RunIIa (left) and RunIIb (right) data, the lower efficiency is clearly visible. This behavior is easy explainable: The RunIIb data in this plot shows an integrated luminosity of  $\int \mathcal{L} dt = 0.4 \text{ fb}^{-1}$  only. As these data were taken directly after the upgrade, the machine and detector were not fully optimized. Additionally, the whole tracking code had to be re-written for RunIIb for the inclusion of Layer0. The overall efficiency of the impact parameter triggers is shown in Table 4.4. As it can be seen, the first two triggers, which require two tracks, have the best efficiency for semimuonic decays. Contrary to the

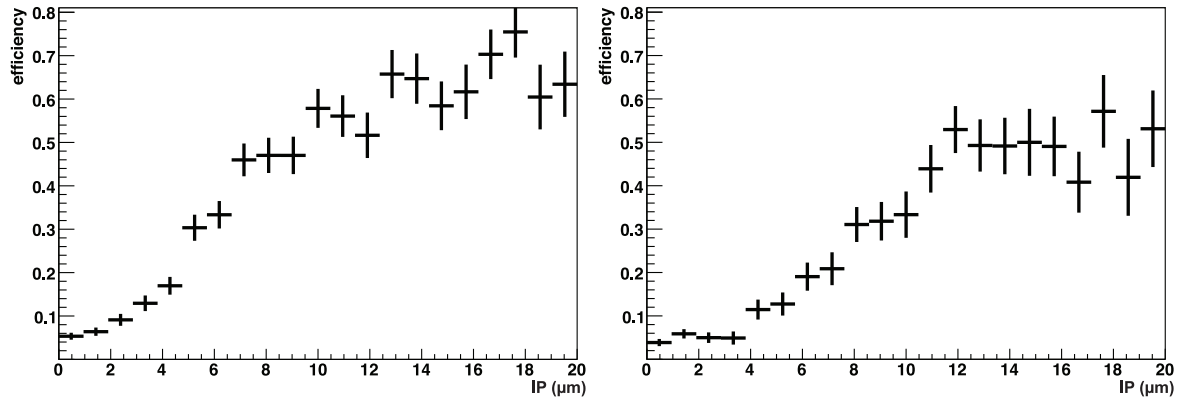


**Figure 4.9:** The results of the Level 3 impact parameter trigger studies are shown (Left: RunIIa with  $\int \mathcal{L} dt = 1.3 \text{ fb}^{-1}$ , Right: RunIIb with  $\int \mathcal{L} dt = 0.4 \text{ fb}^{-1}$ ). The lower efficiency for RunIIb is clearly observable. However, this is an early subset of the RunIIb data, where the machine and detector was not fully optimized. Additionally, the whole tracking code had to be re-written for RunIIb for the inclusion of Layer0.

Trigger name	efficiency	short description
ML1_IPTMM_IMP_V/1	0.67	see text
ML1_TMM_2IP_IMP_V/1	0.68	see text
ML1_TMM_3IP_IMP_V/1	0.50	3 tracks $p_T > 0.75 \text{ GeV}/c$
ML1_TMM_4IP_IMP_V/1	0.25	4 tracks $p_T > 0.5 \text{ GeV}/c$

**Table 4.4:** Efficiencies of relevant impact parameter triggers for a gold-plated event sample. The exact requirements of the first two triggers are explained in the text. The difference of the third and the last trigger in this table, compared to the second trigger, is the number of required tracks with a certain minimum transverse momentum.

single muon triggers their rate allows an unprescaled operation for all luminosity ranges. However, it turned out that the requirement of this trigger became obsolete, as the muon quality on Level 1 was raised anyway and therefore the trigger rate was low enough to even reduce the pre-scale factor on the low  $p_T$  single muon triggers.



## Reconstruction and Monte Carlo Simulation

All data delivered by the DØ data acquisition is stored in a raw data file format on tapes. A software is required to run algorithms on the raw data to identify particles and their tracks by combining the output of all sub-components of the detector and store it as DST<sup>1</sup> [74] or TMB<sup>2</sup>. To study physics processes it is required to compare this information with Monte Carlo simulations, which include all current knowledge about the physics and detector response. This chapter deals with the software used to preprocess the raw data in order to use it for analyses (Section 5.1) and with physics simulations (Section 5.4) to better understand the signal composition. It will conclude with a description of the dataset used for this analysis in Section 5.6.

### 5.1. Reconstruction Software

In order to run physics analysis on raw data from the DØ detector, physics objects, such as tracks, muons, and jets, have to be reconstructed. The standard DØ software for this task is provided by the DØ algorithms group and is called d0reco [75]. Further steps include vertex and cluster finding, which is done using a software package called BANA [76].

#### 5.1.1. d0reco

The offline reconstruction of raw data at DØ is performed with the program d0reco. It reconstructs the objects needed for physics analysis and requires a large amount of CPU power. It is capable of running on both – data and Monte Carlo. The executable is supposed to run on the offline production farms and the results are stored in a common place, accessible by all DØ physicists. As the *B*-physics group uses their own data format called AADST, an extra step is necessary to benefit from the centrally stored reprocessed data.

---

<sup>1</sup>Data Summary Tape

<sup>2</sup>Thumbnail: In contrast to the DST only a compressed subsample of variables per event is stored in order to keep the filesize per event low.

The data is organized in the form of chunks. The primary input for d0reco is the raw data chunk, which is created either by the Level 3 trigger system or Monte Carlo simulations. The reconstruction program adds another chunk for each type of reconstructed object. The data processing is done in several steps. At first detector specific information is unpacked and electronic channels are assigned to physical detector components and calibration constants are applied. Geometry constants are used to associate detector elements with physical positions in space and clusters or hit objects are reconstructed. Afterwards the hit information of the silicon microstrip tracker and central fiber tracker is analyzed to reconstruct global tracks. The results of these algorithms are used as input for the vertexing (see also Section 5.2). The primary vertex, which indicates the location of the  $p\bar{p}$  collision is searched for and different kinematical quantities are calculated. Secondary vertices are identified and assigned to long-lived particles like  $B$  mesons. This information is stored in the vertex chunk and then used for particle identification. Using a wide variety of sophisticated algorithms, information from each of the preceding reconstruction steps are combined and standard physics object candidates are created. At first objects like electrons, photons, muons, neutrinos (through missing  $E_T$ <sup>3</sup>) and jet candidates are identified. Afterwards candidates for heavy-quark and tau decays are built, by using all previous results. A more detailed description can be found in [75].

### 5.1.2. BANA and AATrack

The standard software package used by the  $B$ -physics group for post-processing of d0reco output is called BANA and was inspired by the software used for many years by the DELPHI detector at LEP for  $B$ -physics analyses. Primary vertex finding is done, as well as track jet clustering using the Durham algorithm and secondary vertex finding. The package provides an interface to access Monte Carlo truth information, flavor tagging and silicon  $dE/dx$  information, which makes it very efficient. Its code is based on the DØ AATrack package used for track reconstruction in d0reco.

## 5.2. Track and Vertex Reconstruction

The mode of operation of the AA tracking algorithm is to build all kind of track hypotheses from each possible combination of the first three hits in the silicon microstrip tracker and central fiber tracker. For each hypothesis the radius of curvature  $R$ , the impact parameter  $b$  and the angle  $\varphi$  between the intersection point of the first three hits are calculated. These parameters are illustrated in Figure 5.1. Only tracks, with  $b < b_{\max} = 5$  cm,  $R > R_{\min} = 30$  cm and  $\varphi < \varphi_{\max} = 0.2$  rad are accepted.

Afterwards all hits along a helix within a fixed  $\Delta\phi$  window of the outer layer of the tracking system are assigned to the hypothetical track. If no hit is found a miss pattern is returned. After all hypothesis are generated, they are arranged by number of individual hits, multiple assigned hits and misses. The most probable track hypothesis is selected and all hits, assigned to this track are not taken into account for the other hypothesis. This procedure is repeated for all remaining track hypothesis.

In the final stage the track object is reconstructed with a Kalman filter [77] by taking the magnetic field, multiple scattering and energy loss of a particle within the detector into account. The obtained track can be approximated by a helix. Figure 5.2 shows a particle trajectory and its projections to the  $x$ - $y$  and  $r$ - $z$  plane with the five parameters:

<sup>3</sup>Missing  $E_T$ : Neutrinos can not be detected directly. The energy balance of an event is determined. The difference between the total energy in the detector and the energy of the identified particles is called missing energy and assigned to the neutrinos.

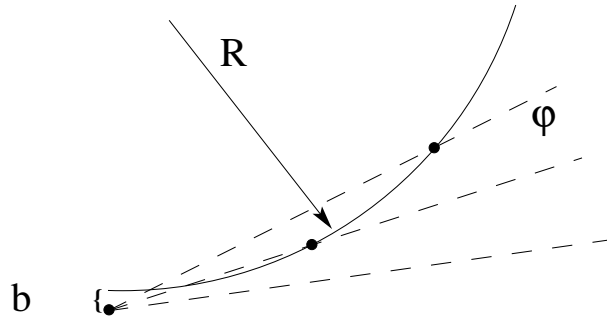


**Figure 5.1:** Functional principle of the track hypothesis of the AA tracking algorithm. Shown are three hits with the corresponding three track parameters radius of curvature  $R$ , the impact parameter  $b$  and the angle  $\varphi$ .

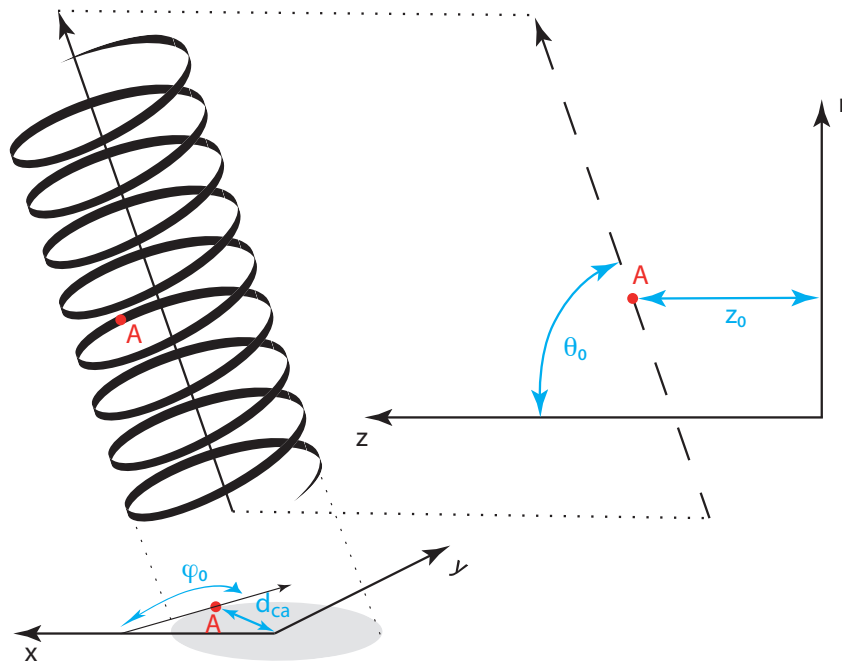


**Figure 5.2:** Particle track projection into  $x$ - $y$  and  $r$ - $z$  plane with the five helix parameters distance of closest approach  $d_{ca}$ , distance  $z_0$ , azimuth angle  $\varphi_0$ , polar angle  $\theta_0$  and charge and track curvature  $q\kappa$ .

- Distance of closest approach ( $d_{ca}$ ): shortest distance of trajectory to point of origin in the  $x$ - $y$  plane.
- Distance  $z_0$ : longitudinal component of impact parameter vector (distance of  $A$  to  $r$ -axis).
- Azimuth angle  $\varphi_0$ : angle between tangent of track and  $x$ -axis.
- Polar angle  $\theta_0$ : angle between  $z$ -axis and particle trajectory.
- Charge and track curvature  $q\kappa$ .

These five helix parameters are saved for each track object and the primary vertex is determined from reconstructed tracks and the beamspot position. The exact position of the primary vertex is calculated by minimizing the  $\chi^2$  of the function

$$\chi^2(\vec{V}) = \sum_a \sum_{\alpha, \beta=1,2} b_a^\alpha (S_a^{-1})_{\alpha, \beta} b_\beta^a + \sum_i \frac{(V_i^{sp} - V_i)^2}{(\sigma_i^{sp})^2}, \quad (5.1)$$

where  $b_{1,2}^a$  are the components of the two-dimensional impact parameter determined relative to the coordinate origin, and  $S_a$  is the covariance matrix of the 2D impact parameter measurement. The beamspot position is given by  $V_i^{sp}$  with uncertainty  $\sigma_i^{sp}$ .

The  $\chi^2$  function is minimized with the tear down method. One of the tracks is removed and the difference

$$\Delta\chi^2 = \chi^2(N_{tr}) - \chi^2(N_{tr} - 1) \quad (5.2)$$

is calculated. The track is removed, if the difference  $\Delta\chi^2$  is above a certain threshold. All secondary vertices are calculated through the same method without taking the beamspot position into account.

Recently a procedure to assign more correctly the impact parameter uncertainties has been developed and applied to all data [78]. In general the tracking resolution for data, especially for the impact parameter is underestimated. For this purpose a track wise calibration has been performed and applied afterwards without refitting the tracks. To obtain this scale factor the tracks are divided into categories based on the number of silicon hits, the layers of silicon in which the first and second hit occurred and the cluster width of the first hit. For these classes of tracks detailed studies for the impact parameter resolution were done and the tracking errors are scaled accordingly.

### 5.3. Muon Reconstruction

The large muon system of the DØ detector allows to reconstruct and measure muon tracks without information from the tracking system. A straight particle track is assigned to hits in the *BC*-layer of the muon system (Section 3.2.3), allowing a measurement of the direction of flight and the position perpendicular to the wires of the drift chambers. This is possible, as both layers reside outside the magnetic field of the toroid magnet and therefore no force affects the trajectory. To measure the position parallel to the drift chamber wires precisely, the tracks are assigned to hits in the *A*-layer, which provides a finer granularity through matching the wire hits with hits in the scintillators. Of course the bending through the magnetic field between *A*-layer and *BC*-layer has to be taken into account. All this information is used to built local muon tracks and the results are stored for each event.

If it is possible to assign information from the tracking system to a local muon track, these tracks are stored as global muon tracks. The accuracy of global tracks exceed the measurement of local muon tracks, as the limited lever arm of each system separately is extended by combining their measurements. Depending on the hit matching of the sub-detectors different muon qualities are assigned. The variable corresponding to this criterion is called *nseg*. Table 5.1 shows these quality assignments. It is also possible to identify muons in the calorimeter by tracking energy deposits consistent with the passage of a minimum ionizing particle. Due to limited accuracy, these tracks are not used in this analysis.

### 5.4. Monte Carlo Simulation

One of the keys for a reliable analysis is to study the expectations using Monte Carlo simulations. For the hadronic modes these simulations were used to determine selection efficiencies and *k*-factor distributions. At DØ the software package d0runjob [79] is used to produce the Monte Carlo

Muon Type	nseg
local muon track	-3
hit in BC-layer only	-2
hit in A-layer only	-1
central track + calorimeter track	0
central track + hit in A-layer only	1
central track + hit in BC-layer only	2
central track + local muon track	3

**Table 5.1:** Overview of muon qualities. Depending on certain hit patterns, a quality between -3 and 3 is assigned.

samples. It requires an input file specifying parameters like decay channel, number of events to produce etc. An example of an input file to produce the decay  $B_s \rightarrow \pi D_s(\phi\pi)X$  can be found in Section B.1. It has up to five different sections, which are called in sequential order:

- The `Global` section contains book keeping information for the storage manager to gain easy access to the generated events once they are produced.
- Afterwards the `Generated` section is called. The generators ALPGEN [80] and PYHTIA [81] are available. All the events for this analysis are generated with PYTHIA, a common tool for simulating  $e^+e^-$ ,  $pp$  and  $p\bar{p}$  collisions. Depending on the requirements, the main production process, decay-trees, collision energy etc. need to be specified. For every event it starts simulating the interactions during a  $p\bar{p}$  collision. The following steps are simulated in sequential order during the generator step
  - a hard scattering process,
  - initial state radiation,
  - final state radiation,
  - hadronization,
  - particle decays.

All of these steps are configured through the so-called card-file. The decay itself is controlled through the user-decay-file, which controls EvtGen [82]. Some of the following steps are very CPU intensive, hence the `d0mess` file (an example can be found in Appendix B.2) tells the generator, which events should be saved for further processing and which can be discarded immediately, by applying kinematic cuts. The configuration is done by the so-called `d0mess` file.

- A virtual copy of the DØ detector has been built with the software package DØgstar [83]. It uses the libraries of GEANT3 [84], which have been developed at CERN to simulate the interaction of particles with the detector material. This includes dead material like the calorimeter cryostat as well as the active material of the calorimeter or the scintillating fibers of the tracking system. Also the interaction with the magnetic field is taken into account. This step requires the most computing time. As there are different geometry files for the RunIIa and RunIIb detector, the `Simulated` section includes, which configuration should be used.
- Afterwards the generated events are overlayed with a zero-bias<sup>4</sup> sample, a calorimeter pile-up<sup>5</sup> and noise from the calorimeter and the tracking system is added. The configuration is done in the `Digitized` section and calls the `d0sim` [85] program.

<sup>4</sup>Zero-bias events are recorded without any triggers adding a bias to the recorded sample. They are used to simulate detector noise and overlayed events.

<sup>5</sup>In the calorimeter system the pile-up, which means the overlap of additional background events on the signal events, originates from two different sources. At high luminosity more than one collision can happen at one crossing (physics pileup) and additionally the readout electronics may contain signals originating from the previous and subsequent crossings (electronics pile-up).

channel	$\mathcal{B}$ ( $10^{-3}$ )	p17			p20		
		MC request ID	gen. evts.	sel. evts.	MC request ID	gen. evts.	sel. evts.
$B_d \rightarrow D^* \pi$	2.7	32987 32986	26918087	214750	89542	25067987	200250
$B_d \rightarrow D^* \pi \pi \pi$	7.7	32983	166210795	104000	89551	160521728	100250
$B_d \rightarrow D^* a1$	13.0	32982	18674524	101000	9552	18508469	100500
$B_d \rightarrow D^* e$	56.0	33877	19377885	102750	89547	19845201	105000
$B_d \rightarrow D^* K$	0.61	32985	24654940	104750	89548	23561611	100250
$B_d \rightarrow D^* \pi \pi^0$	7.0	32981	20881042	102250	89549	21332743	104250
$B_d \rightarrow D^* \rho$	6.8	32980	16212846	103250	89546	15766653	100250
$B_d \rightarrow D^* \tau$	16.0	33878	134456712	103750	89545	136016502	104500
$B_d \rightarrow D^{*0} \pi$	0.9	32984	59376006	100500	89550	61441060	103250
$B^+ \rightarrow D^* \pi \pi$	4.2	33879	12112095	99750	89543	12580554	103750
$B^+ \rightarrow D^* \pi \pi \pi^0$	30.0	33880	13585537	101750	89544	13451892	100250

**Table 5.2:** Overview on the generated Monte Carlo samples to study  $B_d$  decays. For each decay channel the branching ratio, the number of events, generated by PYTHIA and the number of events passing the d0mess cuts is given for p17 (to simulate RunIIa data) and p20 (to simulate RunIIb data) Monte Carlo.

channel	$\mathcal{B}$ ( $10^{-3}$ )	p17			p20		
		MCrequest ID	gen. evts.	sel. evts.	MC request ID	gen. evts.	sel. evts.
$B_s \rightarrow D_s \pi$	2.7	32600 32602	3355725544	228887	89532	70394624	205000
$B_s \rightarrow D_s \pi \pi \pi$	17.1	33119	39097805	100000	89540	40316784	102750
$B_s \rightarrow D_s a1$	8.5	33117	38455116	103250	89533	38705294	104500
$B_s \rightarrow D_s e$	7.0	34195	62906938	104250	89534	63238229	104500
$B_s \rightarrow D_s K$	0.9	33118	156337998	102500	89539	156302476	102250
$B_s \rightarrow D_s \rho$	7.3	33121	35883223	83077	89541	43405476	100500
$B_s \rightarrow D_s^* a1$	12.2	33122	40336715	103250	89535	41160952	105000
$B_s \rightarrow D_s^* e$	84.0	34247	58813433	101000	89536	58571854	100500
$B_s \rightarrow D_s^* \pi \pi \pi$	17.1	34106	38365742	100000	89537	40412927	105000
$B_s \rightarrow D_s^* \pi$	2.6	33120	37052347	102750	89538	38117826	104500

**Table 5.3:** Overview on the generated Monte Carlo samples to study  $B_s$  decays. For each decay channel the branching ratio, the number of events, generated by PYTHIA and the number of events passing the d0mess cuts is given for p17 (to simulate RunIIa data) and p20 (to simulate RunIIb data) Monte Carlo.

- Finally d0reco is called in the Reconstructed section, just like it is done for real data. This way the same data structure is achieved and it is possible to handle the Monte Carlo files the same way like data.

## 5.5. Monte Carlo Samples

To study the selection of hadronic  $B_d$  and  $B_s$  decays it is essential to produce a large amount of Monte Carlo samples. Furthermore, the Monte Carlo samples are used for background studies and to determine parameters for the mixing frequency studies. Table 5.2 shows the produced decay channels for hadronic  $B_d$  decays (including two  $B^+$  decays to study the background), while the same information for hadronic  $B_s$  decays is given in Table 5.3. The decay channel, its branching ratio, the number of events, generated by PYTHIA and the number of events passing the d0mess cuts is given. In these tables p17 refers to Monte Carlo samples for RunIIa, while p20 are the appropriate Monte Carlo samples for RunIIb. This differentiation is necessary, as for the generation of the p20 Monte Carlo samples the upgrade of the DØ detector for RunIIb has been taken into account.

	RunIIa - p14		RunIIa - p17		RunIIb	
	# events	Efficiency	# events	Efficiency	# events	Efficiency
total	115374534	100%	1195580564	100%	1265459598	100%
single- $\mu$	23673711	20.5%	573746529	48.0%	632653338	50.0%

**Table 5.4:** Collected events and number of events passing the single muon skim requirements. This includes a short period in the beginning of RunIIa, which is referred as p14, the rest of RunIIa, which is known as p17 and RunIIb data.

## 5.6. Dataset

The data sample used for this analysis is the single  $\mu$  skim, also used for the semileptonic  $B_s$  selection [54] (and for mostly all single muon analysis in the B-physics group). It is described in detail in [86]. All muons in this skim have to fulfill the following requirements:

- At least one hit in either A-layer, BC-layer (i.e. one hit in either of the two layers) or all three layers of the muon system plus match with with a track from the central tracking system.
- A transverse momentum higher than 1.5 GeV/c ( $p_T \geq 1.5$  GeV/c).
- Best matched muon (centralrank = 1).
- Fit of local muon track was successful ( $\chi^2 \geq 0$ ).
- At least two hits in the SMT ( $n_{\text{SMT}} \geq 2$ ).
- At least two hits in the CFT ( $n_{\text{CFT}} \geq 2$ ).

The data used here was collected between April 2002 and Spring 2006 (RunIIa) – corresponding to about  $1.3 \text{ fb}^{-1}$  – and from July 2006 until August 2007 (RunIIb), which equals to approximately  $1.5 \text{ fb}^{-1}$  (see Figure 3.2 for a plot, showing the accumulated data). Table 5.4 shows an overview on the total number of collected events and how many events pass the single muon skim requirements. While a lot of the muons in RunIIa were triggered with the criteria explained above, the RunIIb trigger condition was changed from loose to tight. That means, hits are required in A-layer and BC-layer and not in either of the layers, as described above. Hence, the total number of collected events is lower for RunIIb than for RunIIa, comparing the same integrated luminosity. But as the trigger requirements already select particles, which are more likely a muon, the yield of the single muon skim is higher for RunIIb than for RunIIa.





## Signal Selection

$B_d$  and  $B_s$  mesons have similar hadronic decay modes. However, more  $B_d$  than  $B_s$  mesons are produced in  $p\bar{p}$  collisions and thus, it is easier to develop tools and techniques with the  $B_d$  channel. The main goal of both selections is to identify signal candidates with high efficiency and low background. This chapter is divided into two parts. At first the selection of the hadronic decay mode<sup>1</sup>  $B_s \rightarrow \pi D_s(\phi\pi)X$  in a dataset of  $\int \mathcal{L} dt = 2.8 \text{ fb}^{-1}$  is presented (Section 6.1). The second part of this Chapter (Section 6.2) is about the selection of the hadronic  $B_d$  decay mode<sup>1</sup>  $B_d \rightarrow D^{*-}\pi^+$  in the same amount of data. As this channel is discussed in detail in [87] and [88], only a brief overview is given on this channel.

### 6.1. Selection of Hadronic $B_s$ Decays

Due to the low number of expected events in the dataset (Section 2.1), the selection of the decay mode  $B_s \rightarrow \pi D_s(\phi\pi)X$  (Figure 2.1) is very challenging. To avoid processing the whole dataset several times during the optimization of the selection, which takes about three weeks each time, a preselection with loose cuts (Section 6.1.1) is applied to the single muon skim at first (the requirements of this skim are described in detail in Section 5.6). It requires the BANA package for the signal reconstruction (Section 5.1.2) and uses the special data format AADST of this package. The output of this step are ROOT-trees [89], allowing to do all further processing on any computer with the ROOT software installed, instead of relying on the complete DØ framework. To enrich the sample with signal candidates, these cuts are tightened in the final selection (Section 6.1.2). This step requires only several hours of computing time. Thus, it allows to quickly adapt cuts.

#### 6.1.1. Selection Principle and Preselection

The selection is made candidate wise. A candidate is defined by a muon and a  $B_s$  meson. Generally one event can have several signal candidates. First, all tracks in a single event are clustered into jets using the DURHAM [90] clustering algorithm. In this analysis, a maximum distance  $d_{\text{init}} =$

<sup>1</sup>For the signal selection also the charge conjugated states are taken into account. This applies for all further occurrences of this decay.

0.25 GeV/ $c$  (the distances are converted into dimensions corresponding approximately to the transverse momentum) was allowed in PYCLUS when forming starting clusters, to speed up reconstruction. The maximum distance  $d_{\text{join}}$ , below which it is allowed to join two clusters was set to  $d_{\text{join}} = 15.0 \text{ GeV}/c$ . Additionally, when the value changed by less than 0.0001 between two iterations the process was stopped. A more detailed view on these parameters is given in [91]. Muons with a track-match are selected. Four additional tracks associated with the  $K^+$ ,  $K^-$  and the two pions have to come from the same vertex. To enrich the data sample with signal candidates, cuts are applied to the tracks. Not all available distributions of relevant cut variables, indicating the proper cut value are shown in the following, but only some representatives. A mechanism to access the preselection at four different stage is implemented and the selection steps are called TAG, LOOSE, STANDARD and TIGHT. This procedure gives an amount of events with at least one  $B_s$  meson candidate after preselection. The following paragraphs include some words on the selection principle and a summary of the cuts, made for each particle candidate. To each of these cuts an identifier (A.1–H.3) is assigned. The exact cut values for each identifier for the TAG, LOOSE, STANDARD and TIGHT selections are shown in Table 6.1.

### Muon Selection

In addition to the selection criteria used in the single muon selection (see Section 5.6) tighter cuts have been applied to the muon transverse momentum and to the total muon momentum. There is no special trigger requirement. However, almost all events were recorded through single muon triggers. Only 7 (2) events of RunIIa (RunIIb) data were not selected by single muon triggers, which amounts to 4.3% (1.7%) of the total number of events passing the final selection. The name of the trigger, which selected most of the events in RunIIa, is ML1\_TMM5\_VX<sup>2</sup>. In the final selection, 20 events were selected by this trigger. In RunIIb most of the events were selected by the trigger ML3\_TMM4\_VX<sup>3</sup>. In the sample of the final selection, 52 events were selected by this trigger. By requiring a certain number of hits in the CFT and SMT it is ensured to use well reconstructed muons for the further analysis only. This is supported by a cut on the muon quality variable  $nseg$  (Section 5.3) and a cut on the transverse and total momentum.

- A.1: At least two hits in the SMT.
- A.2: At least two hits in the CFT.
- A.3: The muon quality  $nseg$  is required to be greater than 2 ( $nseg \geq 2$ ).
- A.4: A transverse momentum greater than 2 GeV/ $c$  ( $p_T \geq 2 \text{ GeV}/c$ ).
- A.5: A total momentum greater than 3 GeV/ $c$  ( $p_{\text{tot}} \geq 3 \text{ GeV}/c$ ).
- A.6: Consistent with the  $z$ -position of the primary vertex.

### $\phi$ Selection

Two tracks are assumed to be kaons coming from a  $\phi$  meson decay. Each track combination is taken into account, as long as both tracks are charged oppositely. For each track the transverse compo-

<sup>2</sup>The exact description of this trigger, as found in the trigger database [92]: L1: A region=w (wide muon region) single muon trigger with tight scintillator and loose wire requirements plus a track with  $p_T > 3 \text{ GeV}/c$  and NOT Calorimeter unsuppressed readout. L2: pass events with at least one muon found meeting STANDARD quality(=2) and tight scintillator timing requirements but no  $p_T$  or region requirement. L3: Requires a primary vertex with  $|z| < 35 \text{ cm}$ , and at least one track matched muon with  $p_T > 5 \text{ GeV}/c$ .

<sup>3</sup>The exact description of this trigger, as found in the trigger database [92]: L1: Select events with one muon passing medium quality requirements and tight scintillation timing cuts, matched to a track found by the CTT with  $p_T > 3 \text{ GeV}/c$ . L2: Select events with one muon passing tight quality requirements and tight scintillation timing cuts and one track found by the CTT or the STT with  $p_T > 3.3 \text{ GeV}/c$  (but no  $\chi^2$  cut). L3: Requires a primary vertex with  $|z| < 35 \text{ cm}$ , and at least one track matched muon (M) with  $p_T > 4 \text{ GeV}/c$ .

ment  $b_T$ , the longitudinal component  $b_L$  and their uncertainties  $\sigma_T$  and  $\sigma_L$  of the impact parameter vector are determined. The significance of the impact parameter  $b/\sigma_b = \sqrt{(b_T/\sigma_T)^2 + (b_L/\sigma_L)^2}$  is calculated. Tracks with a small significance are associated to the primary vertex and thus, the background from tracks produced in the fragmentation process can be minimized by requiring a certain significance of the impact parameter. Afterwards the kaon mass is assigned to the two tracks and the invariant mass  $m(KK)$  of the two tracks is reconstructed. Figure 6.1 shows the transverse momentum distributions of both kaons and the invariant  $KK$  mass for both run periods.

- B.1: At least two hits in the SMT for each kaon.
- B.2: At least two hits in the CFT for each kaon.
- B.3: Each Kaon must have a transverse momentum greater than 0.5 GeV/c ( $p_T \geq 0.5$ ).
- B.4: Both Kaons must belong to the same jet.
- B.5: A certain impact parameter significance  $b/\sigma_b$  of at least one kaon track.
- B.6: Both Kaons are required to be associated to the primary vertex.
- C.1: Kaons charged oppositely
- C.2: Consistent with a certain invariant  $KK$  mass range.

### $D_s^-$ Selection

To reconstruct a  $D_s^-$  meson an additional track assumed to be a pion is added to the two kaon system. Each event contains a high number of tracks, resulting in a high combinatorial background. Contrary to real  $D_s^-$  candidates, these randomly selected track combinations have a small transverse momentum. Hence, a loose cut on the transverse momentum keeps the signal candidate yield high, while suppressing much combinatorial background. A certain impact parameter significance is required for the  $\pi$  meson, as already described for the kaons. A  $\chi^2$ -fit using the tracking parameters is done to reconstruct the four momentum and the decay vertex of the  $D_s^-$  meson. The fitted mass  $m(KK\pi)$  of the  $D_s^-$  meson candidate has to be consistent within a certain mass range around the world-average. To reduce combinatorial background and  $D_s^-$  mesons coming from prompt charm production, a cut on the flight length significance  $l_{xy}/\sigma(l_{xy})$  is applied. The angle, in the  $x$ - $y$  plane, between the  $D_s^-$  meson momentum vector and the vector of the primary vertex to the decay vertex is required to be small. The  $\phi$  meson is a spin one particle. Thus, the kaons are produced mostly along the direction of the  $\phi$  meson. To reduce the background there is a helicity<sup>4</sup> cut. Figure 6.2 shows the transverse momentum distribution of the selected pion candidate, as well as the transverse momentum of the  $D_s^-$  meson. The invariant  $KK\pi$  mass is shown without any likelihood selection cut applied. Additionally the helicity variable  $c_{xy}$  is shown.

- D.1:  $\pi$  meson has at least two hits in the SMT.
- D.2:  $\pi$  meson has at least two hits in the CFT.
- D.3: A certain minimum transverse momentum.
- D.4: Must belong to the same jet like the first selected kaon.
- D.5: Oppositely charged than the first selected kaon.
- D.6: A certain impact parameter significance  $b/\sigma_b$ .
- D.7: Consistent with the  $z$ -position of the primary vertex.
- E.1: Consistent with a certain invariant  $KK\pi$  mass range.
- E.2:  $\chi^2$  of the secondary vertex fit to be smaller than a certain value.
- E.3: A cut on the flight length significance  $l_{xy}/\sigma(l_{xy})$  is applied.

<sup>4</sup>The helicity is defined as the angle between the  $D_s^-$  meson and the  $K^+$  meson in the  $(K^+, K^-)$  rest frame

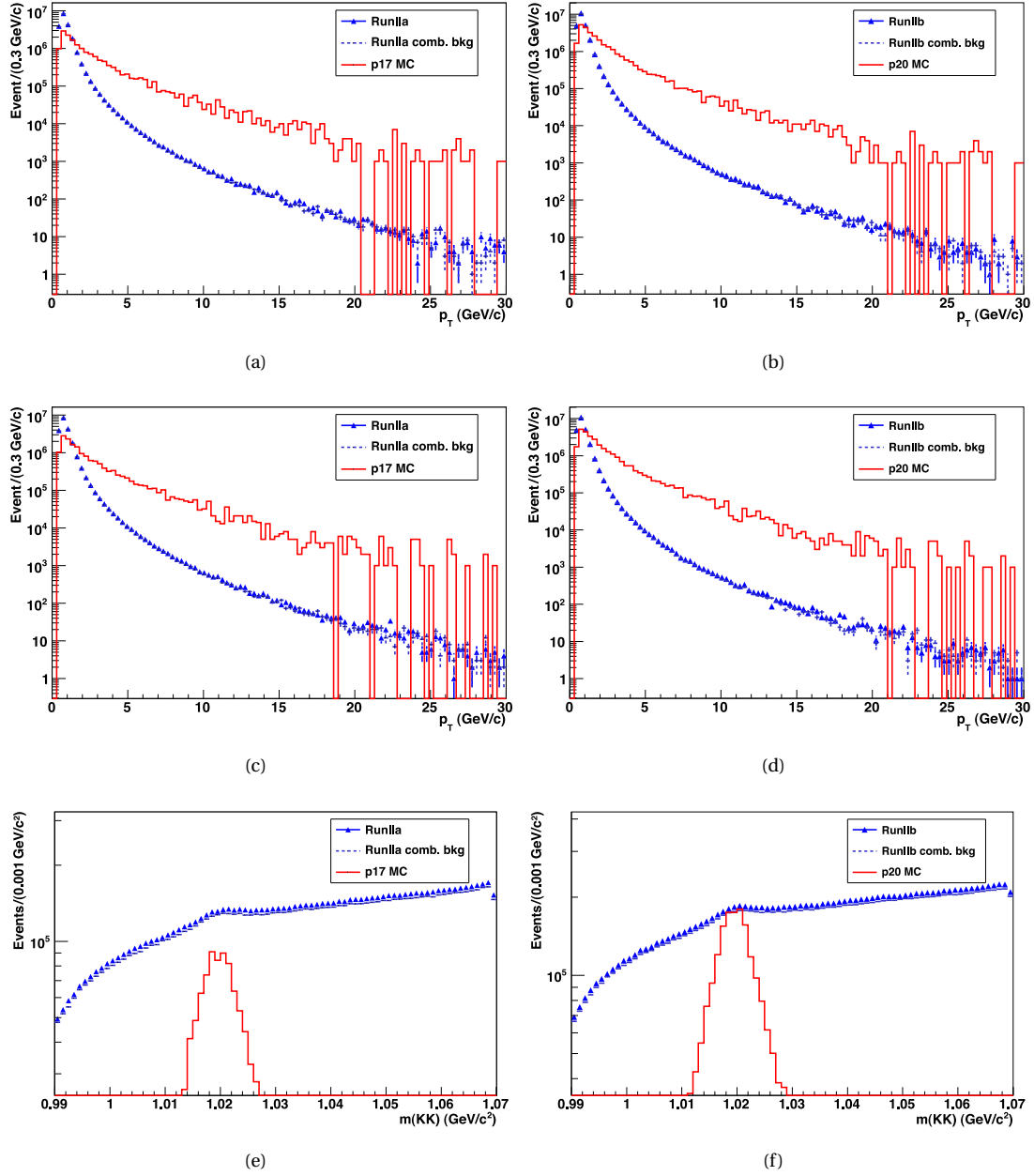


**Figure 6.1:** Distributions for the  $\phi$  candidate selection. All plots show a comparison between data, combinatorial background and an arbitrary scaled signal Monte Carlo (this includes the fully reconstructable mode only). (a) RunIIa transverse momentum distribution of the first selected kaon candidate. (b) Same as (a), but for RunIIb data. (c) RunIIa transverse momentum distribution of the second selected kaon candidate. (d) Same as (c), but for RunIIb data. (e) RunIIa invariant KK mass distribution. (f) Same as (e), but for RunIIb data.

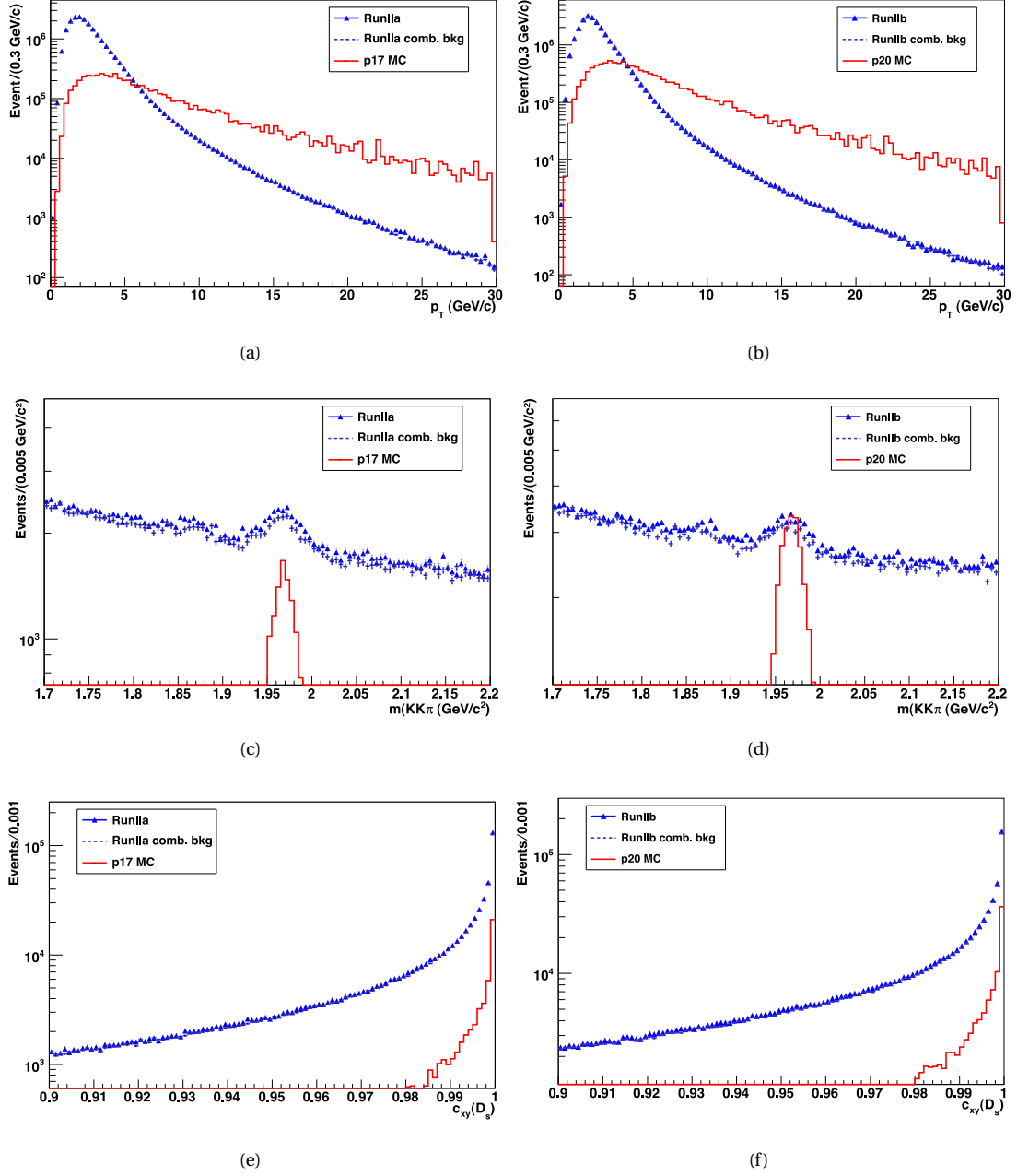


**Figure 6.2:** Distributions of the  $D_s^-$  candidate selection. All plots show a comparison between data, combinatorial background and an arbitrary scaled signal Monte Carlo (this includes the fully reconstructable mode only). (a) RunIIa distribution of the  $D_s$  transverse momentum. (b) Same as (a), but for RunIIb data. (c) RunIIa invariant  $KK\pi$  mass distribution without likelihood selection cut applied. (d) Same as (c), but for RunIIb data. (e) RunIIa helicity angle  $c_{xy}$  distribution. (f) Same as (e), but for RunIIb data.

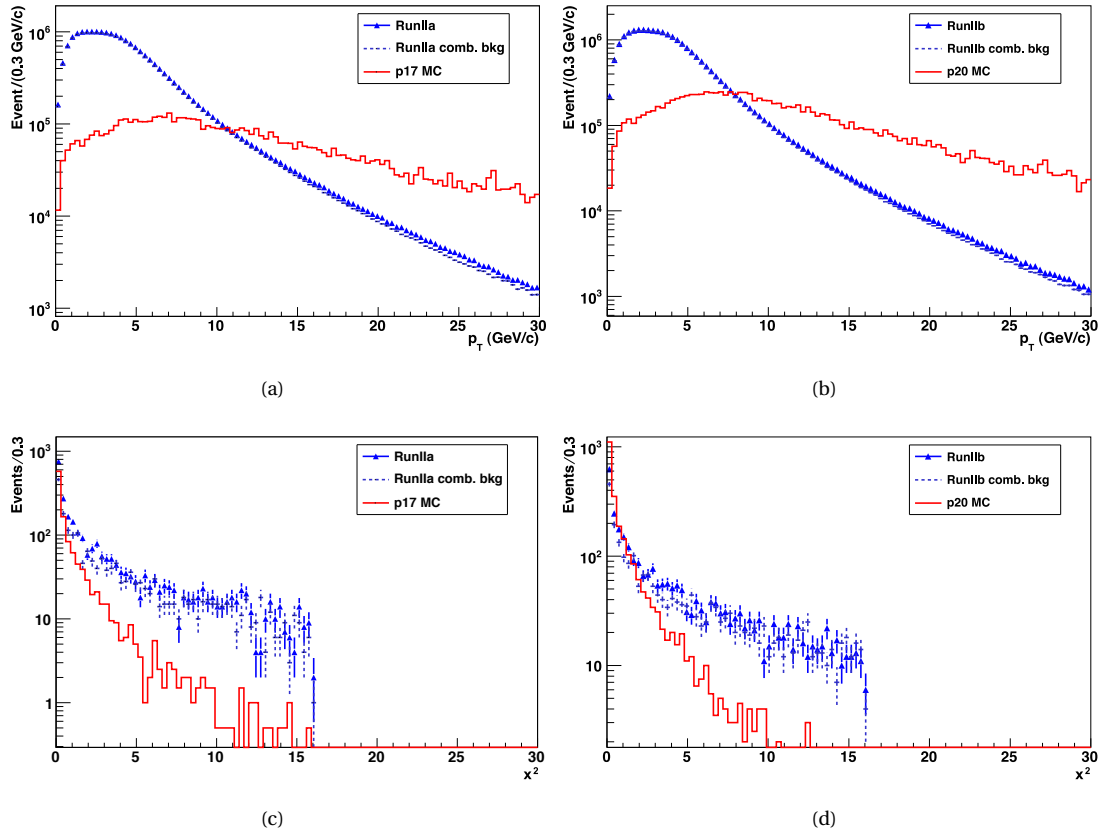


**Figure 6.3:** Distributions for the  $B_s$  candidate selection. All plots show a comparison between data, combinatorial background and signal an arbitrary scaled signal Monte Carlo (this includes the fully reconstructable mode only). (a) RunIIa transverse momentum distribution of the  $B_s$  candidate, (b) RunIIb transverse momentum distribution of the  $B_s$  candidate, (c) RunIIa distribution of the  $B_s$  vertex fit variable, (d) RunIIb distribution of the  $B_s$  vertex fit variable.

- E.4: A certain value of the combined likelihood selection variable  $\text{ctag}$ . The determination of this multivariate discriminating variable is described in Section 6.1.2.
- E.5: There is a cut on the helicity angle, which is defined as the angle between the  $D_s^-$  and the  $K^+$  meson in the  $(K^+, K^-)$  rest frame. The cosine of this angle is required to be greater than 0.15 ( $\cos \alpha_{\text{hel}} > 0.15$ ).
- E.6: The direction of the  $D_s^-$  momentum vector and the line from the primary vertex to the decay vertex has to be consistent in the  $xy$ -plane ( $\cos_{xy}(D_s^-) > 0.9$ ).

### $B_s$ Selection

Finally, to reconstruct a  $B_s$  meson an additional track is searched for and assumed as a pion. A cut on the transverse momentum is applied in order to reduce the combinatorial background which mostly consists of low momentum pions. Additionally this cut makes the final state kinematically similar to those in the semileptonic channels [54], [93]. A certain impact parameter significance is required for the  $\pi$  meson, as already described for the kaons. To form the  $B_s$  meson, the fitted  $D_s^-$  meson candidate is combined with the additional pion. A kinematic fit is applied to reconstruct the

four momentum and the decay vertex of the  $B_s$  meson. Furthermore, the isolation

$$\text{Isolation} = \frac{p_{\text{tot}}(\pi D_s)}{p_{\text{tot}}(\pi D_s) + \sum_i p_{\text{tot},i}} \quad (6.1)$$

is determined, where  $\sum_i p_{\text{tot},i}$  is the sum of the total momentum of all not selected tracks within the cone  $\sqrt{(\Delta\phi)^2 + (\Delta\eta)^2}$ . This variable is large for  $b$  hadrons. The fitted mass  $x(KK\pi\pi)$  is required to be in a mass window consistent with the world-average, which is wide enough to take also partially reconstructed events into account. To remove pathological track combinations, the candidate is removed if the decay length of the  $B_s$  meson is larger than the decay length of the  $D_s^-$  meson.

- E.1:  $\pi$  meson has at least two hits in the SMT.
- E.2:  $\pi$  meson has at least two hits in the CFT.
- E.3: A certain minimum transverse momentum requirement of the  $\pi$  meson.
- E.4: Must belong to the same jet as the first selected kaon.
- E.5: A certain impact parameter significance  $b/\sigma_b$ .
- E.6: Consistent with the  $z$ -position of the primary vertex.
- G.1: Consistent with a certain Invariant  $KK\pi\pi$  mass range.
- G.2:  $\chi^2$  of the primary vertex fit to be smaller than certain value.
- G.3: A positive flight length of the  $B_s$  meson ( $l_{xy}(B_s) > 0$ )
- G.4: A cut on the flight length significance  $l_{xy}/\sigma(l_{xy})$  is applied.
- G.5: The cosine of the angle between the direction of the  $B_s$  and the line between the primary vertex and the  $B_s$  decay vertex is required to be smaller than 0.95.
- G.6: Not in a muon jet.
- G.7: Isolation  $> 0.6$ .
- G.8: No muon in a certain cone around the  $B_s$  candidate.

### General Selection

These cuts are not related to a certain track of the signal selection, but are used to suppress the background further. All of these selections are part of the BANA package.

- H.1: No additional muons in the same jet.
- H.2: No  $J/\Psi$  in the same jet (a detailed view on this selection can be found in [94]).
- H.3: No  $D^*$  background (this selection is described in detail in [95] and [96]).

#### 6.1.2. Final Selection

Based on the list of candidates from the preselection further cuts are made in the final selection. This includes tightening already existing preselection cuts as well as new kinematic cuts. Additionally a likelihood selection is applied. All candidates are divided into two samples, depending on the sign of the product of the charge of the  $D_s^-$  meson and the additional pion<sup>5</sup>: the pion coming from the  $D_s^-$  meson decay has to be of opposite charge than the pion from the  $B_s$  meson decay. This defines signal candidates. It is not possible to generate Monte Carlo sample for all occurring background sources with the appropriate statistic. Thus, another way had to be found to study the background shape. As most of the occurs from wrong-sign combinations of the pions, the combinatorial background was estimated using a sample with pions of the same charge.

<sup>5</sup>Opposite charges result in a negative product as expected for the signal, same charges result in a positive product and are used for the combinatorial background

particle	cut value	ID	TAG	LOOSE	STD	TIGHT
Muon	$n_{\text{SMT}} \geq 2$	A.1	✓	✓	✓	✓
	$n_{\text{CFT}} \geq 2$	A.2	✓	✓	✓	✓
	$n_{\text{seg}}=2$	A.3	✓	✓	✓	✓
	$p_T > 2$ (GeV/c)	A.4	✓	✓	✓	✓
	$p_{\text{tot}} > 3$ (GeV/c)	A.5	✓	✓	✓	✓
	PV	A.6	✓	✓	✓	✓
$K^+, K^-$	$n_{\text{SMT}} \geq 2$	B.1	✓	✓	✓	✓
	$n_{\text{CFT}} \geq 2$	B.2	✓	✓	✓	✓
	$p_T > 0.5$ (GeV/c)	B.3	✓	✓	✓	✓
	$\text{jet}(K^+) = \text{jet}(K^-)$	B.4	✓	✓	✓	✓
	$ b/\sigma_b $	B.5			$\geq 4$	$\geq 4$
	PV	B.6	✓	✓	✓	✓
$\phi$	$q(K^+) \cdot q(K^-) < 0$	C.1	✓	✓	✓	✓
	$m(K^+ K^-)$ (GeV/c <sup>2</sup> )	C.2	$< 1.07$	$< 1.07$	[1.014;1.026]	[1.014;1.026]
$\pi(D_s^-)$	$n_{\text{SMT}} \geq 2$	D.1	✓	✓	✓	✓
	$n_{\text{CFT}} \geq 2$	D.2	✓	✓	✓	✓
	$p_T$ (GeV/c)	D.3	$\geq 0.3$	$\geq 0.5$	$\geq 0.5$	$\geq 0.5$
	$\text{jet}(\pi) = \text{jet}(K^+)$	D.4	✓	✓	✓	✓
	$q(\pi) \cdot q(K^-) < 0$	D.5	✓	✓	✓	✓
	$ b/\sigma_b $	D.6			$\leq 4$	$\leq 4$
	PV	D.7	✓	✓	✓	✓
$D_s^-$	$m(K^+ K^- \pi)$ (GeV/c <sup>2</sup> )	E.1	[1.7;2.3]	[1.7;2.3]	[1.7;2.3]	[1.925;2.005]
	$\chi^2$	E.2	$\leq 25$	$\leq 25$	$\leq 16$	$\leq 16$
	$ l_{xy}/\sigma(l_{xy}) $	E.3		$\geq 3$	$\geq 3$	$\geq 3$
	ctag	E.4			$\geq -0.8$	$\geq -0.8$
	$\cos(\text{hel})$	E.5		$\geq 0.15$	$\geq 0.15$	$\geq 0.15$
	$\cos_{xy}(D_s^-)$	E.6	$\geq 0.9$	$\geq 0.9$	$\geq 0.9$	$\geq 0.9$
$\pi(B_s)$	$n_{\text{SMT}} \geq 2$	F.1	✓	✓	✓	✓
	$n_{\text{CFT}} \geq 2$	F.2	✓	✓	✓	✓
	$p_T$ (GeV/c)	F.3	$\geq 1.5$	$\geq 1.5$	$\geq 1.5$	$\geq 2.5$
	$\text{jet}(\pi) \neq \text{jet}(K^+)$	F.4	✓	✓	✓	✓
	$ b/\sigma_b $	F.5				$\geq 4$
	PV	F.6	✓	✓	✓	✓
$B_s$	$m(K^+ K^- \pi\pi)$ (GeV/c <sup>2</sup> )	G.1	[4.0;6.5]	[4.0;6.5]	[4.0;6.5]	[4.7;5.6]
	$\chi^2$	G.2	$\leq 16$	$\leq 16$	$\leq 16$	$\leq 9$
	$l_{xy}$	G.3				$\geq 0$
	$ l_{xy}/\sigma(l_{xy}) $	G.4		$\geq 4$	$\geq 4$	$\geq 4$
	$\cos_{xy}(B_s)$	G.5	$\leq 0.95$	$\leq 0.95$	$\leq 0.95$	$\leq 0.95$
	$B_s$ no in $\mu$ -jet	G.6			✓	✓
	Isolation	G.7			$\geq 0.6$	$\geq 0.6$
	No $\mu$ in cone around $B_s$	G.8			$\geq 0.7$	$\geq 0.7$
General	Not in a muon jet	H.1			✓	✓
	Not in a $J/\Psi$ jet	H.2			✓	✓
	No $D_s^*$ background	H.3		✓	✓	✓

**Table 6.1:** Preselection cuts  $B_s$ . The cuts are made from TAG to TIGHT, i.e. all cuts applied during the TAG selection are also applied for the LOOSE selection.



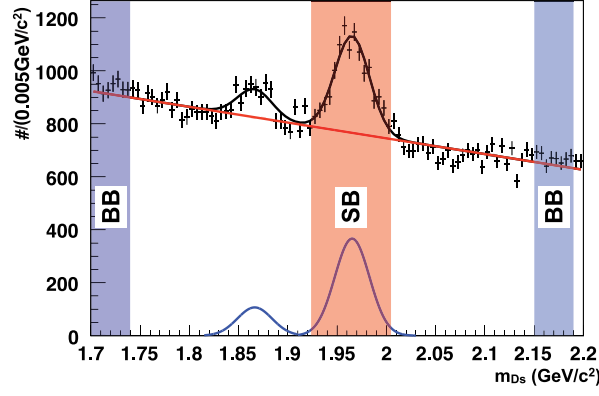


**Figure 6.4:** Definition of the signal and background regions for the likelihood selection optimization. A signal band (SB) in the region  $1.925 \text{ GeV}/c^2 < m(K^+ K^- \pi^-) < 2.005 \text{ GeV}/c^2$  and two background bands (BB) in the regions  $1.7 \text{ GeV}/c^2 < m(K^+ K^- \pi^-) < 1.74 \text{ GeV}/c^2$  and  $2.15 \text{ GeV}/c^2 < m(K^+ K^- \pi^-) < 2.19 \text{ GeV}/c^2$  are assigned.

### Vetoed Events

To pass the final selection, further conditions must be fulfilled. Events already accepted for the semileptonic decay channel  $B_s \rightarrow \mu \nu_\mu D_s(\phi\pi)$  are rejected. The selection of this channel is described in [54]. Furthermore there is a veto on events with a muon in the same  $k_T$  jet as the decay itself and no candidate may occur within a cone around the  $B_s$  meson of  $R=0.7$ .

### Likelihood

Because of the low  $S/(S+B)$  ratio a likelihood selection [97] is used to optimize the yield of  $D_s^-$  meson candidates. For a selection of input variables  $x_i$  the probability density function of the signal  $f^s(x_i)$  and the background  $f^b(x_i)$  is assigned. A combined variable  $y$  is built for each event

$$\text{ctag} = \prod_{i=1}^N \text{ctag}_i \quad \text{with} \quad \text{ctag}_i = \frac{f^s(x_i)}{f^b(x_i)}. \quad (6.2)$$

If a variable  $x_i$  is not defined for one event,  $\text{ctag}_i$  is set to one. The likelihood selection used for this analysis is optimized with RunIIb data. To obtain the likelihood function at first all cuts, except the  $B_s$  meson related cuts, are applied plus an additional cut on the transverse momentum of the  $\phi$  meson is applied to enrich the sample ( $p_T(K^+ K^-) > 2 \text{ GeV}/c$ ). Afterwards the invariant  $K^+ K^- \pi^-$  mass is plotted (Figure 6.4) and a signal band in the region  $1.925 \text{ GeV}/c^2 < m(K^+ K^- \pi^-) < 2.005 \text{ GeV}/c^2$  and two background bands in the regions  $1.7 \text{ GeV}/c^2 < m(K^+ K^- \pi^-) < 1.74 \text{ GeV}/c^2$  and  $2.15 \text{ GeV}/c^2 < m(K^+ K^- \pi^-) < 2.19 \text{ GeV}/c^2$  are defined. The background is fitted with a linear function, while the  $D_s^-$  meson signal peak is parametrized with a Gaussian. Both functions are integrated over the whole plot range to obtain numbers of background and signal candidates.

The set of variables, included into the likelihood selection and assumed to be independent of each other is defined by:

- absolute value of  $\cos(\phi)$ : the helicity angle as described above (Figure 6.5),
- the isolation variable as described above (Figure 6.6),
- $p_T(KK)$ : the sum of the transverse momentum of the two kaons forming the  $\phi$  (Figure 6.7),
- $\chi^2(D_s)$ : the  $\chi^2$  of the fit for the  $D_s^-$  (Figure 6.8),
- $m(KK)$ : the invariant mass of the  $\phi$  (Figure 6.9).

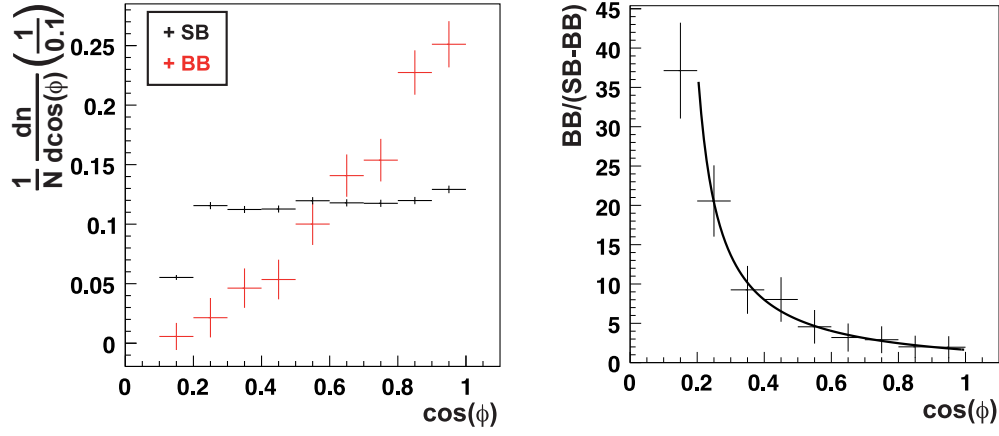


**Figure 6.5:** Distribution of the helicity angle variable. Left: Signal + background (SB) and background bands (BB) normalized to one. Right: The distribution of the ratio  $BB/(SB-BB)$ .

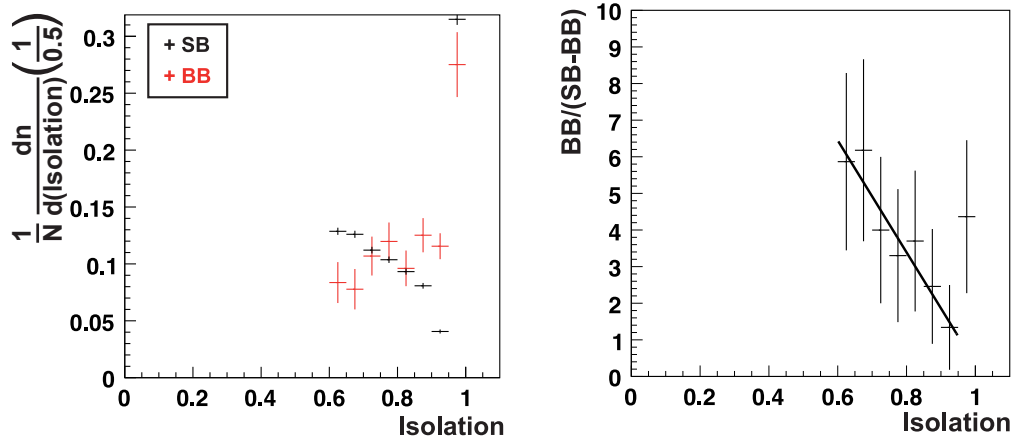


**Figure 6.6:** Distribution of the isolation variable. Left: Signal+background and background bands normalized to one. Right: The distribution of the ratio  $BB/(SB-BB)$ .

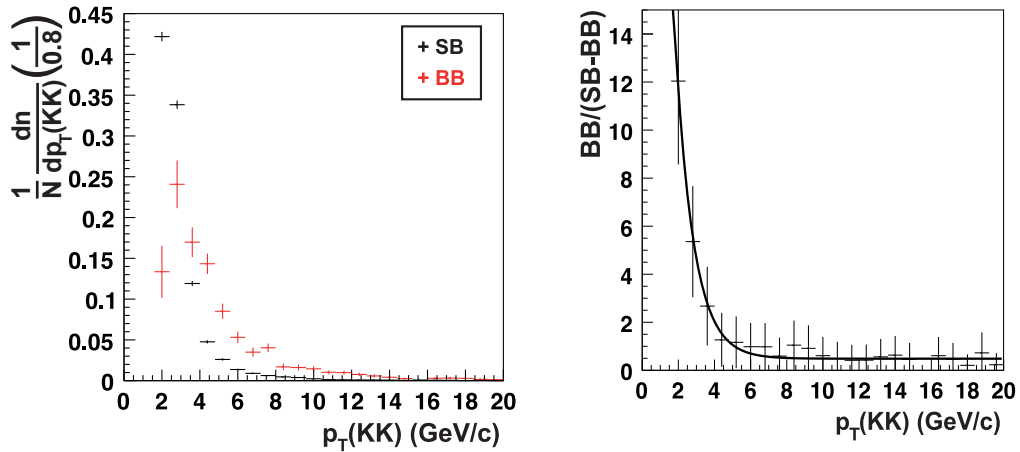


**Figure 6.7:** Distribution of the transverse momentum of the  $\phi$  candidate. Left: Signal+background and background bands normalized to one. Right: The distribution of the ratio  $BB/(SB-BB)$ .

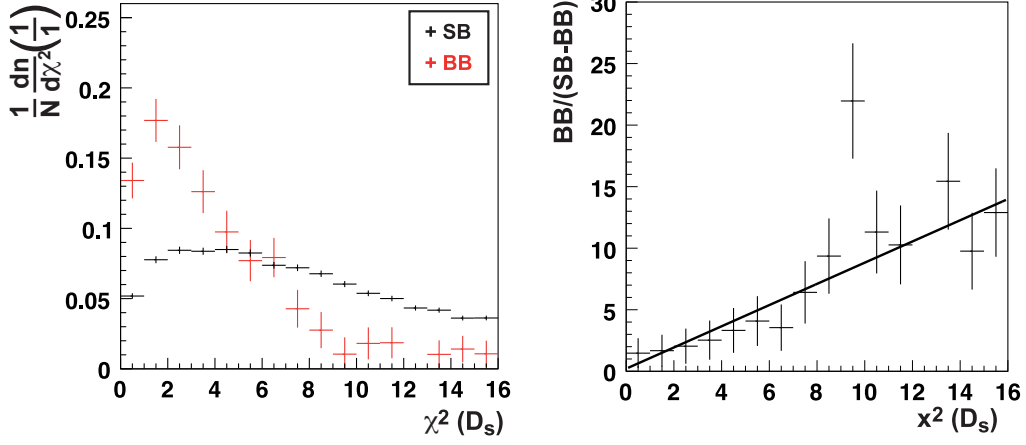


**Figure 6.8:** Distribution of the  $\chi^2$  of the fit for the  $D_s^-$ . Left: Signal+background and background bands normalized to one. Right: The distribution of the ratio  $BB/(SB-BB)$ .

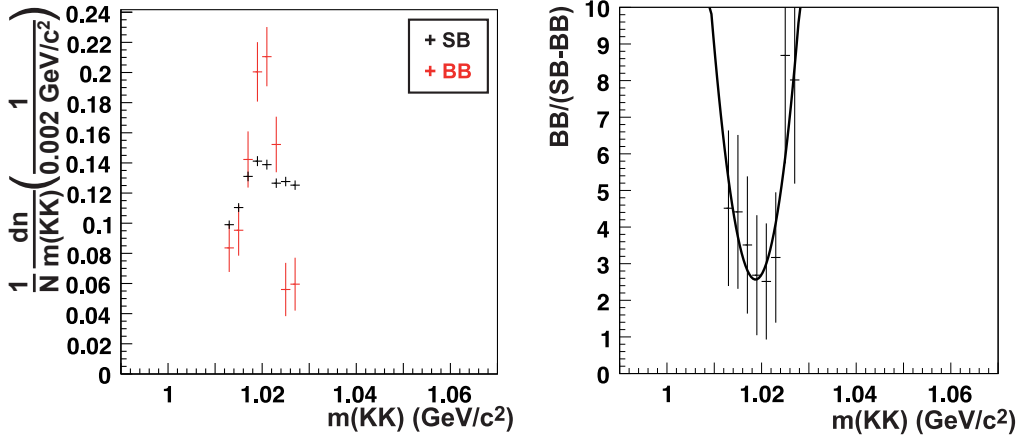


**Figure 6.9:** The invariant mass of the  $\phi$  meson. Left: Signal+background and background bands normalized to one. Right: The distribution of the ratio  $BB/(SB-BB)$ .

Reference distributions for each variable are plotted, scaling the events from the background bands with the number of background candidates and scaling the signal band with the number of signal candidates. As seen in the example signal distribution matches the background distribution in the sidebands and hence, provides a good modeling. The background is subtracted from the signal plus background shape and the background itself divided by this sum. The obtained distribution is parametrized with a polynomial of fourth order (right-hand side plots of Figures 6.5 - 6.9).

The combination of all input variables is computed and shown in Figure 6.10. Figure 6.11 and Figure 6.12 show the invariant  $\phi\pi$  mass distributions for RunIIa and RunIIb. In this plot, the black line is the total signal, consisting of background (red) and signal candidates (blue). The higher peak shows the distribution of a reconstructed  $D_s^-$  candidate with another pion with the correct charge to build a  $B_s$  meson. The other peak is a  $D_s^*$  reflection and derives from candidates with a wrong pion charge. The number of signal candidates is reduced in the further final selection by a hard cut ( $p_T \geq 3.0 \text{ GeV}/c$ ) on the transverse momentum on the pion from the  $B_s$  meson and a flight length cut on the  $B_s$  meson.

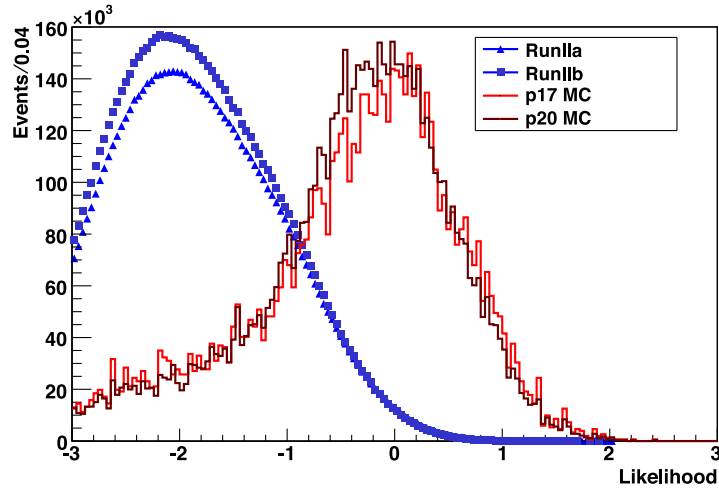


**Figure 6.10:** Likelihood distribution for RunIIa and RunIIb data as well as the corresponding p17 (RunIIa) and p20 (RunIIb) signal MC.

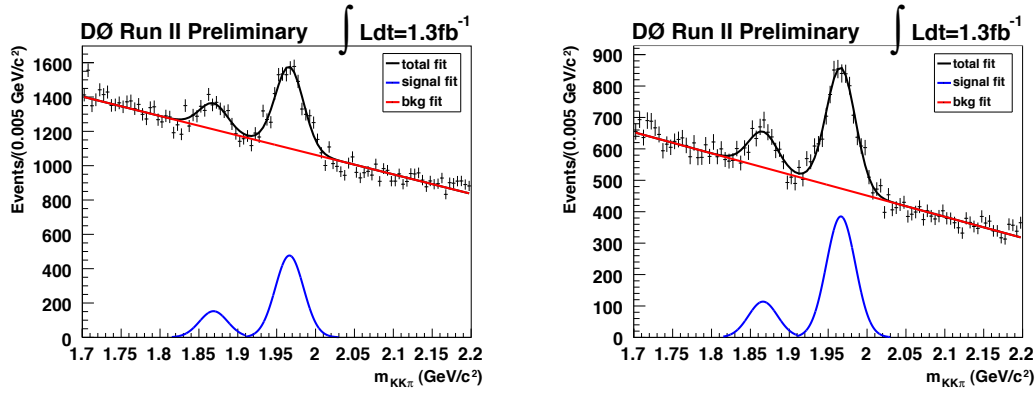


**Figure 6.11:** RunIIa, Left: No cut on the likelihood selection, Background: 17638 Candidates: 4209, Right: Combined likelihood selection variable has to be greater than -0.6, Background: 7597, Candidates: 3482, efficiency: 82.7%, background reduction: 70.2%.

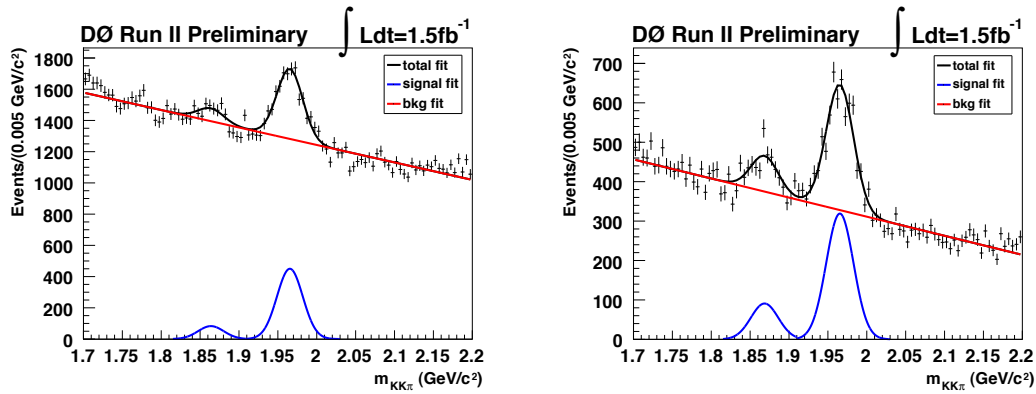


**Figure 6.12:** RunIIb, Left: No cut on the likelihood selection, Background: 20515 Candidates: 3681, Right: Combined likelihood selection variable has to be greater than -0.4, Background: 5250, Candidates: 2746, efficiency: 74.6%, background reduction: 74.6%.

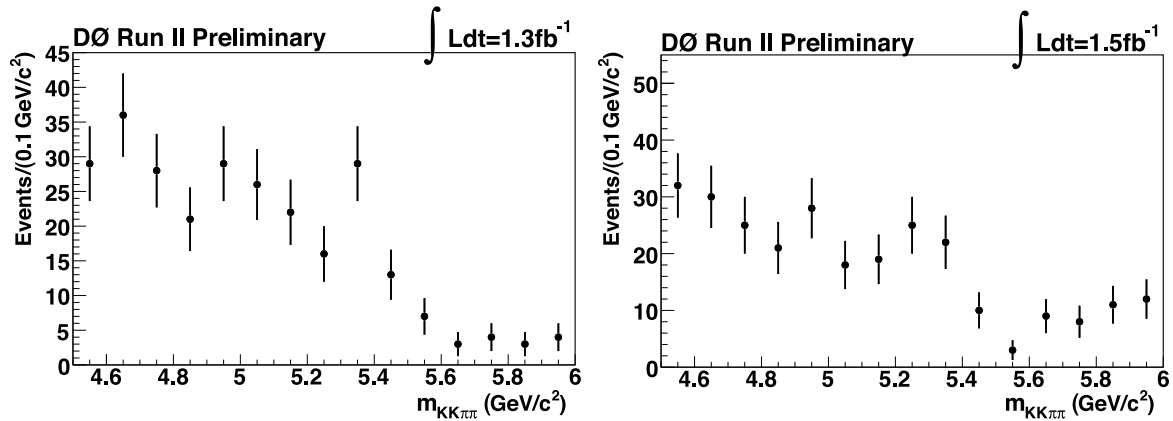


**Figure 6.13:** Plots of the invariant  $K^+ K^- \pi^+ \pi^-$  mass. Left: RunIIa data, Right: RunIIb data. Due to the limited  $p_T$  resolution of the  $D\bar{0}$  detector, the fully reconstructable decays are not separable from the partially reconstructed decays. Hence, no clearly visible  $B_s$  mass peak can be seen.

### Summary of Final Selection Cuts

Most of the cuts in the final selection tighten the cuts from the preselection:

- B.5:  $|b/\sigma_b| \geq 6$  for at least one kaon track.
- D.6: Impact parameter significance of the pion from the decaying  $D_s^-$   $|b/\sigma_b| \geq 8$ .
- E.5: As the likelihood selection is optimized for RunIIb data, there is a slightly tighter cut on RunIIa data: RunIIa:  $\text{ctag} > -0.4$ , RunIIb:  $\text{ctag} > -0.6$ .
- F.4: The cut on the transverse momentum of the  $\pi$  from the decaying  $B_s$  meson is tightened to  $p_T \geq 3.0 \text{ GeV}/c$ .
- F.5: Impact parameter significance of the pion from the decaying  $B_s$  meson  $|b/\sigma_b| \geq 6$ .
- G.1: The cut on the invariant  $KK\pi\pi$  mass is tightened to  $4.75 \text{ GeV}/c^2 \leq m(KK\pi\pi) \leq 5.5 \text{ GeV}/c^2$ .
- Exclude events with a non-reliable muon tag ( $\mathcal{D} < -1.5$ ).

Additionally two charge combinations are considered:

- Both pions charged oppositely ( $q(\pi(D_s^-)) \cdot q(\pi(B_s)) < 0$ ). This combination is used for the signal sample.
- Same charge combinations ( $q(\pi(D_s^-)) \cdot q(\pi(B_s)) > 0$ ). This combination is used for combinatorial background studies.

Figure 6.13 shows the reconstructed  $B_s$  meson mass. Due to the limited  $p_T$  resolution of the  $D\bar{0}$  detector, the fully reconstructable decays are not separable from the partially reconstructed decays. Hence, no clearly visible  $B_s$  mass peak can be seen. Extensive Monte Carlo studies were necessary to understand the signal composition. The samples, described in Section 5.5 were used to study the underlying partially reconstructed decays of the signal. Figure 6.14 shows the same  $B_s$  mass distribution, as shown in the previous figure, but with the signal composition. As it can be seen, the data matches the expected distribution of the Monte Carlo samples and the combinatorial background well for RunIIa. For RunIIb the data background deviates from the distribution of the combinatorial background. This is caused by a very limited statistic in the background fit, resulting in high uncertainties of the distribution obtained. This will improve by utilizing more data.

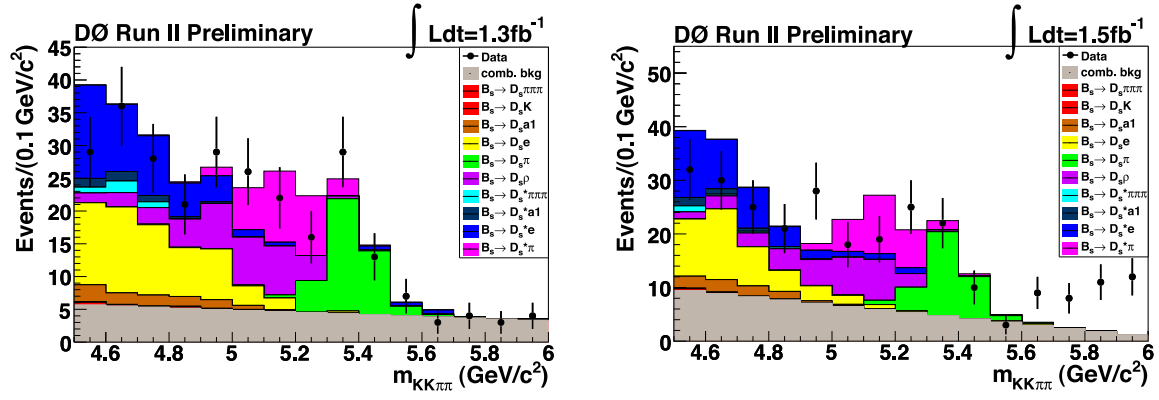


**Figure 6.14:** Plots of the invariant  $K^+ K^- \pi^+ \pi^-$  mass. Left: RunIIa data, Right: RunIIb data. Extensive Monte Carlo studies were necessary to understand the signal composition. The samples, described in Section 5.5 were used to study the underlying partially reconstructed decays of the signal.

	p14 data		RunIIa p17 data		p17 MC		RunIIb p20 data		p20 MC	
	# events	Yield	# events	Yield	# events	Yield	# events	Yield	# events	Yield
total	115374534	100%	1195580564	100%	227787	100%	1265459598	100%	205000	100%
single- $\mu$	23673711	20.5%	573746529	48.0%	68165	29.9%	632653338	50.0%	52647	25.7%
TAG	1160075	4.9%	24206358	4.2%	12460	18.3%	28928533	4.6%	13199	25.1%
LOOSE	653935	56.4%	13374115	55.3%	10512	84.7%	18148921	62.7%	11501	87.1%
STANDARD	10979	1.7%	200275	1.5%	4054	38.6%	242587	1.3%	4716	41.0%
TIGHT	307	2.8%	4242	2.1%	1735	42.8%	4753	0.2%	2002	42.5%
final	2	0.7%	160	3.8%	1597	92.0%	107	2.2%	1834	91.6%

**Table 6.2:** The number of candidates for data and the corresponding Monte Carlo is summarized. This includes a short period in the very beginning of RunIIa, referred as p14, the rest of RunIIa, which is named p17 and RunIIb (p20). The yields are given as relative values to the previous selection stage. Due to the multiplicity of tracks the combinatorial background is higher for RunIIb, leading to a slightly lower candidate yield. It starts with the total number of events collected on tape. Afterwards selection cuts are applied to select events with one muon. The further steps include the cuts as described in this chapter for the different preselection steps TAG, LOOSE, STANDARD and TIGHT and the final selection.

### 6.1.3. Performance of Selection

The selection is divided into different qualities of the signal sample. Beginning with a single- $\mu$  skim (Section 5.6) loose cuts are applied for a so-called TAG selection. By tightening the cuts and adding further constraints, the purity of the signal sample gets enhanced within the chain: TAG→LOOSE→STANDARD→TIGHT, as it can be seen from the number of events in Table 6.2. All events of the TIGHT selection are equal to the events from the final selection and used for this analysis and go into the Log-likelihood fit. The efficiencies are determined relative to the previous selection.

	signal sample	wrong charge combination
RunIIa	162	34
RunIIb	107	31
Total	269	65

**Table 6.3:** Events passing the final selection.

Table 6.3 shows an overview of the events passing the final selection for RunIIa and RunIIb data. The yield in RunIIb is lower than for RunIIa: it is dropping with increasing luminosity, because of multiple interactions present at high luminosities [98]. For the background events: the more  $p\bar{p}$  interactions in an event, the more confusion is expected.

## 6.2. Selection of Hadronic $B_d$ Decays

As this channel is discussed in detail in [87] and [88], only a brief overview is given here on this channel. The intention for this selection was, to stick as closely as possible to the selection of the hadronic  $B_s$  mode in order to verify the selection methods. The  $B_d$  mesons are reconstructed via the  $D^{*-}\pi^+$  decay mode, where the  $\pi^+$  is denoted as  $\pi(B_d)$ . To reconstruct  $D^{*-}$  mesons, the decay mode  $\bar{D}^0\pi^-$  is used. ( $\pi^-$  are denoted as  $\pi(D^{*-})$ ), with the  $\bar{D}^0$  decaying into a  $\pi^-$  and  $K^+$ . In the following only one charge sign will be considered, but the processes are also valid for the charge conjugated decays. Two tracks, which kinematically fit best to a pion and a kaon, are combined to a  $\bar{D}^0$ . A further track (pion candidate track) is used for the selection of  $D^{*-}$  candidates. Finally – in combination with another track – the  $B_d$  candidates are built. The single muon skim as described in the previous section is used for this decay mode. The following section describes the exact cuts which were applied to the dataset. The selection is divided into a preselection with loose cuts and a final selection, where the cuts are tightened.

### 6.2.1. Preselection

In the preselection only loose cuts are applied. A mechanism to access the preselection at four different stages is implemented and the selection steps are called TAG, LOOSE, STANDARD and TIGHT. Table 6.4 shows all relevant cut values for these stages. The selection identifiers A.1-G.4 are already explained in the hadronic  $B_s$  selection section. Cuts, which are not explained so far, are labelled with small letters and are explained in the following.

- b.1–b.6: These cuts are equivalent to B.1–B.6, but refer to a kaon instead of a pion.
- e.1: The mass difference  $\Delta m(D^{*-} - D^0)$  has to be consistent with a certain value.

### 6.2.2. Final Selection

For the final selection, the preselection cuts are tightened. The following list summarizes the exact cuts:

- The muon is required to have a reconstructed charge.
- Opposite charges of slow pion (from the  $D^*$  decay) and the pion, associated directly to the  $B_d$ .
- b.3: A transverse momentum of the slow pion higher than  $0.18 \text{ GeV}/c$  ( $p_T(\pi_{D^*}^-) > 0.18 \text{ GeV}/c$ ).

The result of the selection, including the selection applied to the Monte Carlo samples is shown in Figure 6.15, while the number of signal candidates are given in Table 6.5. The yield for RunIIb candidates is significantly lower. The explanation for this behaviour is a track cut of  $p_T = 0.5 \text{ MeV}/c$  in order to save processing time. The introduction of this cut was necessary, as the track multiplicity is higher in RunIIb, due to the increased luminosity.

particle	cut value	ID	TAG	LOOSE	STD	TIGHT
Muon	$n_{\text{SMT}} \geq 2$	A.1	✓	✓	✓	✓
	$n_{\text{CFT}} \geq 2$	A.2	✓	✓	✓	✓
	$n_{\text{seg}}=2$	A.3	✓	✓	✓	✓
	$p_T > 2$ (GeV/c)	A.4	✓	✓	✓	✓
	$p_{\text{tot}} > 3$ (GeV/c)	A.5	✓	✓	✓	✓
	PV	A.6	✓	✓	✓	✓
$K^-$	$n_{\text{SMT}} \geq 2$	B.1	✓	✓	✓	✓
	$n_{\text{CFT}} \geq 2$	B.2	✓	✓	✓	✓
	$p_T > 0.7$ (GeV/c)	B.3	✓	✓	✓	✓
	$ b/\sigma_b  \geq 3$	B.5	✓	✓	✓	✓
	PV	B.6	✓	✓	✓	✓
$\pi^+$	$n_{\text{SMT}} \geq 2$	b.1	✓	✓	✓	✓
	$n_{\text{CFT}} \geq 2$	b.2	✓	✓	✓	✓
	$p_T > 0.7$ (GeV/c)	b.3	✓	✓	✓	✓
	$ b/\sigma_b  \geq 3$	b.5	✓	✓	✓	✓
	PV	b.6	✓	✓	✓	✓
$D^0$	$q(K^-) \cdot q(\pi^+) < 0$	C.1	✓	✓	✓	✓
	$m(K^- \pi^+) \text{ (GeV}/c^2\text{)}$	C.2	[1.3;2.0]	[1.4;2.0]	[1.75;1.95]	[1.78;1.92]
$\pi(D^{*-})$	$n_{\text{SMT}} \geq 2$	D.1	✓	✓	✓	✓
	$n_{\text{CFT}} \geq 2$	D.2	✓	✓	✓	✓
	$\text{jet}(\pi) = \text{jet}(K^-)$	D.4	✓	✓	✓	✓
	$q(\pi) \cdot q(K^-) > 0$	D.5	✓	✓	✓	✓
	PV	D.7	✓	✓	✓	✓
$D^{*-}$	$\Delta m(D^{*-} - D^0) \text{ (GeV}/c^2\text{)}$	e.1	$\leq 0.17$	$\leq 0.17$	$\leq 0.17$	[0.142;0.149]
	$\chi^2$	E.2	$\leq 16$	$\leq 9$	$\leq 9$	$\leq 9$
	$ l_{xy}/\sigma(l_{xy})  \geq 4$	E.3		✓	✓	✓
	$\cos_{xy}(D^{*-}) \geq 0.9$	E.6	✓	✓	✓	✓
$\pi(B_d^0)$	$n_{\text{SMT}} \geq 2$	F.1	✓	✓	✓	✓
	$n_{\text{CFT}} \geq 2$	F.2	✓	✓	✓	✓
	$p_T \text{ (GeV}/c\text{)}$	F.4	$\geq 1$	$\geq 1$	$\geq 1$	$\geq 3$
	$\text{jet}(\pi) = \text{jet}(K^+)$	F.4	✓	✓	✓	✓
	$q(\pi(B_d^0) * \pi(D^{*-})) < 0$	F.4	✓	✓	✓	✓
	PV	F.6	✓	✓	✓	✓
$B_d^0$	$m(K^+ \pi^- \pi \pi) \text{ (GeV}/c^2\text{)}$	G.1				[4.75;5.45]
	$\chi^2 \leq 9$	G.2				✓
	$l_{xy} \geq 0$	G.3				✓
	$l_{xy}/\sigma(l_{xy}) \geq 3$	G.4				✓

**Table 6.4:** Preselection cuts  $B_d$ . The cuts are made from TAG to TIGHT, i.e. all cuts applied during the TAG selection are also applied for the LOOSE selection.

	signal sample	wrong charge combination
RunIIa	644	157
RunIIb	235	38
Total	879	195

**Table 6.5:** Events passing the final selection. The yield for RunIIb candidates is significantly lower, as a track cut of  $p_T = 0.5 \text{ GeV}/c$  was introduced in order to save processing time.



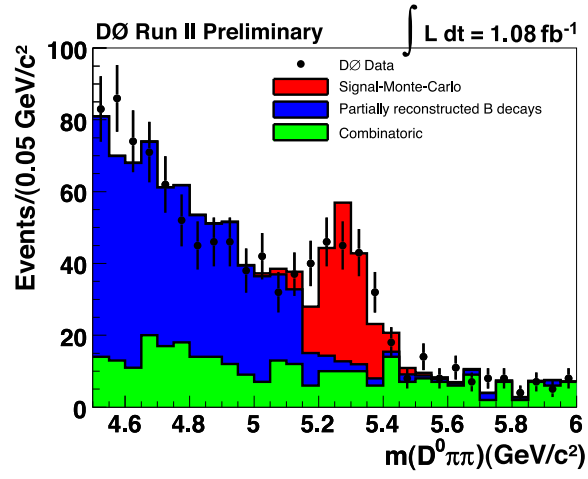


**Figure 6.15:** Comparison of the background decay channels (extracted from the MC samples), signal MC and an integrated luminosity  $\int \mathcal{L} dt = 1.08 \text{ fb}^{-1}$  of RunIIa data [87].



## Lifetime Measurement of $B_d$ and $B_s$ Mesons

Determining the lifetime of the selected  $B_d$  and  $B_s$  mesons provides a check of the selected data sample and the input parameters, as the lifetime is a well-known property<sup>1</sup> [6]. The extraction of the lifetime utilizing an unbinned maximum likelihood fit is described in this chapter. This method is similar to that used to extract the oscillation frequency, as discussed in Chapter 9, and therefore provides an excellent proof of concept. The selections for the  $B_d$  and  $B_s$  candidates are described in Chapter 6.

### 7.1. Lifetime and Decay Length

The following discussion is true for  $B_d$ , as well as for  $B_s$  mesons. On this account  $B$  meson in the equations below has be exchanged with either of these two. As shown in Equation 2.6 the proper decay time,  $t_0$ , of  $B_s$  mesons is given by measuring their decay length  $L_{xy}^B$  and momentum  $p_T(B)$

$$t_0 = x^M / c = L_{xy}^B \frac{M_B}{p_T(B)}. \quad (7.1)$$

The mass is set to the PDG-value  $M_{B_s} = 5.3675 \text{ GeV}/c^2$  ( $M_{B_d} = 5.2795 \text{ GeV}/c^2$ ) [6] for  $B_s$  ( $B_d$ ) mesons. To measure the decay length  $L_{xy}^B$ , the positions of the primary and secondary vertex have to be determined from data.

### 7.2. Extraction of the Lifetime Using an Unbinned Maximum Likelihood Fit

To understand the method to extract the lifetime, it is essential to keep in mind in the following, that a method, relying on theoretical predictions, is used. This means, a certain lifetime is theoretically assumed and afterwards the detector effects are included. A visible proper decay length probability

<sup>1</sup>In this chapter the lifetime is referred as  $c\tau$ . According to its units  $c\tau$  is a length and not a time. However, with the constant  $c$  both values are easy comparable and as the lifetime is usually referred as  $c\tau$  at DØ this terminology is used for consistency reasons.

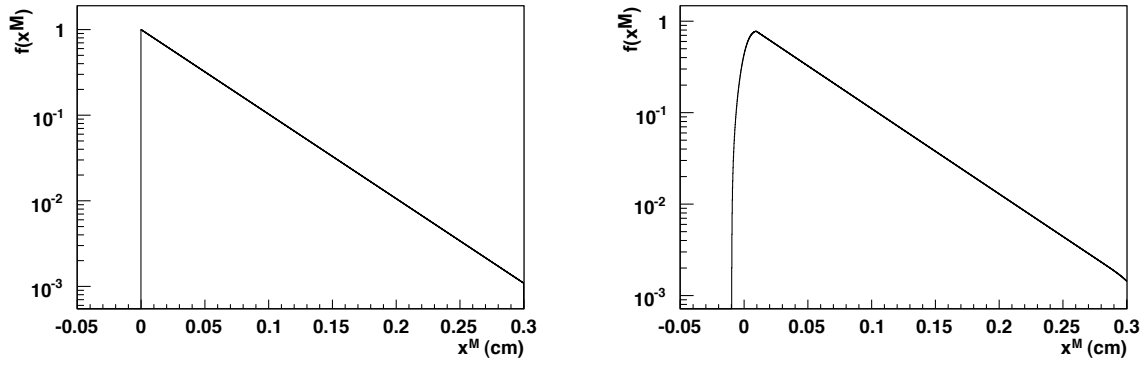


**Figure 7.1:** These plots show the functional principle of the determination of the lifetime measurement. Under the assumption of a specific lifetime, the distribution of  $B$  meson proper decay time is shown (left). After detector effects are taken into account, the distribution of visible proper decay lengths of the  $B_s$  meson sample is obtained (right).

distribution is determined for each event at the assumed lifetime, taking into account the measurement uncertainties of each single event. In the end the probability for each event is obtained by using the value of the distribution at the reconstructed visible proper decay length. By repeating this procedure for each event, adding its logarithmic value and scanning over several lifetimes, a distribution is obtained, showing the value with the most likely average lifetime. The advantage of this procedure is, that well-known detector effects are folded into the theoretical description and compared to the experimentally obtained result. This implementation is much easier than using the experimental result and unfolding the detector effects to obtain the true value. In this section only the influence on the inputs to the fit are described. A detailed explanation on how to obtain the inputs themselves is given in the next section.

Constructing the prediction starts by calculating the proper decay time distribution under the assumption of a certain lifetime

$$f(ct_0) = e^{-\frac{ct_0}{c\tau_B}}. \quad (7.2)$$

Therefore, for each theoretically assumed lifetime a plot as shown on the left-hand side of Figure 7.1 is obtained. As discussed in Section 2.3, there is an uncertainty caused by partially reconstructed decays. This uncertainty is taken into account by applying the  $k$ -Factor to yield a visible proper decay length  $ct_0 = k \cdot x_{\text{true}}$ . The equation of the lifetime distribution changes to

$$f(x_{\text{true}}) = \int_0^\infty e^{-\frac{kx_{\text{true}}}{c\tau_B}} \rho(k) dk, \quad (7.3)$$

where  $\rho(k)$  are distributions determined through Monte Carlo studies and are described in the next section. Furthermore, it is not possible to measure the visible proper decay length without an uncertainty. This is taken into account by smearing the just obtained equation with the detector resolution

$$f(x_{\text{meas}}^M) = \int_{-\infty}^{+\infty} \int_0^\infty G(x_{\text{meas}}^M - x_{\text{true}}; \sigma_{x_{\text{meas}}^M}) e^{-\frac{kx_{\text{true}}}{c\tau_B}} \rho(k) dk dx_{\text{true}}. \quad (7.4)$$

In this equation  $G(x_{\text{meas}}^M - x_{\text{true}}; \sigma_{x_{\text{meas}}^M})$  is a function reflecting the finite resolution for measuring  $x_{\text{meas}}^M$  with the standard deviation  $\sigma_{x_{\text{meas}}^M}$ , which is determined event-wise. These two effects cause the lifetime distribution (Figure 7.1 (left)) to change. The right-hand side plot of Figure 7.1 reflects these changes, when taking the partially reconstructed events and the detector resolution into account.

Finally, the selection efficiency,  $\epsilon(x_{\text{meas}}^M)$ , and combinatorial background contamination are dependent on the measured visible proper decay length. Taking both of these into account yields the final predicted distribution, to be compared with data

$$f(x_{\text{meas}}^M) = \epsilon(x_{\text{meas}}^M) \left[ \frac{1}{1 - f_{bg}(x_{\text{meas}}^M)} \right] f(x_{\text{meas}}^M). \quad (7.5)$$

In this equation it is assumed, that the signal and background have the same efficiency as a function of  $x_{\text{meas}}^M$ . Obviously, it is essential to determine the inputs properly.

### 7.3. Input Parameters to the Fit

In the previous section, the application of different detector effects was described. This section deals with the determination of these input parameters.

#### 7.3.1. K-Factor

As it is not possible to select only fully reconstructable hadronic decays with the DØ detector (the  $p_T$  resolution is limited by the lever arm), also the partially reconstructed decays have to be taken into account. This is done via the  $k$ -Factor, which is obtained through Monte Carlo simulations. The distribution

$$k = \frac{p_T(B_{\text{reco}})}{p_T(B_{\text{truth}})} \quad (7.6)$$

is plotted for four different visible mass bins in the range  $4.75 \text{ GeV}/c^2 < m(B_s) < 5.5 \text{ GeV}/c^2$  (with a slightly smaller mass window in the case of  $B_d$ :  $4.75 \text{ GeV}/c^2 < m(B_d) < 5.45 \text{ GeV}/c^2$ ), where  $p_T(B_{\text{reco}})$  is the transverse momentum of all reconstructed particles and  $p_T(B_{\text{truth}})$  is the true information from Monte Carlo. To parametrize the  $k$ -Factor an asymmetric Gaussian function

$$\rho(k) = \frac{1}{\sqrt{2\pi}p_2} (p_0 + p_3 k) e^{-\frac{(k-p_1)^2}{2p_2^2}} \quad (7.7)$$

is fitted to each mass bin distribution. The usage of an asymmetric function is justified, as a  $k$ -Factor of one represents the case, where the true momentum is reconstructed. Hence, a  $k$ -Factor greater than one is only possible due to detector smearing effects and values in the interval zero to one are more likely. Figure 7.2 shows the fitting results obtained from Monte Carlo for  $B_s$  decays. The exact parameters obtained from the fitting procedure are shown in Table 7.1 for the hadronic  $B_s$  and  $B_d$  mode.

#### 7.3.2. Resolution of the Visible Proper Decay Length

It is not possible to measure the flight length of the  $B_s$  meson with infinite precision. The accuracy with which the flight length is determined for a specific event depends on the pattern of hits in the tracking detectors. To quantify this uncertainty, a method classifying each event by its hit pattern in the tracking system of the DØ detector was developed as explained in Section 5.2 and [78]. By applying this event-by-event determination of the resolution an estimated improvement of 5% is expected at an oscillation frequency of  $\Delta m_s = 17 \text{ ps}^{-1}$  and of 7.3% at  $\Delta m_s = 20 \text{ ps}^{-1}$  compared to the use of average resolution values.

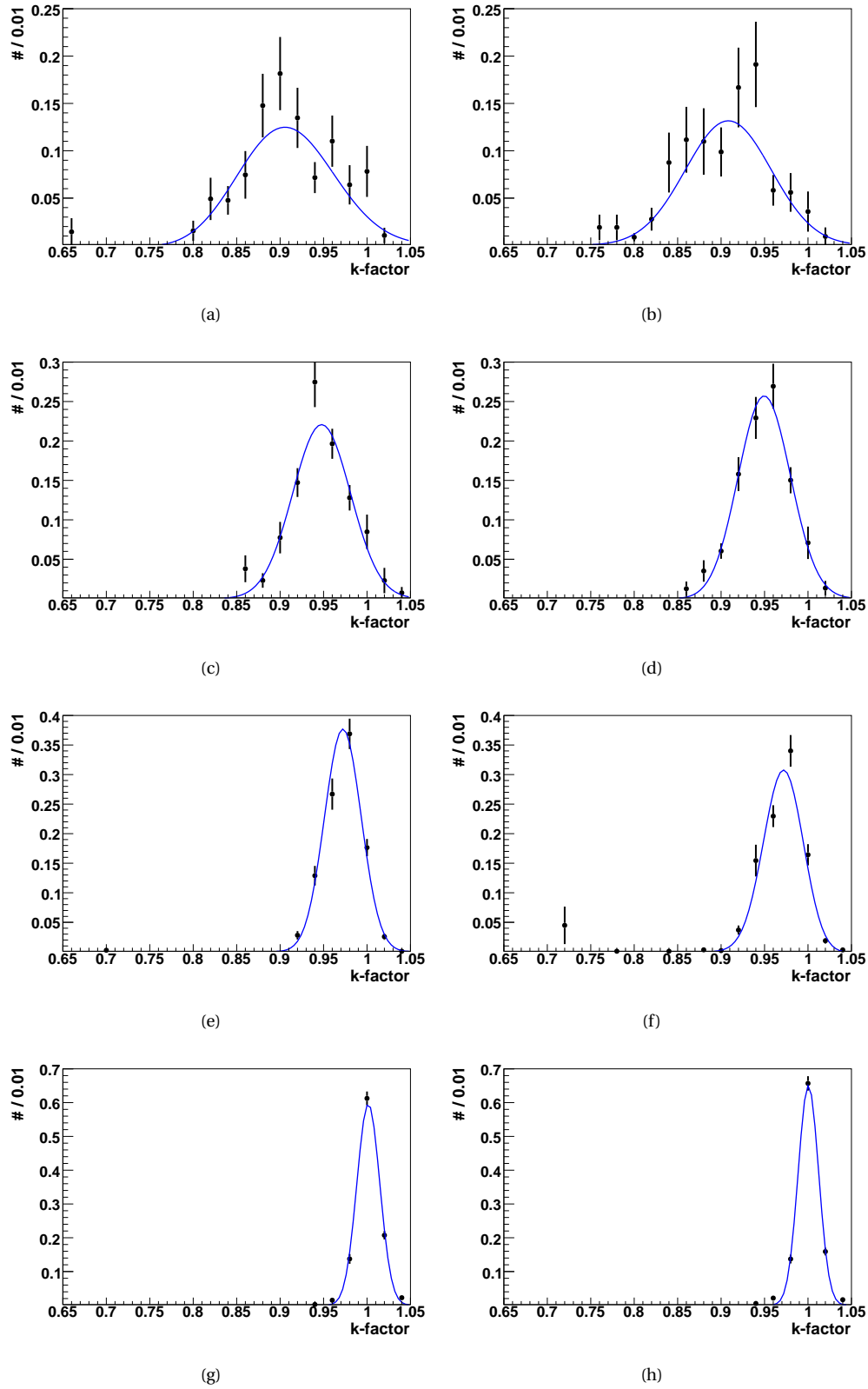


**Figure 7.2:** K-Factor distributions, as obtained for  $B_s$  decays from Monte Carlo studies. The distributions are determined for four different mass bins. (a) RunIIa,  $4.75\text{GeV}/c^2 < m(B_s) < 4.95\text{GeV}/c^2$ , (b) RunIIb,  $4.75\text{GeV}/c^2 < m(B_s) < 4.95\text{GeV}/c^2$ , (c) RunIIa,  $4.95\text{GeV}/c^2 < m(B_s) < 5.15\text{GeV}/c^2$ , (d) RunIIb,  $4.95\text{GeV}/c^2 < m(B_s) < 5.15\text{GeV}/c^2$ , (e) RunIIa,  $5.15\text{GeV}/c^2 < m(B_s) < 5.30\text{GeV}/c^2$ , (f) RunIIb,  $5.15\text{GeV}/c^2 < m(B_s) < 5.30\text{GeV}/c^2$ , (g) RunIIa,  $5.30\text{GeV}/c^2 < m(B_s) < 5.50\text{GeV}/c^2$ , (h) RunIIb,  $5.30\text{GeV}/c^2 < m(B_s) < 5.50\text{GeV}/c^2$ .

	Fit Para- meter	$B_s$				$B_d$			
		RunIIa		RunIIb		RunIIa		RunIIb	
		Value	Error	Value	Error	Value	Error	Value	Error
I	$p_0$	-0.421	$\pm 0.422$	0.074	$\pm 0.109$	0.071	$\pm 1.143$	1.240	$\pm 1.425$
	$p_1$	0.882	$\pm 0.028$	0.908	$\pm 0.006$	0.906	$\pm 0.088$	0.996	$\pm 0.081$
	$p_2$	0.593	$\pm 0.101$	0.049	$\pm 0.004$	0.070	$\pm 0.009$	0.071	$\pm 0.031$
	$p_3$	0.558	$\pm 0.488$	-0.001	$\pm 0.120$	0.000	$\pm 1.193$	-1.193	$\pm 1.414$
II	$p_0$	0.101	$\pm 0.084$	-0.085	$\pm 0.088$	0.316	$\pm 0.150$	4.572	$\pm 3.800$
	$p_1$	0.948	$\pm 0.002$	0.0.941	$\pm 0.002$	0.961	$\pm 0.003$	1.002	$\pm 0.047$
	$p_2$	0.033	$\pm 0.002$	0.0.031	$\pm 0.002$	0.026	$\pm 0.003$	0.049	$\pm 0.015$
	$p_3$	0.000	$\pm 0.089$	1.019	$\pm 0.095$	-0.210	$\pm 0.156$	-4.557	$\pm 3.800$
III	$p_0$	0.137	$\pm 0.084$	1.829	$\pm 0.357$	5.521	$\pm 0.542$	4.937	$\pm 1.039$
	$p_1$	0.972	$\pm 0.001$	0.980	$\pm 0.003$	0.997	$\pm 0.001$	0.998	$\pm 0.001$
	$p_2$	0.021	$\pm 0.000$	0.024	$\pm 0.000$	0.013	$\pm 0.000$	0.013	$\pm 0.001$
	$p_3$	0.000	$\pm 0.087$	-1.752	$\pm 0.359$	-5.363	$\pm 0.539$	-4.775	$\pm 1.037$
IV	$p_0$	-2.015	$\pm 0.071$	-1.625	$\pm 0.076$	0.180	$\pm 0.093$	-5.348	$\pm 0.714$
	$p_1$	0.999	$\pm 0.000$	0.999	$\pm 0.000$	1.014	$\pm 0.000$	1.006	$\pm 0.002$
	$p_2$	0.013	$\pm 0.000$	0.019	$\pm 0.000$	0.122	$\pm 0.000$	0.015	$\pm 0.001$
	$p_3$	2.187	$\pm 0.071$	1.803	$\pm 0.076$	0.000	$\pm 0.092$	5.483	0.715

**Table 7.1:** Overview of the fitting parameters for the  $k$ -Factor. These parameters are obtained through Monte Carlo studies by comparing the reconstructed momentum with the truth information. The roman numbers on the left-hand side correspond to the four mass bins  $4.75 \text{ GeV}/c^2 < m(B_s) < 4.95 \text{ GeV}/c^2$ ,  $4.95 \text{ GeV}/c^2 < m(B_s) < 5.15 \text{ GeV}/c^2$ ,  $5.15 \text{ GeV}/c^2 < m(B_s) < 5.30 \text{ GeV}/c^2$  and  $5.30 \text{ GeV}/c^2 < m(B_s) < 5.50 \text{ GeV}/c^2$ . The last mass window is slightly smaller for the  $B_d$  selection:  $5.30 \text{ GeV}/c^2 < m(B_s) < 5.45 \text{ GeV}/c^2$ . The stated error corresponds to the uncertainty of the fit only.

Fit Para- meter	$B_s$				$B_d$			
	RunIIa		RunIIb		RunIIa		RunIIb	
	Value	Error	Value	Error	Value	Error	Value	Error
$p_0$	0.388	$\pm 0.122$	0.472	$\pm 0.152$	0.416	$\pm 0.070$	2.697	$\pm 0.095$
$p_1$ (1/cm)	-0.509	$\pm 3.304$	-7.959	$\pm 3.569$	-4.193	$\pm 1.784$	-4.228	$\pm 2.638$
const.	0.083		0.074		0.086		0.1125	

**Table 7.2:** Fitting parameters of the background fit for  $B_s$  and  $B_d$  mesons for both run periods. The stated error corresponds to the uncertainty of the fit only. Hence, no error for the constant term is given, as it is not determined within the fit.

### 7.3.3. Background

Most of the background occurs by adding a wrong pion to the selected  $D_s^-$ . For the background estimation, data events, where a pion and a  $D_s^-$  meson with the same charge as the pion are combined. To estimate the background fraction, the VPDL distributions of data for these “wrong sign” were divided by VPDL distributions in “right sign”  $B_s$  candidate events. This assumes equal probability for a background event to “wrong sign” or “right sign”. The background fraction is parametrized by a straight line for all visible proper decay lengths below 0.06 cm

$$f_{bg}(x^M) = \frac{N_{bg}}{N_{all}} = p_0 + p_1 \cdot x^M, \quad (7.8)$$

where  $p_0$  and  $p_1$  are the fitting parameters. Due to low statistics the background can not be well-modeled by this parametrization for events with  $x^M > 0.06$  cm. Therefore, all events above this value are used to determine a constant background fraction. It has been tested, that events with a higher VPDL have negligible influence on the result of the fit. Table 7.2 shows the parameters for the linear

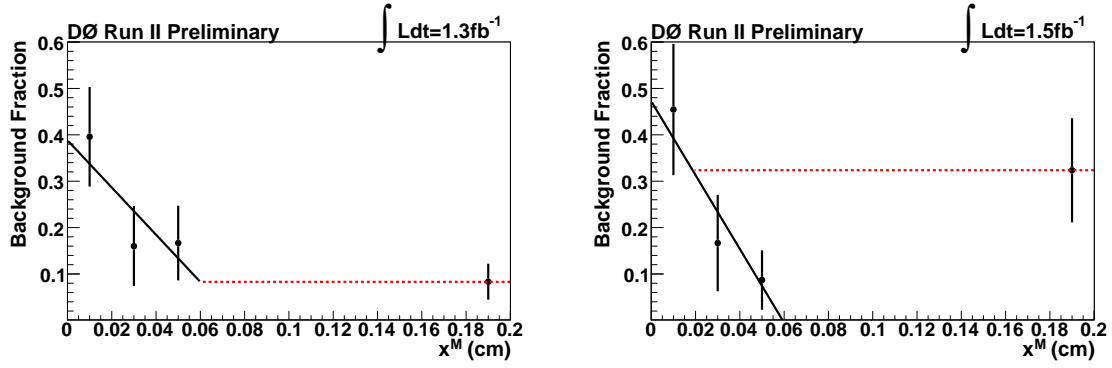


**Figure 7.3:** Background distributions for RunIIa (left) and RunIIb (right)  $B_s$  data. The distributions are obtained by dividing the sample with wrong charged pion correlation by the sample with the correct pion charge correlation. All values below  $x^M < 0.06$  cm are fitted by a straight line. All other events are used to determine a constant background fraction for longer visible proper decay lengths. For the lifetime fit, the linear distribution is used, until it drops below the constant value. For higher VPDs the constant value is used, which is indicated by a red dotted line in the plots.

Fit Para- meter	$B_s$				$B_d$			
	RunIIa		RunIIb		RunIIa		RunIIb	
	Value	Error	Value	Error	Value	Error	Value	Error
$p_0$	0.951	$\pm 0.055$	0.949	$\pm 0.050$	0.949	$\pm 0.460$	0.925	$\pm 0.039$
$p_1$ (cm)	0.055	$\pm 0.040$	0.048	$\pm 0.047$	0.030	$\pm 0.005$	0.015	$\pm 0.018$
$p_2$ (1/cm)	-34.789	$\pm 14.211$	-42.592	$\pm 17.095$	-0.706	$\pm 16.735$	-0.438	$\pm 423.558$
$p_3$ (1/cm <sup>2</sup> )	481.355	$\pm 622.794$	728.649	$\pm 786.250$	1260.60	$\pm 693.339$	-893.707	$\pm 22104.1$
$p_4$ (1/cm <sup>3</sup> )	-1238.78	$\pm 7875.16$	-3085.83	$\pm 13450.0$	10000.0	$\pm 11025.9$	-10000.0	$\pm 19466.1$

**Table 7.3:** Overview of the fitting parameters for the selection efficiency as obtained from Monte Carlo for RunIIa and RunIIb.

function as obtained from the fit of data. The corresponding functions for  $B_s$  mesons are shown in Figure 7.3. The higher background fraction of RunIIb data is explainable by the higher instantaneous luminosity and the resulting more complicated underlying events that result [98].

### 7.3.4. Selection Efficiency

The selection efficiency takes into account the influence of lifetime biasing cuts in the selection, as described in Chapter 6. The efficiency to select an event is dependent on the visible proper decay length. While it is very unlikely to select a signal candidate for short  $x^M$ , the efficiency raises to almost one for longer VPDs ( $x^M > 0.04$  cm). The selection efficiency is obtained through Monte Carlo studies by dividing the VPD distribution of Monte Carlo events after the final selection by the events obtained by the same selection without lifetime biasing cuts. The distribution obtained is fitted by the function

$$\epsilon(x_{\text{meas}}^M) = p_0 \cdot \left( 1 - e^{-\left(\frac{x_{\text{meas}}^M}{p_1}\right)^2} \left( 1 + p_2 \cdot x_{\text{meas}}^M + p_3 \cdot (x_{\text{meas}}^M)^2 + p_4 \cdot (x_{\text{meas}}^M)^3 \right) \right). \quad (7.9)$$

The results of these fits are plotted in Figure 7.4, while the fit parameters,  $p_0 - p_4$ , as obtained for RunIIa and RunIIb Monte Carlo are shown in Table 7.3.



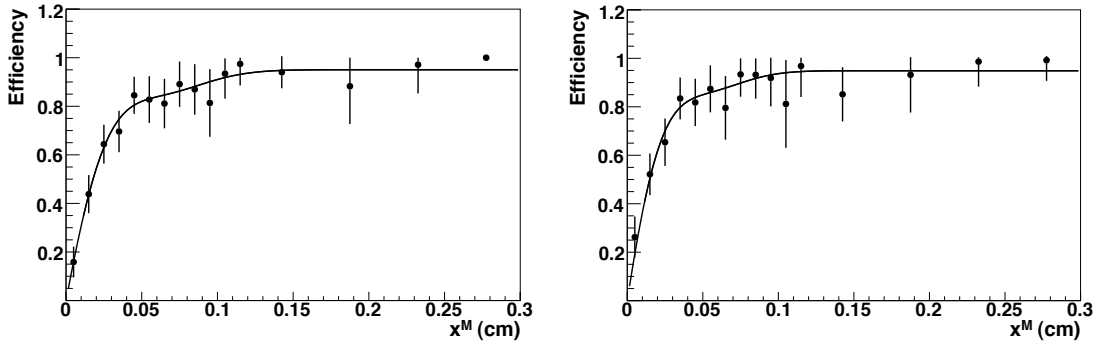


**Figure 7.4:** The selection efficiency vs. the visible proper decay length. The distributions are obtained by dividing the VPDL distribution of Monte Carlo events after the final selection by the events obtained by the same selection without lifetime biasing cuts for RunIIa (left) and RunIIb (right).

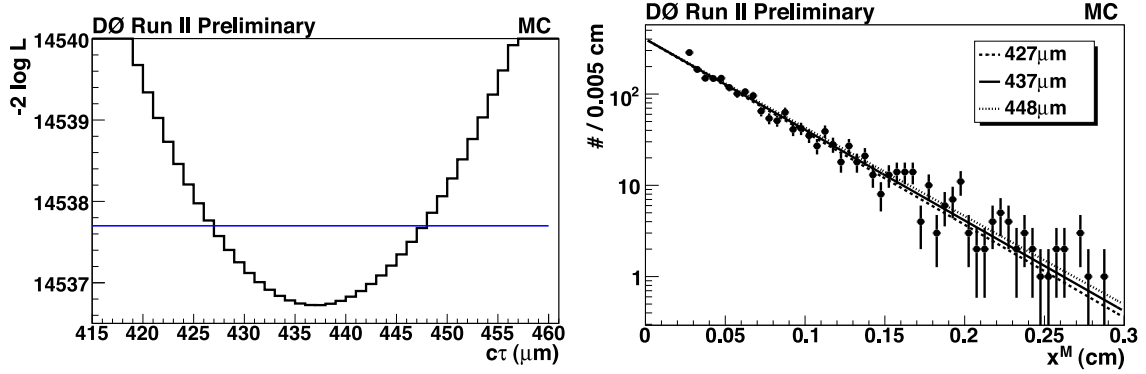


**Figure 7.5:** The lifetime fit as obtained from the RunIIb  $B_s$  signal Monte Carlo  $B_s \rightarrow D_s^+ \pi^-$ . The plot on the left shows the results of the likelihood fit with the straight line corresponding to the  $1\sigma$  uncertainty interval. The plot on the right shows the comparison of the determined lifetime with the distribution of the visible proper decay length. For this plot the MC distribution was corrected with the selection efficiency.

## 7.4. Results

The results of the fitting procedure, as described in the previous section, are shown here. This includes a consistency check with Monte Carlo, as well, as the measurement for RunIIa and RunIIb data for a selection of hadronic  $B_d$  and  $B_s$  decays.

### 7.4.1. Applying the Fit to a Monte Carlo Sample

After implementing the described procedure, it is crucial to check the lifetime fit with a sample with known inputs. Thus, the fit was applied to Monte Carlo. To avoid any uncertainties, only the signal Monte Carlo  $B_s \rightarrow D_s^+ \pi^-$  (as described in Section 5.5) was used. The background was set to zero and the efficiency was determined with the signal Monte Carlo only for this check. At the time of generating the Monte Carlo sample the world average of the  $B_s$  meson lifetime was  $c\tau = 438 \mu\text{m}$ . Hence, this value was used. From this signal Monte Carlo sample a lifetime of

$$c\tau_{\text{RunIIa-MC}} = (451^{+11}_{-14}(\text{stat}))\mu\text{m}, \quad (7.10)$$

$$c\tau_{\text{RunIIb-MC}} = (437^{+11}_{-10}(\text{stat}))\mu\text{m}. \quad (7.11)$$

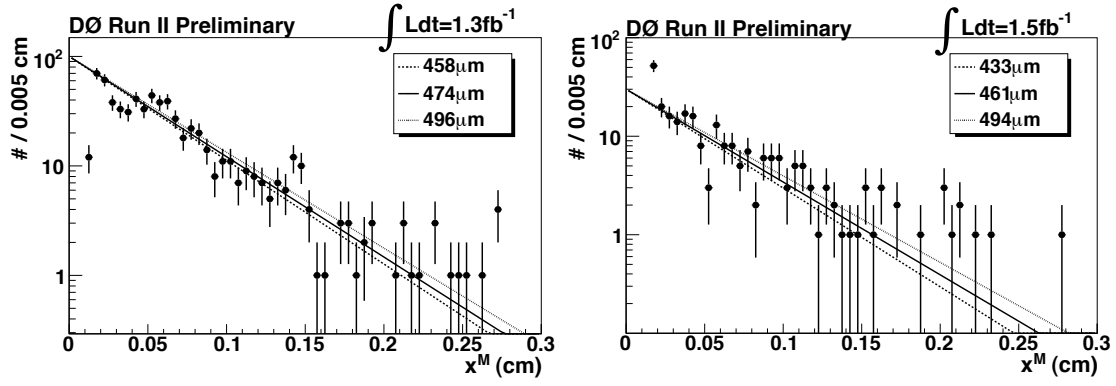


**Figure 7.6:** The lifetime fit as obtained from the  $B_d$  selection sample. Shown are the obtained fit values, as well as the  $\pm 1\sigma$  statistical uncertainties. For this plot the data was corrected with the selection efficiency in order to be able to directly compare the fit with the data distribution. RunIIa data is shown on the left, while the right-hand side plot shows RunIIb data.

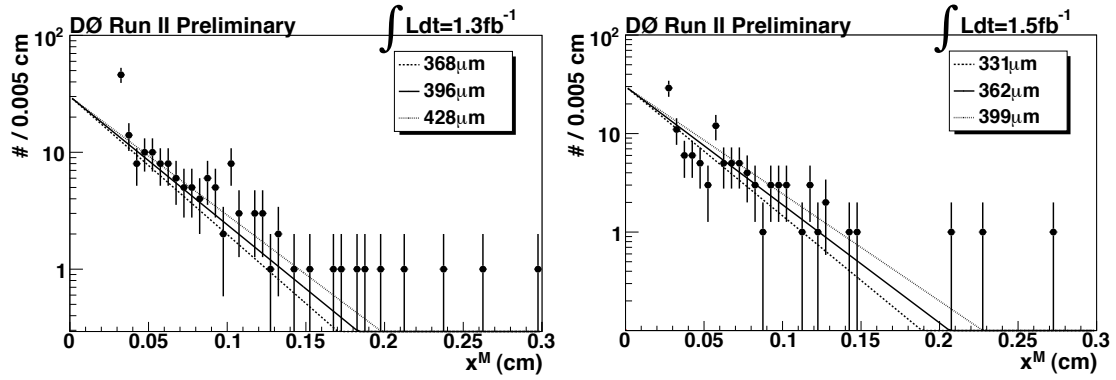


**Figure 7.7:** The lifetime fit as obtained from the  $B_s$  selection sample. Shown are the obtained fit values, as well as the  $\pm 1\sigma$  statistical uncertainties. For this plot the data was corrected with the selection efficiency in order to be able to directly compare the fit with the data distribution. RunIIa data is shown on the left, while the right-hand side plot shows RunIIb data.

was obtained. This is in agreement with the assumed lifetime within its statistical uncertainties. Figure 7.5 (left) shows the results of the lifetime fit, as obtained from the likelihood fit. The minimum indicates the most probable decay length. The blue line shows the  $1\sigma$  uncertainty. The plot on the right-hand side presents the lifetime value as obtained by the fit in comparison with the Monte Carlo sample. For this plot the Monte Carlo sample was corrected with the selection efficiency in order to be able to directly compare the fit with the Monte Carlo distribution. Furthermore, the  $\pm 1\sigma$  distributions are shown as dotted lines.

#### 7.4.2. Applying the Fit to Data

The full dataset of  $\int \mathcal{L} dt = 2.8 \text{ fb}^{-1}$  is used for this measurement. The two run periods RunIIa and RunIIb are handled separately. The same final selection as used in the previous section and described in Chapter 6 is used for the lifetime of  $B_s$  and  $B_d$  mesons. For the latter case the lifetime is determined as

Systematic (uncertainties in $\mu\text{m}$ )	$B_s$		$B_d$	
	RunIIa	RunIIb	RunIIa	RunIIb
Efficiency	$\pm 13$	$\pm 13$	$\pm 10$	$\pm 5$
Background	$< \pm 0.1$	$< \pm 0.1$	$< \pm 0.1$	$< \pm 0.1$
k-Factor	$\pm 8$	$^{+8}_{-7}$	$\pm 10$	$^{+10}_{-9}$
Resolution	$< \pm 0.1$	$< \pm 0.1$	$\pm 1$	$< \pm 0.1$

**Table 7.4:** Summary of the contributions to the systematic uncertainty of the lifetime fit. The deviations are given in  $\mu\text{m}$ . The efficiency and the k-Factor add the highest uncertainties to the measurement, as their determination is limited by the available Monte Carlo samples.

$$c\tau_{B_d, \text{RunIIa}} = (474^{+22}_{-16}(\text{stat}))\mu\text{m}, \quad (7.12)$$

$$c\tau_{B_d, \text{RunIIb}} = (461^{+33}_{-29}(\text{stat}))\mu\text{m}. \quad (7.13)$$

Notable is the fact, that the statistical uncertainty of the RunIIb dataset is higher than for RunIIa data, although the integrated luminosity is higher for RunIIb. The reason is a lower  $B_d$  candidate yield, which is caused by an additional cut on the transverse momentum on the tracks, as described in Section 6.2.2. A comparison of the lifetime value obtained with the selected data is shown in Figure 7.6.

For the  $B_s$  mesons the lifetime is extracted as

$$c\tau_{B_s, \text{RunIIa}} = (396^{+32}_{-28}(\text{stat}))\mu\text{m}, \quad (7.14)$$

$$c\tau_{B_s, \text{RunIIb}} = (362^{+37}_{-31}(\text{stat}))\mu\text{m}. \quad (7.15)$$

Figure 7.7 shows these lifetimes in comparison with RunIIa and RunIIb data. As there are uncertainties on the inputs to the fit, all their contributions are described in the following section.

### 7.4.3. Systematic Uncertainties

Detailed studies to quantify the impact of the uncertainties of the input parameters on the result of the fit were performed. The efficiency is the main contribution to the systematic uncertainties. The main cause for the high contribution is the limited statistics, used to determine the fitting parameters. The size of the uncertainty was estimated by using a different efficiency parametrization in the fits

$$\epsilon(x_{\text{meas}}^M) = p_0 \cdot \left( 1 - e^{-\left(\frac{x_{\text{meas}}^M}{p_1}\right)^2} \right). \quad (7.16)$$

For the background two different contributions were checked. At first the offset of the linear fit was varied by  $\pm 20\%$ . Then the slope was varied by  $\pm 20\%$ , but using the original offset again. For the contribution of the k-Factor to the systematic uncertainties, a  $\pm 2\%$  shift of the k-Factor distribution was computed and used as systematic input. The choice of a 2% variation originated from intensive studies [99]. For this analysis in particular, there are three possible sources of systematic uncertainties for the k-Factors

- differences in k-Factor distributions using generator-level information versus reconstructed momentum (1.2%) [100],
- dependence of the k-factor on the  $B$  meson momentum (2% [99]), and
- using EvtGen values for relative  $B_s \rightarrow \pi D_s(\phi\pi)X$  signal decays where PDG values are unavailable (2.1% as the worst-case).

The largest effect is expected to come from the last of these items, and is estimated to be covered by the 2% shift in the  $k$ -Factor means. A Gaussian function, with width set by the topology-dependent VPDL uncertainty for the event in question, is used to parametrize the resolution function. Resolution-based systematic effects are estimated by scaling the VPDL uncertainties by  $\pm 20\%$ . Table 7.4 shows an overview on the impact of the contributions to the systematic uncertainties. Only the efficiency and the  $k$ -Factor distributions show a non negligible impact on the lifetime measurement. Their determination is limited by the available Monte Carlo samples.

#### 7.4.4. Final Results of the Lifetime Measurement

In combination with the systematical uncertainties the lifetimes of the  $B_d$  mesons are extracted as

$$c\tau_{B_d, \text{RunIIa}} = (474^{+22}_{-16}(\text{stat}) \pm 14(\text{sys}))\mu\text{m}, \quad (7.17)$$

$$c\tau_{B_d, \text{RunIIb}} = (461^{+33}_{-29}(\text{stat})^{+11}_{-10}(\text{sys}))\mu\text{m}. \quad (7.18)$$

These values are in agreement (within  $\pm 1\sigma$ ) with the PDG value [6] of  $c\tau_{B_d} = (459 \pm 2.5)\mu\text{m}$ . The lifetime of the  $B_s$  mesons is determined as

$$c\tau_{B_s, \text{RunIIa}} = (396^{+32}_{-28}(\text{stat}) \pm 15(\text{sys}))\mu\text{m}, \quad (7.19)$$

$$c\tau_{B_s, \text{RunIIb}} = (362^{+37}_{-31}(\text{stat}) \pm 15(\text{sys}))\mu\text{m}. \quad (7.20)$$

Compared to the world-average of  $c\tau_{B_s} = (439.8 \pm 17.7)\mu\text{m}$  [6], the RunIIa data is in agreement within its statistical and systematical error, while the lifetime obtained from RunIIb data is too short (by about  $\pm 1.5\sigma$ ). Differences between the fitted and true lifetimes are expected, however, because of uncertainties in modeling the VPDL-dependent efficiency. Therefore, the lifetimes obtained are used in the measurement of the oscillation frequency (Chapter 9) to correct for mis-modeled efficiency.

As these results are in general agreement with the world-average, the extraction of the lifetime with an unbinned loglikelihood fit can be considered as the correct approach. Hence, this method is also used to determine the oscillation frequencies in the  $B_d$  and  $B_s$  system, as described in Chapter 9. The only difference to this method, is taking into account the information, whether an event oscillated or not. Information on the reliability of this tag is included via the dilution, as discussed in Chapter 8. How to obtain this information is described in the next chapter.

## Initial and Final State Flavor Tagging

One of the key pieces of information for a successful oscillation analysis is the knowledge of the flavor content of the  $B_s$  meson in the initial and final state to determine, whether it has mixed or not. While the flavor in the final state is given by the charges of the decay particles, more sophisticated methods are needed for the initial state. As described in Section 2.2 the initial state can be determined by either examining the opposite side decay (OST) or studying the signal (same) side itself (SST). Same side flavor tagging is not used in this analysis, although it is used in the  $B_s \rightarrow \mu\nu_\mu D_s(\phi\pi)$  mode. This is justified, as the signal events must contain a muon on the opposite side in order to trigger on it. This is described in detail in Chapter 4. Further information about the exact implementation of the SST at DØ and the tagging performance is described in [101]. As the OST takes into account the decay on the opposite side only and does not rely on the decay on the signal side itself, a proper determination of the tagging power can be done by studying  $B_d$  decays [95].

### 8.1. Opposite Side Tagging Classes

Different OST methods are grouped into classes and priorities are assigned to each class depending on the information available in a given event. These classes are described in the following sections. If an additional muon is found in the decay, the muon jet charge (Section 8.1.1) and the secondary vertex jet charge (Section 8.1.2) are used. If no additional muon is identified and an additional electron is found, the electron jet charge (Section 8.1.3) is used. If no additional electron is found, the secondary vertex jet charge (Section 8.1.2) and the event jet charge (Section 8.1.4) are used. For each event, all available classes are combined into the tagging variable  $d$  (Section 8.1.5).

#### 8.1.1. Muon Tagging

For the opposite side muon tagging only muons, which are not in the same jet as the reconstructed  $B$  Meson, are taken into account. Therefore, the three-momenta of the muon  $\vec{p}_\mu$  and  $B$  Meson  $\vec{p}_B$  have to fulfill the requirement

$$\cos\phi(\vec{p}_\mu, \vec{p}_B) < 0.8. \quad (8.1)$$

If several muons are outside the jet, only the muon with the highest number of hits in the muon system, or, that being equal, with the highest transverse momentum is used. The muon jet charge

$$Q_J^\mu = \frac{\sum_i q_i p_{T,i}}{\sum_i p_{T,i}} \quad (8.2)$$

is determined, where  $q_i$  is the charge of the  $i$ -th track with the transverse momentum  $p_{T,i}$ . All charged particles within the cone

$$\Delta\mathcal{R} = \sqrt{(\Delta\phi)^2 + (\Delta\eta)^2} < 0.5 \quad (8.3)$$

around the transverse momentum of the muon are taken into account in this sum, with the exception of tracks contributing to the B meson candidate.

### 8.1.2. Secondary Vertex Tagging

A secondary vertex may occur, due to the long lifetime of  $B$  mesons. These vertices are reconstructed using the vertex finder of the DELPHI experiment [102], requiring at least two tracks with a transverse impact parameter significance greater than three in order to be associated with the vertex. Furthermore, the distance between the primary and secondary vertex has to be measured precisely ( $D_{xy} > 4\sigma(d_{xy})$ ). All momenta of the particles related to the secondary vertex are summed up, if they satisfy the condition

$$\cos\phi(\vec{p}_{SV}, \vec{p}_B) < 0.8. \quad (8.4)$$

Therefore, the secondary vertex jet charge is defined as

$$Q_J^{SV} = \frac{\sum_i (q_i p_{L,i})^k}{\sum_i (p_{L,i})^k}, \quad (8.5)$$

where  $q_i$  and  $p_{T,i}$  are defined similar to the opposite side muon jet charge tagging. The exponent  $k$  was determined as  $k = 0.6$  through extensive studies [95].

### 8.1.3. Electron Tagging

The electron candidates taken into account for tagging have to fulfill standard electron selection criteria [103]. Additionally the electrons have to be reconstructed within the central region of the calorimeter,  $|\eta| < 1.1$ , have to have a transverse momentum of at least  $2 \text{ GeV}/c$  and are required to have at least two hits in the SMT and CFT each. A jet condition

$$\cos\phi(\vec{p}_e, \vec{p}_B) < 0.5 \quad (8.6)$$

is used to veto on electrons associated to the  $B$  meson. Similar to the muon jet charge, a cone is defined to calculate the electron jet charge

$$Q_J^e = \frac{\sum_i q_i p_{L,i}}{\sum_i p_{L,i}}. \quad (8.7)$$

Again  $q_i$  and  $p_{T,i}$  are defined analogously to the opposite side muon jet charge tagging variables.

### 8.1.4. Event Charge Tagging

The event jet charge tagging variable is highly correlated with the opposite side muon jet charge and thus is not used if a muon is identified. The charge  $q_i$  and the transverse momentum  $p_{T,i}$  are used to construct the event charge

$$Q_J^{\text{EC}} = \frac{\sum_i q_i p_{T,i}}{\sum_i p_{T,i}}. \quad (8.8)$$

All tracks  $i$ , having a transverse momentum  $p_T > 0.5 \text{ GeV}/c$  and

$$\Delta\mathcal{R} = \sqrt{(\Delta\phi)^2 + (\Delta\eta)^2} > 1.5 \quad (8.9)$$

relative to the reconstructed  $b$  hadron, are taken into account.

### 8.1.5. Combined Tagging Variable

The performance of the tagging methods is very different and each event allows only a subset of all methods to be used. Therefore, a combined tagging variable  $d$  is determined for every event. A likelihood ratio method, similar to the likelihood selection variable (section 6.1.2), is used to take into account the weights of performance differences. For each method  $i$  the ratio

$$r_i = \frac{f_i^{\bar{b}}}{f_i^b} \quad (8.10)$$

is determined, where  $f_i^{\bar{b}}$  ( $f_i^b$ ) are the probabilities of a  $\bar{b}$  ( $b$ ) quark in the initial state given the observed variables for the event. If a method  $i$  is not defined for a decay, the value  $r_i$  is set to one. Afterwards all variables are multiplied

$$r = \prod_{i=1}^n r_i. \quad (8.11)$$

Hence, the combined variable  $r$  indicates a higher probability for a  $b$  ( $\bar{b}$ ) quark, if  $r$  is smaller (greater) than one. Usually the combined tagging variable  $d$ , which is defined as

$$d = \frac{1-r}{1+r} \quad (8.12)$$

is used to tag the initial state. It varies between  $-1 < d < 1$ . Negative (positive) values indicate  $\bar{b}$  ( $b$ ) quarks. The more negative or positive the value of  $d$ , the more likely the correct state is found.

## 8.2. Tagging Performance

As the production rate of  $B_d$  decays is about factor four higher than for  $B_s$  decays (Section 1.4), higher statistics are achieved with the same data set and thus, a measurement with less statistical uncertainties is possible. To check the consistency of the measurement, the mass difference  $\Delta m_d$  was determined and compared with the PDG value.

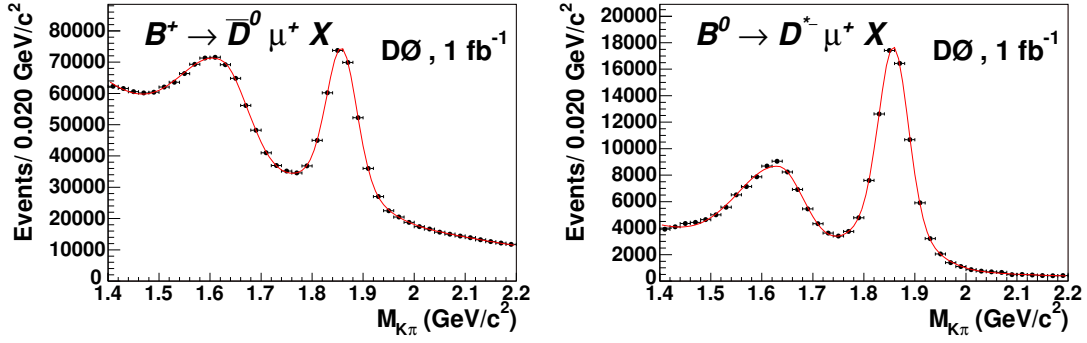


**Figure 8.1:** Invariant  $K\pi$  masses. Left:  $D^0$  sample with  $230551 \pm 1627$  reconstructed signal candidates. Right:  $D^*$  sample with  $73532 \pm 304$  candidates [95], called  $D^{*-}$  and  $D^0$ .

### 8.2.1. Selection of the Decay $B_d \rightarrow \mu^+ \nu_\mu \bar{D}^0 X$

For the performance studies and the measurement of the  $B_d$  oscillation frequency  $\Delta m_d$  a dataset of  $1 \text{ fb}^{-1}$ , collected with the DØ detector between April 2002 and October 2005, was used.  $B$  mesons were selected using their semileptonic decays  $B_d \rightarrow \mu^+ \nu_\mu \bar{D}^0 X$  and afterwards divided into two exclusive groups [95].

The  $D^*$  dataset included all  $D^*$  candidates, decaying through the decay  $D^{*-} \rightarrow \bar{D}^0 \pi^-$  into a  $\bar{D}^0$ . All remaining candidates form the  $D^0$  dataset. The  $D^*$  sample consists of 85% of  $B_d \rightarrow \mu^+ \nu_\mu D^{*-} X$  and 15% of the decay  $B^+ \rightarrow \mu^+ \nu_\mu \bar{D}^0$ , while the candidate ratios are reversed for the  $D^0$  sample. Figure 8.1 shows the invariant  $K\pi$  masses for the  $D^0$  and  $D^*$  candidates.

Events from the  $D^*$  sample were used to measure the purity of the flavor tagging and the oscillation parameter  $\Delta m_d$ . In addition, the purity was measured in the  $D^0$  sample to test the hypothesis that the flavor tagger is independent of the type of reconstructed  $B$  meson.

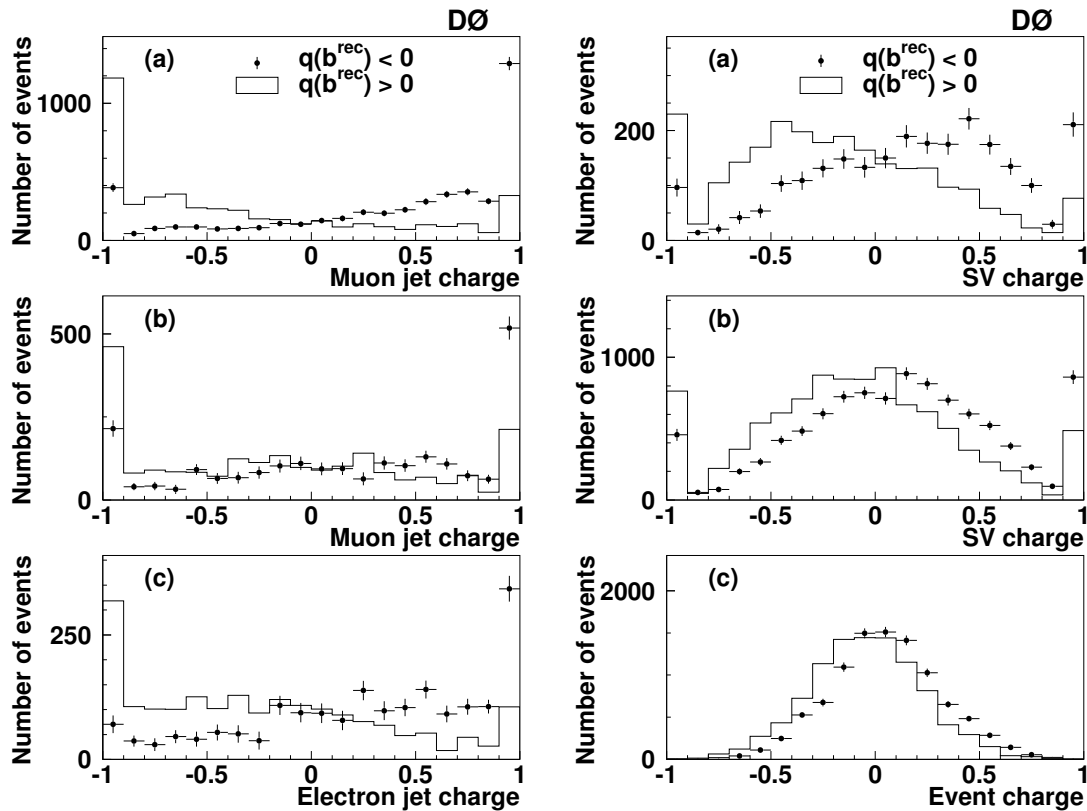
### 8.2.2. Measurement of the Tagging Performance

Figure 8.2 shows the distributions of all various tagging methods, described in Section 8.1. The distributions are obtained from data. The closer an event is to 1 (-1), the more probable the event is non-oscillated (oscillated). The upper left plot shows the best separation of oscillated and non-oscillated events. Thus, muon tagging provides the best tagging performance, despite the fact that all muons from the cascade decays ( $b \rightarrow c \rightarrow \mu X$ ) carry the same charge as the  $b$  quarks on the reconstructed side. Hence, the wrong initial state is determined and the tagging performance is reduced.

Figure 8.3 shows the combination of all tagging variables. For the combination of all opposite side tagging techniques, the tagging power is determined as [95]

$$\epsilon \mathcal{D}^2 = (2.48 \pm 0.21(\text{stat}) {}^{+0.08}_{-0.06}(\text{sys}))\%. \quad (8.13)$$





**Figure 8.2:** Normalized distributions of tagging methods [95].  $q(b^{\text{rec}})$  is the charge of the  $b$  quark from the reconstructed side. Top left: muons with three hits in the muon system. Middle left: muons with less than three hits in the muon system. Lower left: electron jet charge distribution. Top right: secondary vertex jet charge for events with an opposite side muon. Middle right: secondary vertex jet charge for events without an opposite side muon. Lower right: event jet charge.

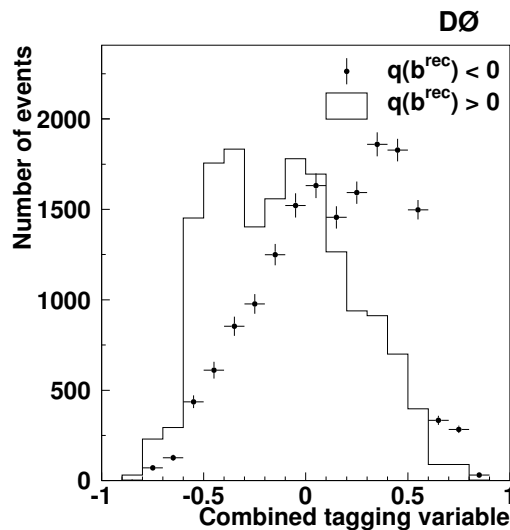


**Figure 8.3:** Distribution of the combined tagging variable  $d$  [95], which is the combination of various opposite side tagging methods and obtained by a likelihood ratio method.

**8.2.3. Measurement of the Oscillation Frequency  $\Delta m_d$** 

The mixing frequency is obtained through the flavor asymmetry

$$A = \frac{N_{\text{nos}} - N_{\text{osc}}}{N_{\text{nos}} + N_{\text{osc}}}, \quad (8.14)$$

where  $N_{\text{nos}}$  ( $N_{\text{osc}}$ ) is the number of non-oscillated (oscillated) events. An event is considered to be oscillated, if  $q(\mu) \cdot d < 0$  for the decay  $B_d \rightarrow \mu^+ \nu_\mu \bar{D}^0 X$  and non-oscillated, if  $q(\mu) \cdot d > 0$ . In the case of  $q(\mu) \cdot d = 0$  it is not possible to determine, if the event is oscillated or not. All events in the  $D^0$  and  $D^*$  samples were divided into seven groups, depending on the visible proper decay lengths. For each group the asymmetry is determined and by minimizing a  $\chi^2$  function the oscillation frequency is determined. By using events with  $|d| > 0.3$  the mixing frequency [95]

$$\Delta m_d = (0.506 \pm 0.020(\text{stat}) \pm 0.016(\text{sys})) \text{ ps}^{-1} \quad (8.15)$$

is obtained, which is in perfect agreement with the world average of  $\Delta m_d = (0.507 \pm 0.005) \text{ ps}^{-1}$  [6].

## Extraction of the Oscillation Frequency $\Delta m_s$

A precise measurement of the oscillation frequency of  $B_s$  mesons is essential to determine the matrix element  $|V_{td}|$  of the CKM matrix. This is a crucial check of the standard model, as it is described in Section 1.5. To obtain the oscillation frequency an unbinned maximum likelihood fit has been utilized in this thesis. The procedure is very similar to the measurement of the average  $B_s$  meson lifetime, as described in Chapter 7. In fact, the only difference is taking into account the information, whether an event is oscillated or not. The oscillation frequency is scanned in a range between  $0 \text{ ps}^{-1}$  and  $30 \text{ ps}^{-1}$  and the probability of an oscillation is calculated for every single event. As the theoretical prediction for the oscillation frequency is  $\Delta m_s = (18.3 \pm 1.7) \text{ ps}^{-1}$  [104] this region is sufficient to confirm or exclude a mixing frequency, as expected within the standard model. The fitting procedure is described in detail in Section 9.1. A consistency check with Monte Carlo (Section 9.2), the results for a  $\Delta m_d$  (Section 9.3) and a  $\Delta m_s$  (Section 9.4) scan are shown afterwards. Systematic uncertainties are presented in Section 9.5. Finally, the impact on the side length  $|V_{td}|/|V_{ts}|$  of the unitarity triangle is discussed.

### 9.1. Method to Extract the Oscillation Frequency $\Delta m_s$ by Using an Unbinned Likelihood Fit

The general principal of the likelihood fit is explained in Chapter 7, where the extraction of the  $B_s$  meson lifetime is described. For the fit, which aims to extract the oscillation frequency, the same input observables and parameters are used, as those employed in the lifetime fit, but tagging information is also added. The charge correlation of the pion from the signal  $B_s$  decay and the flavor tag of the opposite side  $B$  hadron is used to decide, whether an event is oscillated or not. Information on the reliability of this tag is include via the dilution, as discussed in Chapter 8. Thus, the principle of this fit is exactly the same as that used in the lifetime fit. The only difference is the determination of an oscillation and non-oscillation probability, instead of the decay probability in Chapter 7. The prediction of the oscillation probabilities is already described in Chapter 2, while the exact technical implementation is explained in Appendix C.

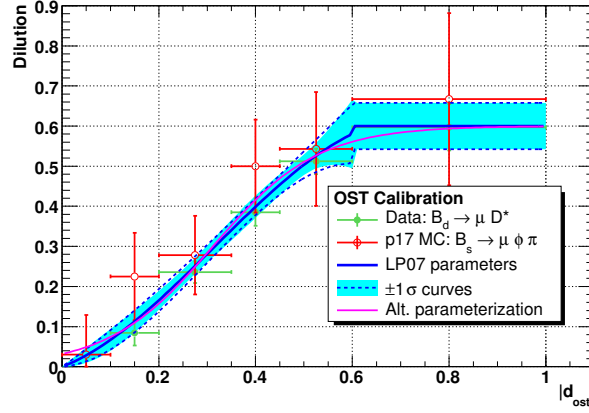


**Figure 9.1:** Dilution calibration curve [105] to determine the oscillation status. A more detailed view on the OST technique is given in Chapter 8.

Fitting parameter	$p_0$	$p_1$	$p_2$	$p_3$
Value	$0.600 \pm 0.058$	$0.457 \pm 0.385$	$2.349 \pm 1.628$	$-2.498 \pm 1.984$

**Table 9.1:** Fitting parameters for the dilution calibration curve, as obtained in [105].

Except for the dilution all other input parameters are described in detail in the lifetime measurement chapter (Chapter 7), which includes all reference distributions and how the input parameters are extracted. The dilution is predicted based on the value of the event tag variable,  $d$ , using the calibration curve shown in Figure 9.1. It is fitted [105] and parametrized with a polynomial of third order

$$|d| \leq 0.6 : p_1 \cdot |d| + p_2 \cdot |d|^2 + p_3 \cdot |d|^3 \quad (9.1)$$

$$|d| > 0.6 : p_0, \quad (9.2)$$

with the fitting parameters,  $p_0 - p_3$ , given in Table 9.1. The visible proper decay length is determined on an event-by-event basis

$$x^M = L_{xy}^B \frac{m(B_s)c}{p_T(B_s)}, \quad (9.3)$$

where  $m(B_s)$  is taken from the PDG [6], the flight length  $L_{xy}^B$  and the visible transverse momentum  $p_T(B_s)$  are taken from data. To obtain a quantity for the values of  $\Delta m_s$ , where the fitting results are confident, the distribution

$$\log \mathcal{L}_{\text{evt}} = \frac{\mathcal{L}_{\text{evt}}^{\text{OS}} + \mathcal{L}_{\text{evt}}^{\text{SS}}}{2} \quad (9.4)$$

can be plotted. It is equal to a distribution, where the charge combination of the  $\pi$  meson from the decaying  $B_s$  and the  $\mu$  from the opposite side is unknown. The range between  $0 \text{ ps}^{-1}$  and the intersection of the distribution and the loglikelihood value 1.67 is valid with a confidence level of 95%. The decay constant  $c\tau$  is set to the values measured in Chapter 7. These steps are repeated for different values of  $\Delta m_s$  within the interval  $0 \text{ ps}^{-1} < \Delta m_s < 30 \text{ ps}^{-1}$ .

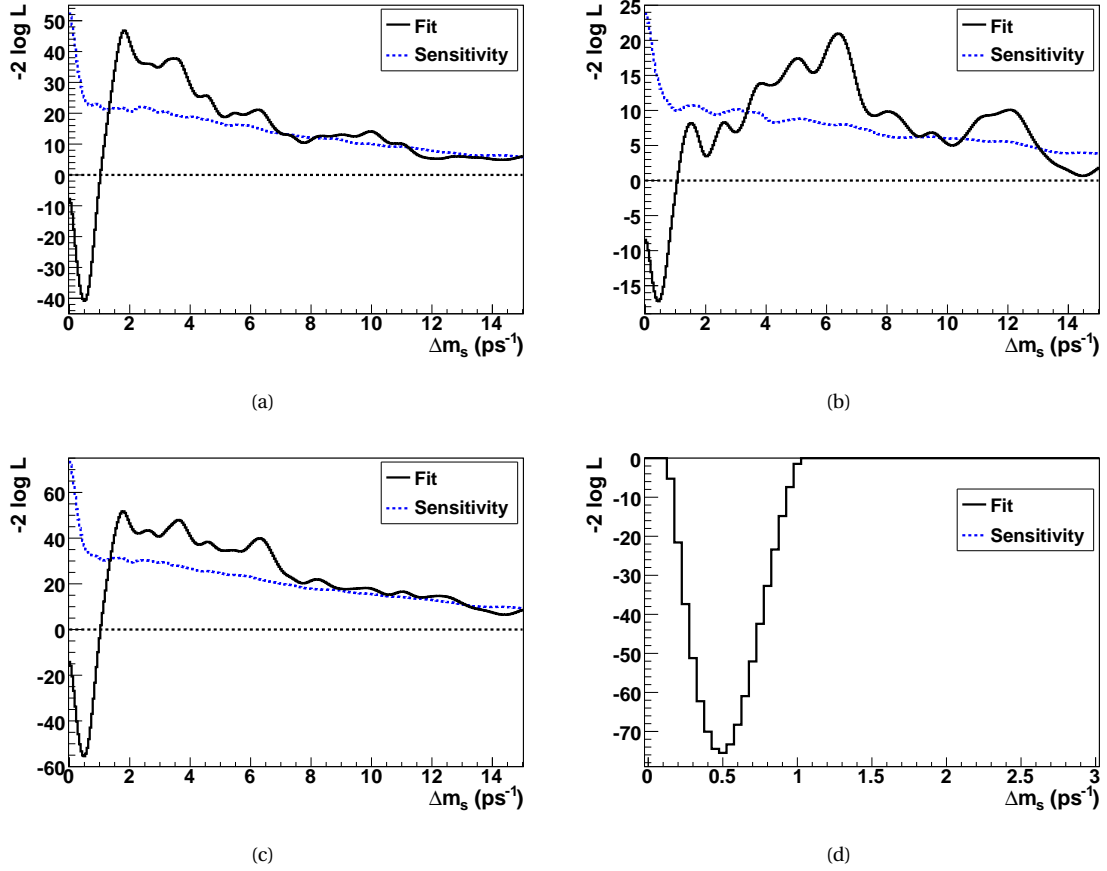


**Figure 9.2:** Results of the consistency check of the likelihood fit with  $B_d$  signal Monte Carlo. In this sample an oscillation frequency of  $\Delta m_d = 0.5 \text{ ps}^{-1}$  is implemented. The black solid line is the distribution of the fit itself, while the blue dashed line shows the sensitivity of the fit. (a) RunIIa  $B_d$  Monte Carlo sample, (b) RunIIb  $B_d$  Monte Carlo sample, (c) Combined RunIIa and RunIIb  $B_d$  Monte Carlo sample, (d) Same as (c), but zoomed into interesting region.

## 9.2. Checking the Fit with Monte Carlo Simulation

To prove the functional principle of the fit, Monte Carlo samples are used to extract the oscillation frequency and compare the result with the implemented value. For the  $B_d$  Monte Carlos a mixing frequency of  $\Delta m_d = 0.5 \text{ ps}^{-1}$  is used. All the samples as described in chapter 5 are taken into account, i.e. the fully reconstructed, as well as the partially reconstructed decays. For the likelihood fit a step size of  $0.05 \text{ ps}^{-1}$  is used. Figure 9.2 shows the obtained likelihood fits for RunIIa and RunIIb Monte Carlo separately (upper plots) and for the combination of both simulation sets, including a zoom into the interesting region (right-hand side lower plot). From the fits an oscillation frequency of

$$\Delta m_{d,\text{RunIIa-MC}} = (0.50 \pm 0.05(\text{stat})) \text{ ps}^{-1}, \quad (9.5)$$

$$\Delta m_{d,\text{RunIIb-MC}} = (0.45^{+0.10}_{-0.15}(\text{stat})) \text{ ps}^{-1}, \quad (9.6)$$

$$\Delta m_{d,\text{combined-MC}} = (0.50 \pm 0.05(\text{stat})) \text{ ps}^{-1} \quad (9.7)$$

is extracted, where most of the statistical uncertainty is given by the step size. As the result of the fit is in perfect agreement with the implemented value, the fit can be considered as working. The same check is performed for  $B_s$  Monte Carlo with an implemented oscillation frequency of

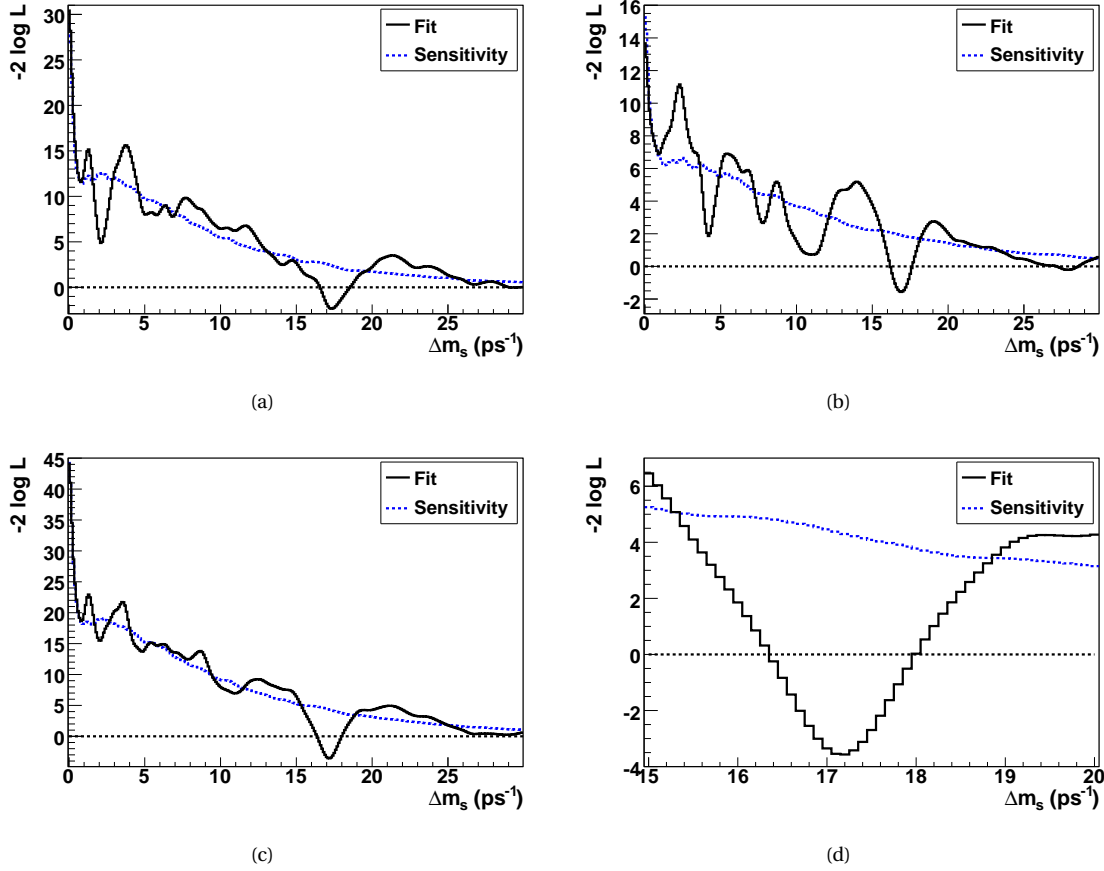


**Figure 9.3:** Results of the consistency check of the likelihood fit with  $B_s$  signal Monte Carlo. In this sample an oscillation frequency of  $\Delta m_s = 17.11 \text{ ps}^{-1}$  is implemented. The black solid line is the distribution of the fit itself, while the blue dashed line shows the sensitivity of the fit. (a) RunIIa  $B_s$  Monte Carlo sample, (b) RunIIb  $B_s$  Monte Carlo sample, (c) Combined RunIIa and RunIIb  $B_s$  Monte Carlo sample, (d) Same as (c), but zoomed to interesting region.

$\Delta m_s = 17.11 \text{ ps}^{-1}$ . In this case the step size is set to  $0.1 \text{ ps}^{-1}$ . The obtained distributions are shown in Figure 9.3. The oscillation frequency in case of the  $B_s$  Monte Carlo sample can be extracted as

$$\Delta m_{s,\text{RunIIa-MC}} = (17.3^{+0.6}_{-0.5}(\text{stat})) \text{ ps}^{-1}, \quad (9.8)$$

$$\Delta m_{s,\text{RunIIb-MC}} = (16.9^{+0.6}_{-0.5}(\text{stat})) \text{ ps}^{-1}, \quad (9.9)$$

$$\Delta m_{s,\text{combined-MC}} = (17.2^{+0.6}_{-0.5}(\text{stat})) \text{ ps}^{-1}. \quad (9.10)$$

Like the results for the  $B_d$  Monte Carlos, this is in perfect agreement with the implemented mixing frequency. This again validates the fitting procedure and thus, it can be used to extract a result from the data samples.

### 9.3. Measurement of $\Delta m_d$

After the likelihood fit was verified with Monte Carlo events, the oscillation frequency for  $B_d$  mesons was determined. The range between  $0 \text{ ps}^{-1}$  and  $20 \text{ ps}^{-1}$  was scanned with a step size of  $0.05 \text{ ps}^{-1}$ . This determination is another crucial cross-check of the analysis chain, as these events occur with

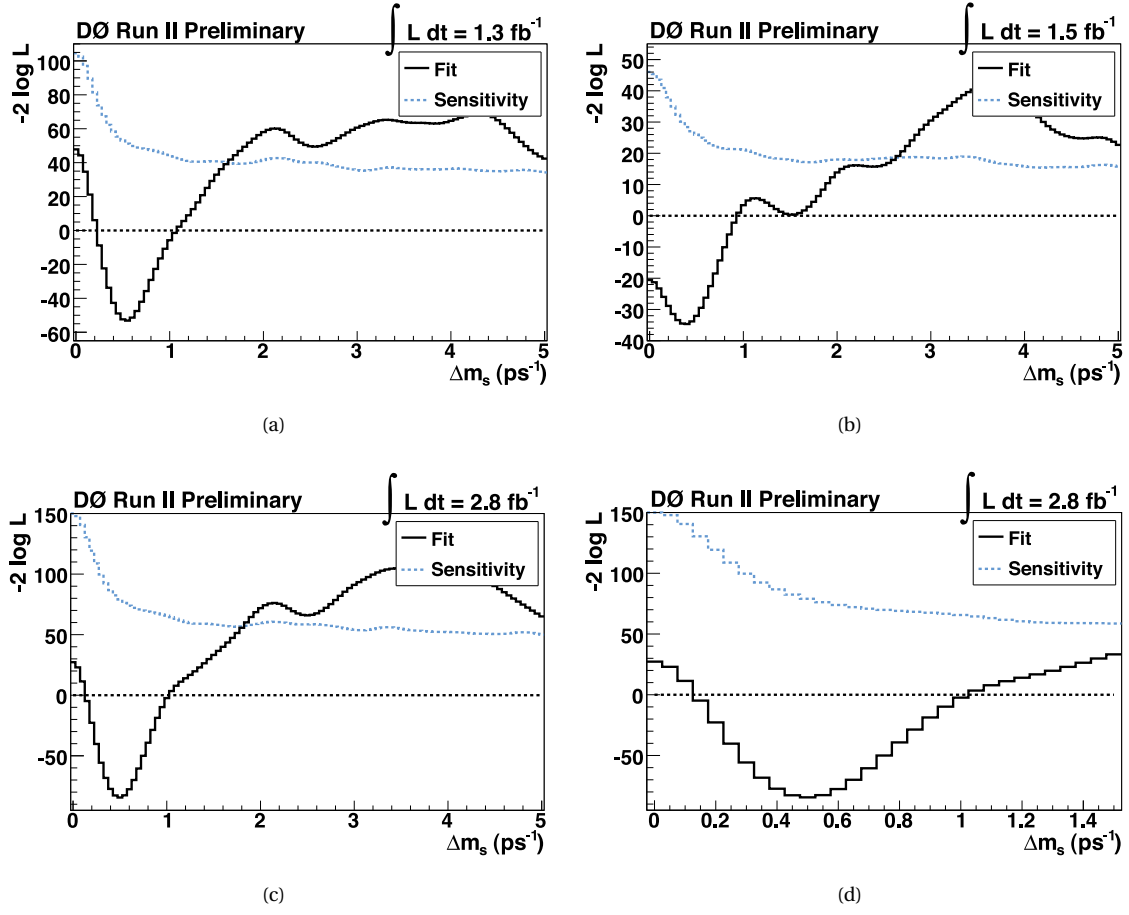


**Figure 9.4:** Results of the likelihood fit with  $B_d$  data. The black solid line is the distribution of the fit itself, while the blue dashed line shows the significance of the fit. (a) RunIIa data, (b) RunIIb data, (c) Full data set, (d) Full data sample and zoomed to interesting region.

higher statistics and precise measurements already exist from BaBar and Belle [6]. The results of the likelihood fit are shown in Figure 9.4. From these plots the oscillation frequency was extracted as

$$\Delta m_{d,\text{RunIIa}} = (0.55 \pm 0.05(\text{stat})) \text{ ps}^{-1}, \quad (9.11)$$

$$\Delta m_{d,\text{RunIIb}} = (0.40 \pm 0.05(\text{stat})) \text{ ps}^{-1}, \quad (9.12)$$

$$\Delta m_{d,\text{combined}} = (0.50 \pm 0.05(\text{stat})) \text{ ps}^{-1}. \quad (9.13)$$

As for the lifetime fits, the oscillation frequency is a little bit too low for RunIIb data. This effect is still not understood completely. It may be caused by a different background composition due to overlayed events. However, the RunIIa data is in agreement with the world-average of  $\Delta m_d = (0.507 \pm 0.005) \text{ ps}^{-1}$  [6] and the combination of both datasets results in a reliable measurement of the oscillation frequency.

## 9.4. Measurement of $\Delta m_s$

The analysis chain was tested thoroughly with Monte Carlo events and the higher statistic sample of hadronic decays of  $B_d$  mesons. Both measurements lead to reliable results. Hence, the same

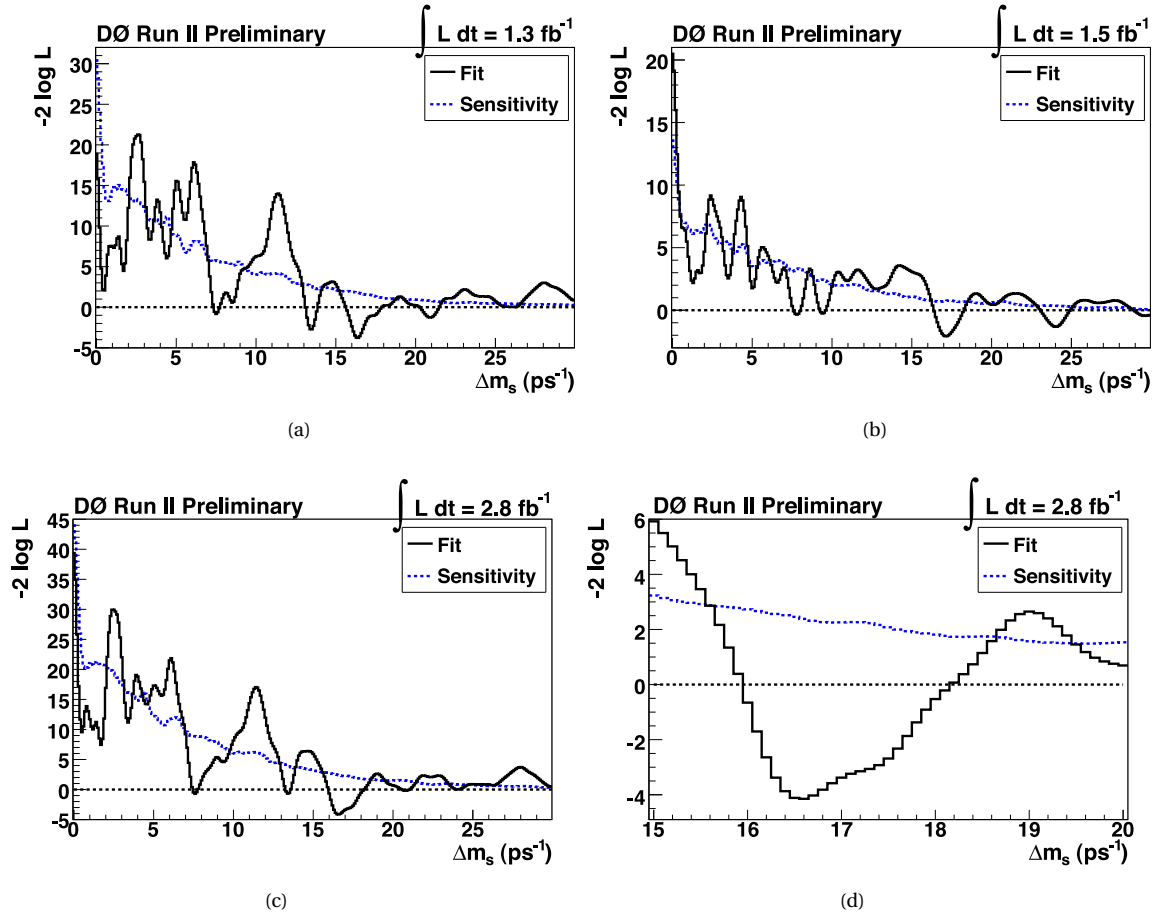


**Figure 9.5:** Results of the likelihood fit with  $B_s$  data. The black solid line is the distribution of the fit itself, while the blue dashed line shows the significance of the fit. (a) RunIIa data, (b) RunIIb data, (c) Full data set, (d) Full data sample and zoomed to interesting region.

procedure was applied to the selected  $B_s$  dataset. As the number of candidates is significantly lower than for the measurement of  $B_d$  oscillations, the statistical uncertainties are expected to be higher. The result of the fit is shown in Figure 9.5 and the mixing frequency of  $B_s$  mesons in the golden mode  $B_s \rightarrow \pi D_s(\phi\pi)X$  was determined as

$$\Delta m_{s,\text{RunIIa}} = (16.5^{+0.2}_{-0.3}(\text{stat})) \text{ ps}^{-1}, \quad (9.14)$$

$$\Delta m_{s,\text{RunIIb}} = (17.1^{+0.7}_{-0.4}(\text{stat})) \text{ ps}^{-1}, \quad (9.15)$$

$$\Delta m_{s,\text{combined}} = (16.6^{+0.5}_{-0.4}(\text{stat})) \text{ ps}^{-1}. \quad (9.16)$$

However, the RunIIa result has to be handled with care: from the first point of view, the statistical uncertainty seems to be low, compared to the almost same amount of events from RunIIb data. However, there is another minimum close-by (at  $\Delta m_s \approx 13.5 \text{ ps}^{-1}$ ), which has almost the same significance. Thus, the significance of the RunIIa data is low, compared to the significance of RunIIb.



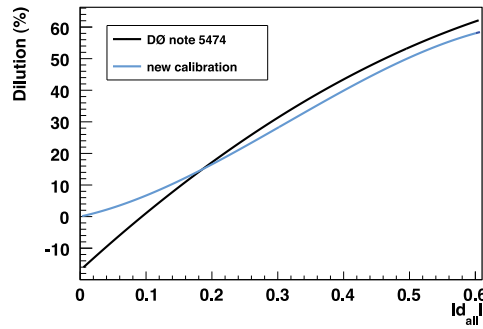


**Figure 9.6:** Comparison of the old [106], [107] and new dilution calibration curve.

Systematic	$B_s$			$B_d$		
	RunIIa	RunIIb	combined	RunIIa	RunIIb	combined
Efficiency	$< \pm 0.1$	$< \pm 0.1$	$< \pm 0.1$	$< \pm 0.05$	$< \pm 0.05$	$< \pm 0.05$
Background	$< \pm 0.1$	$< \pm 0.1$	$< \pm 0.1$	$< \pm 0.05$	$< \pm 0.05$	$< \pm 0.05$
k-Factor	$+0.3$ $-0.4$	$+0.4$ $-0.3$	$+0.4$ $-0.3$	$< \pm 0.05$	$< \pm 0.05$	$< \pm 0.05$
Resolution	$< +0.1$ $-0.1$	$< +0.1$ $-0.1$	$< \pm 0.1$	$< \pm 0.05$	$< \pm 0.05$	$< \pm 0.05$
Dilution	$< \pm 0.1$	$\pm 0.1$	$< \pm 0.1$	$< \pm 0.05$	$< \pm 0.05$	$< \pm 0.05$
Lifetime	$< \pm 0.1$	$< \pm 0.1$	$< \pm 0.1$	$< \pm 0.05$	$< \pm 0.05$	$< \pm 0.05$

**Table 9.2:** Uncertainties of the  $\Delta m_{d,s}$  fit. The deviation is given in  $\text{ps}^{-1}$ .

## 9.5. Systematic Uncertainties

The same uncertainties as for the lifetime measurement as described in Section 7.4.3 were taken into account (background variation,  $k$ -factor uncertainty and changing the resolution width). Additionally systematic checks for the dilution and lifetime are performed. As stated in Equation 2.5 the lifetime – whose extraction is shown in Chapter 7 – is directly correlated with the mixing probability. As this measurement has an uncertainty itself, the lifetime was varied within the statistical error of the lifetime measurement to take this into account.

The dilution is an important variable when determining the mixing state. Hence, the calibration may influence the oscillation frequency measurement. The uncertainty of the dilution was determined by using an older calibration curve, which has been used for the Lepton-Photon 2007 conference results [106], [107]. The comparison between both curves is shown in Figure 9.6.

Table 9.2 gives an overview of all the performed systematic checks and the impact on the measurement of the oscillation frequencies  $\Delta m_s$  and  $\Delta m_d$ . It is clearly visible, that the highest systematic uncertainty arises from the determination of the  $k$ -factor. It is limited by the amount of available Monte Carlo, as already discussed in Chapter 7. The resolution has only a minor impact on the measurement. The other systematic checks are negligible. They are smaller than the scanning interval of  $0.1 \text{ ps}^{-1}$  ( $0.05 \text{ ps}^{-1}$  in the case of  $B_d$  mixing). The shift of the amplitude caused by the systematic uncertainties can be found in Table 9.3 for  $\Delta m_d$  and Table 9.4 for  $\Delta m_s$ . It is in perfect agreement with the results of the likelihood fit.

## 9.6. Final Results for the Measurement of $\Delta m_d$ and $\Delta m_s$

By taking the systematical uncertainties of the previous sections into account, the final results of the mixing frequency of  $B_d$  mesons in the mode  $B_d \rightarrow D^{*-}\pi^+$  are

$$\Delta m_{d,\text{RunIIa}} = (0.55 \pm 0.05(\text{stat}) \pm (< 0.2)(\text{sys})) \text{ps}^{-1}, \quad (9.17)$$

$$\Delta m_{d,\text{RunIIb}} = (0.40 \pm 0.05(\text{stat}) \pm (< 0.2)(\text{sys})) \text{ps}^{-1}, \quad (9.18)$$

$$\Delta m_{d,\text{combined}} = (0.50 \pm 0.05(\text{stat}) \pm (< 0.2)(\text{sys})) \text{ps}^{-1}. \quad (9.19)$$

Additionally an amplitude scan for this decay was performed. The distributions obtained are shown in Figure 9.7, including the systematical and statistical uncertainties for all oscillation frequencies. The results for the region near the amplitude peak are shown in Table 9.3.

For the  $B_s$  mixing frequency the results, including the systematical uncertainties are

$$\Delta m_{s,\text{RunIIa}} = (16.5^{+0.2}_{-0.3}(\text{stat}) \pm (< 0.5)(\text{sys})) \text{ps}^{-1}, \quad (9.20)$$

$$\Delta m_{s,\text{RunIIb}} = (17.1^{+0.7}_{-0.4}(\text{stat})^{+(<0.5)}_{-(<0.4)}(\text{sys})) \text{ps}^{-1}, \quad (9.21)$$

$$\Delta m_{s,\text{combined}} = (16.6^{+0.5}_{-0.4}(\text{stat})^{+(<0.5)}_{-(<0.4)}(\text{sys})) \text{ps}^{-1}. \quad (9.22)$$

For this data an amplitude scan was also performed, as shown in Figure 9.8 and summarized in Table 9.4.

As the Tevatron is the only place, where these kind of oscillations can be observed, only measurements of the CDF and DØ collaborations exist so far. The  $\Delta m_s$  results presented here are lower than those measured before by the DØ collaboration:  $\Delta m_s = (18.53 \pm 0.93(\text{stat}) \pm 0.30(\text{sys})) \text{ps}^{-1}$  [106], [107]. However, these results are still limited by statistics and are marginally compatible with the previous measurements. As the CDF measurement of  $\Delta m_s = (17.77 \pm 0.10(\text{stat}) \pm 0.07(\text{sys})) \text{ps}^{-1}$  [108] is lower than the DØ measurement, the results of this analysis are in better agreement with the CDF results, which are also dominated by the golden mode  $B_s \rightarrow \pi D_s(\phi\pi)X$ .

## 9.7. Impact on $|V_{td}|/|V_{ts}|$

A crucial test of the standard model is to over-constrain the unitarity triangle. As already described, the least known parameter is the side length  $|V_{td}|$ . It is accessible by obtaining the oscillation frequency of  $B_d$  and  $B_s$  mesons. The exact determination of the CKM element ratio from measurements of  $\Delta m_s$  and  $\Delta m_d$  is discussed in Section 2.5. It is given by

$$\frac{|V_{td}|}{|V_{ts}|} = \xi \sqrt{\frac{\Delta m_d}{\Delta m_s} \frac{M_{B_s}}{M_{B_d}}}, \quad (9.23)$$

where  $\xi = 1.210^{+0.047}_{-0.035}$  [11] is a hadronic correction term,  $\Delta m_s$  and  $\Delta m_d$  are the mixing frequencies of  $B_s$  and  $B_d$  mesons and  $M_{B_s}$ ,  $M_{B_d}$  are their masses. Using the results for  $\Delta m_s$  from the hadronic mode  $B_s \rightarrow \pi D_s(\phi\pi)X$  presented here and the world-averages for  $\Delta m_d$ ,  $M_{B_s}$  and  $M_{B_d}$ , the side length ratio is determined as

$$|V_{td}|/|V_{ts}| = 0.213^{+0.004}_{-0.003}(\text{exp}) \pm 0.008(\text{theor}). \quad (9.24)$$

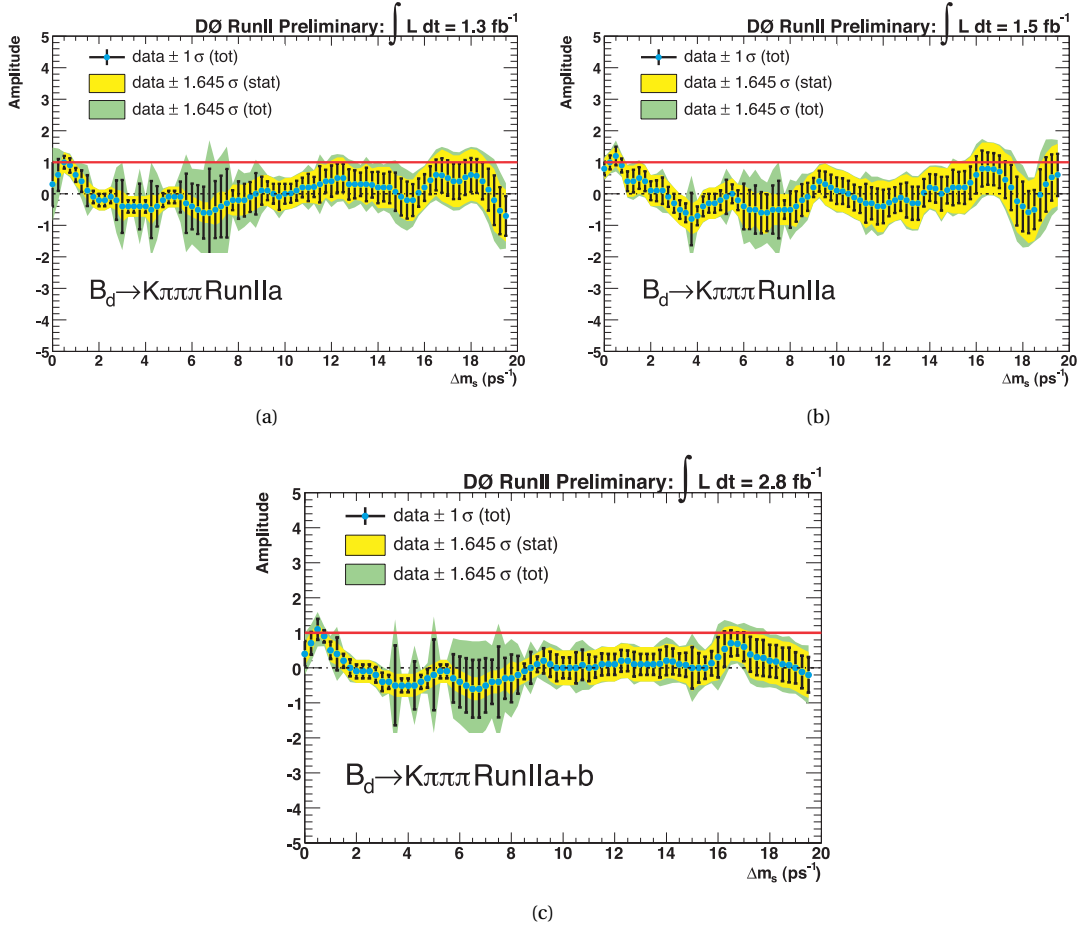


**Figure 9.7:** Amplitude scans for the hadronic  $B_d$  decay mode. (a) RunIIa data, (b) RunIIb data, (c) Combination of both datasets.

$\Delta m_d (\text{ps}^{-1})$	Ampl.	stat.	bkg (off)	bkg (sl)	dil	k-fac	res.	eff.	$\tau_{B_s}$	syst.	tot.
0.00	0.40	0.20	+0.00	+0.00	-0.30	+0.00	+0.00	+0.00	+0.00	0.30	0.36
0.25	0.70	0.20	-0.15	+0.00	-0.15	-0.15	+0.00	+0.00	+0.00	0.26	0.33
0.50	1.10	0.10	-0.20	+0.00	-0.20	+0.00	+0.00	+0.00	+0.00	0.28	0.30
0.75	0.90	0.10	+0.00	+0.10	+0.00	+0.10	+0.00	+0.00	+0.00	0.14	0.17
1.00	0.50	0.20	+0.00	+0.00	+0.00	-0.15	+0.00	+0.00	+0.00	0.15	0.25
1.25	0.40	0.20	-0.30	+0.00	-0.30	+0.00	+0.00	+0.00	+0.00	0.42	0.47
1.50	0.20	0.20	+0.00	+0.00	+0.00	+0.00	+0.00	+0.00	+0.00	0.00	0.20

**Table 9.3:** Uncertainties of the  $\Delta m_d$  amplitude scan in a region near the amplitude peak. This table shows the scanned  $\Delta m_d$  value and its determined amplitude in the two left hand-side columns. These values are followed by the statistical uncertainty and the studied uncertainty sources: an offset of the background distribution, a variation of the slope of the background, a different dilution calibration curve, a shift in the k-Factor distributions, a variation of the resolution, the modelling of the efficiency and a variation of the lifetime. All contributions are taken into account for the systematical uncertainty and given in absolute values. The most right hand-side column shows the total variation of the amplitude, caused by statistical and systematical uncertainties.

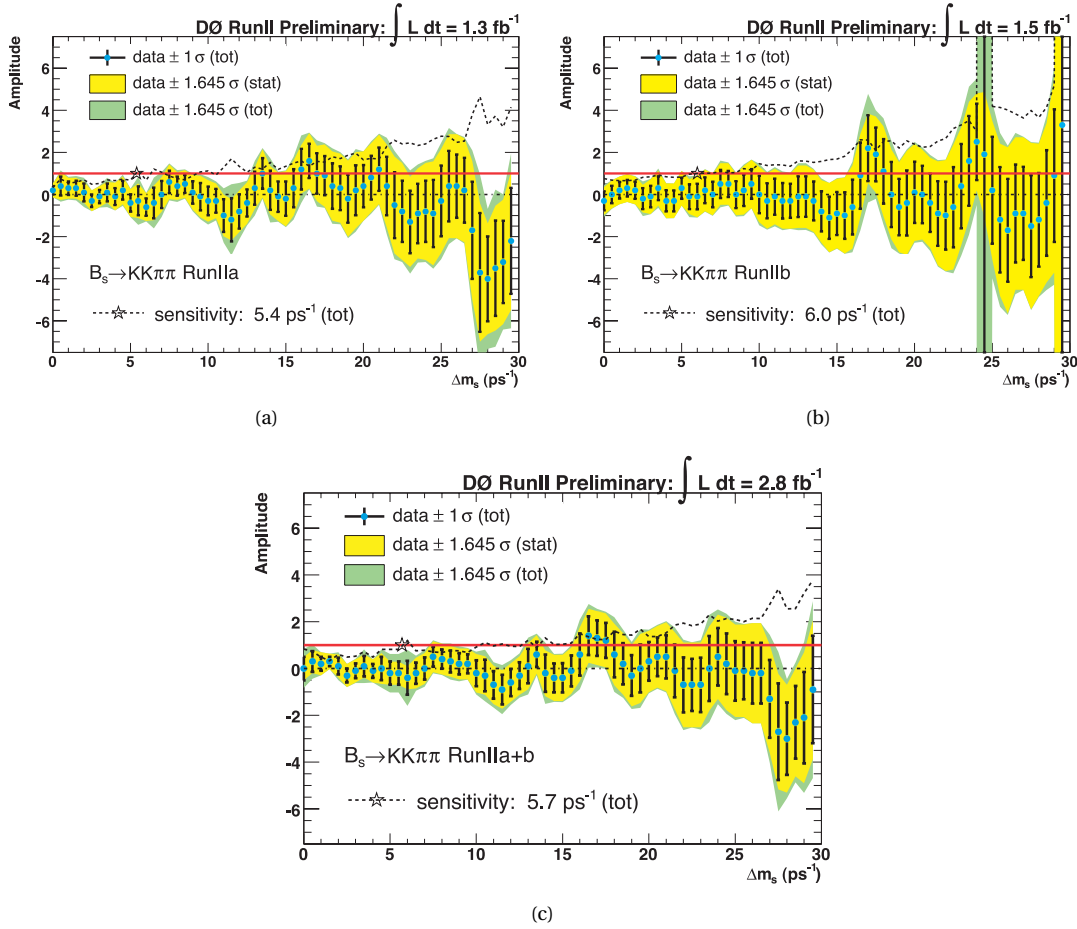


**Figure 9.8:** Amplitude scans for the hadronic  $B_s$  decay mode. (a) RunIIa data, (b) RunIIb data, (c) Combination of both datasets.

$\Delta m_s(\text{ps}^{-1})$	Ampl.	stat.	bkg (off)	bkg (sl)	dil	k-fac	res.	eff.	$\tau_{B_s}$	syst.	tot.
15.00	-0.40	0.60	+0.00	+0.00	+0.00	+0.13	-0.13	+0.00	+0.00	0.19	0.63
15.50	-0.10	0.60	+0.00	+0.18	+0.00	-0.20	-0.08	+0.00	+0.00	0.28	0.66
16.00	0.60	0.70	+0.00	+0.00	-0.06	-0.56	-0.11	+0.00	+0.00	0.57	0.90
16.50	1.40	0.70	-0.10	+0.00	-0.04	-0.40	-0.14	+0.00	+0.00	0.44	0.83
17.00	1.30	0.70	-0.10	+0.00	-0.10	+0.20	-0.16	+0.00	+0.00	0.29	0.76
17.50	1.20	0.70	-0.13	-0.03	-0.10	+0.10	-0.17	+0.00	+0.00	0.26	0.75
18.00	0.60	0.80	+0.00	+0.10	+0.00	+0.50	-0.20	+0.05	+0.05	0.55	0.97
18.50	0.20	0.80	-0.10	+0.00	+0.00	+0.30	-0.20	+0.00	+0.00	0.37	0.88
19.00	-0.30	0.80	+0.00	+0.00	+0.00	+0.30	-0.16	+0.00	+0.00	0.34	0.87
19.50	0.00	0.90	+0.00	+0.00	-0.11	-0.41	-0.22	+0.00	+0.00	0.48	1.02
20.00	0.30	0.80	+0.00	+0.00	+0.00	-0.11	-0.19	+0.00	+0.00	0.22	0.83
20.50	0.50	0.80	+0.00	+0.00	+0.00	-0.14	-0.16	+0.00	+0.00	0.21	0.83
21.00	0.50	0.90	-0.056	+0.00	-0.06	-0.06	-0.21	+0.00	+0.00	0.23	0.93
21.50	-0.10	1.00	+0.00	+0.01	-0.11	+0.49	-0.12	+0.00	+0.00	0.52	1.13
22.00	-0.70	1.10	-0.05	+0.00	-0.15	+0.35	-0.16	+0.00	+0.00	0.42	1.18
22.50	-0.70	1.10	+0.00	+0.00	-0.10	+0.00	-0.11	+0.00	+0.00	0.15	1.11
23.00	-0.70	1.10	-0.15	+0.00	-0.25	+0.05	-0.21	+0.00	+0.00	0.37	1.16

**Table 9.4:** Uncertainties of the  $\Delta m_s$  amplitude scan in a region near the amplitude peak. An explanation of the variables shown can be found in Table 9.3.

## Summary and Outlook

The standard model of particle physics is a theory, describing three out of four fundamental forces. In this model the CKM matrix describes the relation between weak and flavor eigenstates of the quarks. One of the least known matrix elements is  $|V_{td}| = (7.4 \pm 0.8) \cdot 10^{-3}$  [6]. It is accessible by studying the transition of neutral  $B$  mesons to their anti-particles and vice versa, a behavior which is also known as mixing [7]. It is caused by the mass difference  $\Delta m = m_H - m_L$  of the two mass eigenstates  $|B_H\rangle = p|B^0\rangle - q|\bar{B}^0\rangle$  and  $|B_L\rangle = p|B^0\rangle + q|\bar{B}^0\rangle$ , where  $B^0$  and  $\bar{B}^0$  are weak (flavor) eigenstates, and  $p, q$  are constants.. Since observation of flavor oscillations in the  $B_d$  system by the ARGUS collaboration [8] this topic has been studied intensively and was well measured at the  $B$ -factories BaBar and Belle. Theoretically the relation between  $\Delta m_d$  and  $|V_{td}|$  is given by [11]:

$$\Delta m_d = \text{const.} \times f_{B_d}^2 B_{B_d} |V_{tb}^* V_{td}|^2. \quad (10.1)$$

Nonperturbative QCD effects are contained in  $f_{B_d}^2 B_{B_d}$ , where  $f_{B_d}^2$  is the  $B_d$  meson decay constant and  $B_{B_d}$  is the  $B_d$  meson bag parameter. As there are large uncertainties in the order of 20% on these hadronic correction terms, the determination of  $|V_{td}|$  is not trivial. By measuring the mass differences  $\Delta m_d$  and  $\Delta m_s$  and calculating their ratio most of the uncertainties cancel out:

$$\frac{\Delta m_s}{\Delta m_d} = \frac{m_{B_s}}{m_{B_d}} \xi^2 \frac{|V_{ts}|^2}{|V_{td}|^2}, \quad \text{with} \quad \xi^2 = \frac{f_{B_s}^2 B_{B_s}}{f_{B_d}^2 B_{B_d}} \quad (10.2)$$

where  $\xi = 1.210_{-0.035}^{+0.047}$  has uncertainties [11] of approximately 4%. The B-factories operate on the  $\Upsilon(4s)$  resonance, so the production of  $B_s \bar{B}_s$  pairs is not possible, as  $m(\Upsilon(4s)) \leq m(B_s) + m(\bar{B}_s)$ . Furthermore, the oscillation frequency of  $B_s$  mesons is about 20 times faster than for  $B_d$  mesons. To observe oscillations with the same detector resolution, the energy of the  $B_s$  mesons has to be 20 times higher to achieve the same oscillation length in the lab frame of the detector. Thus, the Tevatron (providing  $p\bar{p}$  collisions at  $\sqrt{s}=1.96$  TeV) is currently the only place, where  $B_s$  oscillations can be studied. DØ was the first experiment, which published an upper limit for the oscillation frequency  $\Delta m_s$ . It was based on the semimuonic channel  $B_s \rightarrow \mu \nu_\mu D_s(\phi\pi)$  [54]. Shortly after, the CDF collaboration confirmed this result and was able to give a  $5\sigma$  measurement [108]. The big improvement was the utilization of the hadronic mode  $B_s \rightarrow \pi D_s(\phi\pi) X$ , which is also known as the “golden mode”. No neutrinos, which are not detectable, are involved in this decay. Hence, the decay is fully reconstructable and has less uncertainties.

However, this channel is very challenging at the DØ experiment. Contrary to the CDF experiment it is not possible to trigger efficiently on displaced track vertices from low  $p_T$  objects (the STT allows a displaced vertex trigger for high  $p_T$ ), which occur due to the  $B_s$  meson lifetime. Furthermore, the momentum resolution of the DØ detector is limited by the lever arm. Hence, it is not possible to select an exclusive sample of golden mode decays,  $B_s \rightarrow \pi D_s(\phi\pi)X$ , as it is not possible to separate  $B_s \rightarrow \pi D_s$  from partially reconstructed decays,  $B_s \rightarrow \pi D_s(\phi\pi)X$ . Thus, to trigger on these decays is only possible by identifying a muon from a decay of the other  $B$  hadron in the event (opposite side). The combined requirements of a semimuonic  $B$  decay in addition to the low branching ratio signal decay ( $B_s \rightarrow \pi D_s(\phi\pi)X$ ) results in a small number of selected signal events and a large background. Extensive trigger studies were necessary to get the best possible yield of decays and consumed a large fraction during this thesis. Furthermore, for the selection, detailed Monte Carlo studies were required done in the context of this analysis.

The first selection of the hadronic decay mode  $B_s \rightarrow \pi D_s(\phi\pi)X$  at DØ to measure the oscillation frequency  $\Delta m_s$  and to determine the side length  $|V_{td}|/|V_{ts}|$  was presented. The results obtained supersede the analysis, which was already presented at Lepton-Photon 2007 [106], [107]. Compared to the 2007 results, the improvements are

- utilizing the complete dataset until a shutdown in 2007, i.e. the dataset has increased from  $\int \mathcal{L} dt = 2.5 \text{ fb}^{-1}$  to  $\int \mathcal{L} dt = 2.8 \text{ fb}^{-1}$ ;
- a likelihood selection, tuned to RunIIb data: In 2007 a slightly adapted likelihood selection from the semimuonic mode [54] was used. For this analysis the input variable distributions were determined and the selection was tuned for RunIIb data, resulting in a higher yield of  $B_s$  candidates;
- complete integration of the hadronic  $B_d$  decay mode [87], [88];
- more accurate determination of the input variables for RunIIb, due to availability of Monte Carlo samples for this run period;
- re-writing of the likelihood fit code to extract the oscillation frequencies;
- extraction of the  $B_s$  and  $B_d$  lifetimes to prove the concept of the likelihood fit code;
- utilizing the event-by-event scaling factor for RunIIb data, which was available for RunIIa data only in 2007.

The results obtained

$$\Delta m_s = (16.6_{-0.4}^{+0.5}(\text{stat})_{-(<0.4)}^{+(<0.5)}(\text{sys})) \text{ ps}^{-1}, \quad (10.3)$$

$$|V_{td}|/|V_{ts}| = 0.213_{-0.003}^{+0.004}(\text{exp})_{-0.006}^{+0.008}(\text{theor}) \quad (10.4)$$

with a significance of  $2.5\sigma$  are compatible with previous DØ measurements and within  $1.5\sigma$  with a precise measurement of the CDF collaboration

$$\Delta m_s = (18.53 \pm 0.93(\text{stat}) \pm 0.30(\text{sys})) \text{ ps}^{-1} \quad (\text{DØ}), \quad (10.5)$$

$$\Delta m_s = (17.77 \pm 0.10(\text{stat}) \pm 0.07(\text{sys})) \text{ ps}^{-1} \quad (\text{CDF}). \quad (10.6)$$

These results are illustrated in Figure 10.1. As no world-average exists so far, a personal world-average was calculated from the DØ and CDF measurement (Equations 10.5, 10.6) as

$$\Delta m_s = (17.78 \pm 0.1(\text{stat}) \pm 0.07(\text{sys})) \text{ ps}^{-1}, \quad (10.7)$$

$$|V_{td}|/|V_{ts}| = 0.206 \pm 0.0007(\text{exp})_{-0.006}^{+0.008}(\text{theor}). \quad (10.8)$$

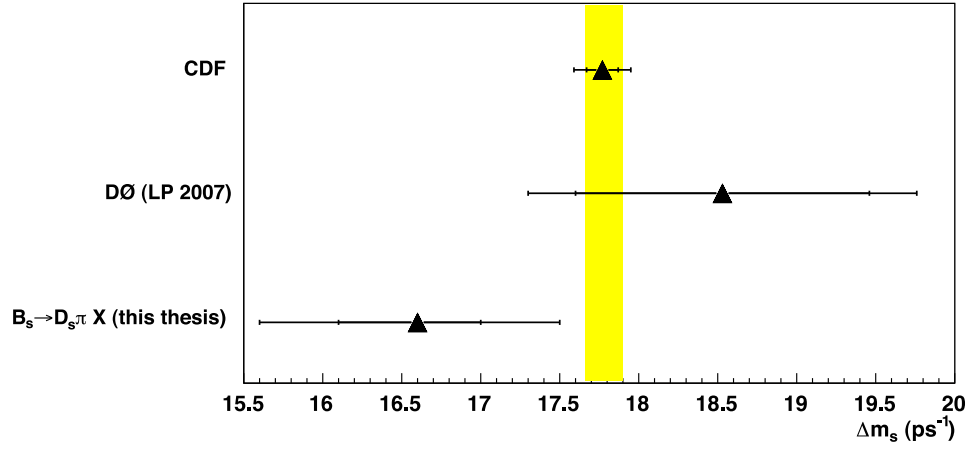


**Figure 10.1:** Comparison of the obtained  $\Delta m_s$  results with existing measurements, including a precise measurement of the CDF RunII collaboration [108], the DØ conference results from Lepton-Photon 2007 [106], [107] and the hadronic decay mode  $B_s \rightarrow \pi D_s(\phi\pi)X$ , presented in this thesis.

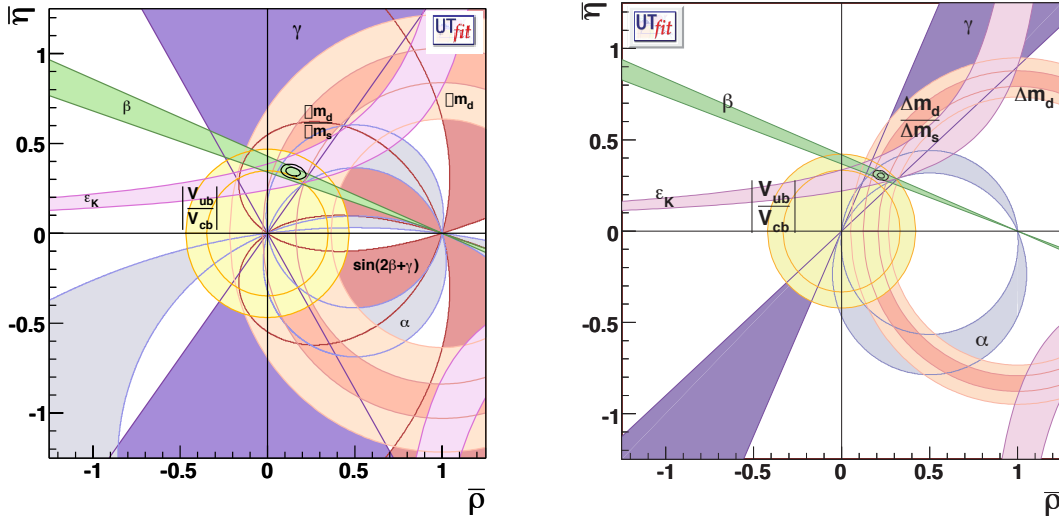


**Figure 10.2:** Evolution of the unitarity triangle as predicted by the UFit collaboration [109]. Left: Status of today. Right: As it might look like with  $10 \text{ fb}^{-1}$  data from LHC [110].

This world-average is shown as yellow band, while the different measurements are shown as black lines. Furthermore, the measurements are consistent with the SM expectations of  $\Delta m_s = (18.3 \pm 1.7) \text{ ps}^{-1}$  [104]. No hints for new physics, which could explain the existence of dark matter or matter-anti-matter asymmetry, are observed. However, the  $B$  physics program at DØ still offers fields for the observation of new physics in rare decays like  $B_s \rightarrow \mu\mu$  or  $B_s \rightarrow J/\Psi\phi$ . The latter decay is part of the squashed unitarity triangle, where the window to new physics is still open widely.

Improvements are also possible for this analysis:

- In the meantime a dataset of more than  $5 \text{ fb}^{-1}$  is available. Until the complete shutdown of the Tevatron about  $8\text{-}9 \text{ fb}^{-1}$  are planned. Right now it is not possible to easily extend the analysis to a higher dataset, as the event-by-event scaling factor is not available for more recent data.

- Higher Monte Carlo statistics would allow to determine the input variables more accurately. Some parts of a mechanism to use Monte Carlo samples at generator level are already implemented. About 10 million events at generator level are already produced, allowing to determine the input variables like the  $k$ -Factor with an accuracy of 3% [111], compared to a full Monte Carlo sample.
- The background modeling is not fully understood. Further studies may also increase the significance of this measurement.

Additionally, the LHC [27] is going to start its operation this year. The ATLAS [112] and CMS [113] experiments offer a similar spectra of  $B$  physics program, like DØ and CDF. Furthermore, with the LHC-b collaboration [114] one experiment at the LHC is focussed on observations and precise measurements within  $B$  physics. Figure 10.2 shows the prediction of the evolution of the unitarity triangle with a dataset of  $10\text{fb}^{-1}$  taken with the LHC-b detector. As already precise measurements for the angle  $\sin 2\beta$  exist [115], there will be no big improvement through measurements at LHC here. The tighter constraints on the side length  $|V_{td}|/|V_{ts}|$  are dominated by more accurate lattice QCD calculations and only a small contribution can be credited to LHC-b. However, another big improvement is expected in the measurement of the angle  $\gamma$ , which is accessible through the decay  $B^0 \rightarrow DK^{*0}$  [116]. It is expected, that this decay will allow to drop the current sensitivity from  $\Delta\gamma = \pm 4.2^\circ$  to  $\Delta\gamma = \pm 0.38^\circ$  [117].

The first selection of the “golden” mode  $B_s \rightarrow \pi D_s(\phi\pi)X$  has been presented in this analysis. It is fully reconstructable and thus, has less uncertainties than the semimuonic decay channels. The measurement of the  $B_s$  oscillation frequency is consistent with the SM predictions and does not offer a hint for new physics. However, the  $B$  physics sector still offers a rich spectra of interesting topics and the window to observe new physics is still open widely in the measurement of the “squashed unitarity triangle”.



## Muon Trigger Qualities

### A.1. Level-1 Muon Qualities

- Forward:
  - loose: A-layer centroid + A-layer pixel hit  $|\eta| < 1.6$
  - tight: loose + B-layer centroid + B-layer pixel
- Central:
  - loose: octants 0-4, 7: A-layer centroid +  $A\phi$ -hit
  - tight: either loose + C-layer + CMSC hit  
or loose + B-layer centroid + A- or B-layer SC

### A.2. Level-2 Muon Qualities

#### A.2.1. Quality for Stubs

##### CENTRAL

For A-stubs: the following conditions are examined:

- (a) 2 PDT hits (in different desks) with valid hit-pattern in LUT
- (b) Drift times satisfy track residual < tolerance (value TBA) for 3-hit patterns
- (c) Associated A-layer scintillator hit

Q=1: (a)

Q=2: (a).AND.( (b).OR.(c) )

Q=3: (a).AND.(b).AND.(c)

For BC-stubs: the following conditions are examined:

- (a) 2 PDT hits with valid hit-pattern in LUT (they may be hits in single layer)
- (b) At least one hit in each of B, C layers

(c) Associated cosmic cap scintillator hit

Q=1: (a)

Q=2: (a).AND.( (b).OR.(c) )

Q=3: (a).AND.(b).AND.(c)

## **FORWARD**

For A-stubs:

Q=1: Number of decks = 2 plus a matching Pixel in layer A

Q=2: Number of decks > 2

Q=3: Number of decks > 2 + matching Pixel

For BC-stubs:

Q=1: Stub consists of hits in only B or C

Q=2: Stub consists of hits in both layers B and C

Q=3: B+C matches have >0 matching scintillator (pixel) match in B or C

### **A.2.2. Quality for Muons**

## **CENTRAL**

loose: Qual(A) > 0 .OR. Qual(BC) > 0

medium: Qual(A) > 0 .AND. Qual(BC) > 0

tight: Qual(A) > 1 .AND. Qual(BC) > 1

## **FORWARD**

loose: Qual(A) + Qual(BC) > 1

medium: Qual(A) > 0 .AND. Qual(BC) > 0

tight: Qual(A) + Qual(BC) > 3

## Monte Carlo Files (p20)

### B.1. dØrunjob Files

#### ckm\_pythia\_BsMu\_DsPi.py

```
import SAM
params={
  'Global':{
    'runtype':'Monte Carlo',
    'stream':'notstreamed',
    'description':'mixed p20.05.00/p20.09.03 Pythia b+b->incl (require Bs ->Ds(Phi Pi
      )Pi) #DOMESS-EFF=0.02%#)',
    'producedforname':'ralf',
    'phase':'mcp20',
    'groupname':'bphysics',
    'datatier':'reconstructed'
  },
  'Generated':{
    'generator':'pythia',
    'cardfileversion':'v01-01-19',
    'cardfiledir':'ckm',
    'production':'b+b',
    'decay':'incl_sm.n',
    'ptlt':'-1.0',
    'ptgt':'0.0',
    'etalt':'5.0',
    'etagt':'-5.0',
    'd0messprocess':'bs-ds_pi',
    'evtgendecayprocess':'bs-ds-pi',
    'collisionenergy':'1960.0',
    'd0release':'p20.05.00',
    'useevtgen':'on',
    'pdflibfunc':'LHPDFCTEQ6L1',
  },
  'Simulated':{
    'd0release':'p20.09.03',
    'keepparticlecalenergy':'off',
    'geometry':'plate-run2b',
  },
  'Digitized':{
    'numminbi':'1.0',
  }
}
```

```

    'mergeminbias':'on',
    'minbipt':'Fixed',
    'minbidataset' : '
        zerob_p20_09_03_RunIIBMC_online_0sup_only_sample_sept06_shutdown2007_warmcellfix',
        'calorimeternoise':'off',
        'd0release':'p20.09.03',
        'frameworkrcpname':'runD0Sim_noCalNoise_run2b.rcp',
    },
    'Reconstructed':{
        SAM.attrAppFamily:'reconstruction',
        SAM.attrAppName:'d0reco',
        SAM.attrAppVersion:'p20.09.03',
        'd0release':'p20.09.03',
        'frameworkrcpname':'runD0reco_mc.rcp',
    },
}

```

## B.2. d0mess Files

### d0\_mess\_bs-ds\_pi.rcp

```

// Author: Alberto Sanchez
// Modified: V. Jain
// Modified: T. Bose, |eta| < 2.1
// Modified: C. Ay
// Modified: G. Weber
// Purpose: Control rcp for d0_mess event selector
//          Selects events with hadronic decays pi and Ds
//          The muon with pT > 1.5
//          The daughters of the Phi from Ds (K-,K+), will have pT>0.5
//          The Pi from Ds, will have pT>0.5

string PackageName = "d0_mess"

bool d0_mess_on = true

int NumberOfCuts = 8

string Cut1 = "AbsPdgId == 531"
string Cut2 = "AbsPdgId == 13 && Pt > 1.5 && AbsEta < 2.1"
string Cut3 = "AbsPdgId == 431 && AbsParentId == 531"
string Cut4 = "AbsPdgId == 211 && Pt > 1.5 && AbsParentId == 531"
string Cut5 = "AbsPdgId == 211 && Pt > 0.5 && AbsEta < 2.1 && AbsParentId == 431"
string Cut6 = "PdgId == 333 && AbsParentId == 431"
string Cut7 = "PdgId == 321 && Pt > 0.5 && AbsEta < 2.1 && ParentId == 333"
string Cut8 = "PdgId == -321 && Pt > 0.5 && AbsEta < 2.1 && ParentId == 333"

```

## Technical Implementation of the Likelihood

The likelihood fit uses a template method, i.e. theoretical predictions are determined, taking all detector effects into account and finally comparing the experimentally measured value with this theoretical description. The following principle complies to the discussion in Chapter 2. The base distributions for the fits are the probabilities to find opposite sign or same sign events (Equation 2.5). As already discussed it is not possible to measure the true proper decay length of partially reconstructed events. Hence, the  $k$ -Factor (Equation 2.9) has to be taken into account. Its determination is described in Section 7.3.1. It has to be folded into the mixing probabilities. To achieve this, for each bin  $a$  in the histograms  $P^{OS/SS}(t_a)$  all possible values for the true visible proper decay length  $x_i^t = \frac{ct_a}{k_i}$  are constructed

$$P_a(x_i^t) = P(k_i) \times P^{OS/SS}(t_a). \quad (C.1)$$

Afterwards all histograms are summed up at  $x_i^M(t)$

$$P^{OS/SS}(x_i^t) = \sum_{a=t\text{-bins}} P_a(x_i^t). \quad (C.2)$$

Of course, this assumes an infinite resolution of the detector. As this is not the case, the resolution effect is similarly taken into account, like the  $k$ -Factor convolution. Histograms are constructed for all possible values of the measured visible decay length  $x_i^M$

$$P_a(x_i^M) = R(x_i^M - x_a^t; \sigma_{\text{evt}}) \times P(x_a^t). \quad (C.3)$$

In this equation  $\sigma_{\text{evt}}$  is the resolution, determined with the event-by-event scaling factor (Section 7.3.2). Like for the  $k$ -Factor all histograms are summed up

$$P^{OS/SS}(x_i^M) = \sum_{a=X^M\text{-bins}} P_a(x_i^M). \quad (C.4)$$

The background (Section 7.3.3) is taken into account through the signal fraction as a function of the visible proper decay length  $x^M$  and is derived from wrong-sign events

$$P_{\text{tot}}^{OS/SS}(x_i^M) = P^{OS/SS}(x_i^M) / (1 - f_{\text{bg}}(x_i^M)) \quad (C.5)$$

This corrections has to be done, before the efficiency correction, because  $f_{\text{bg}}$  is derived from non-efficiency-corrected events. As the selection efficiency (Section 7.3.4) and the oscillation probability directly rely on  $x^M$  the combination of both is given as

$$P_{\text{eff}}^{\text{OS/SS}}(x_i^M) = P_{\text{tot}}^{\text{OS/SS}}(x_i^M) \times \epsilon(x_i^M). \quad (\text{C.6})$$

These distributions have to be normalized

$$P^{\text{OS/SS}}(x_i^M) = \frac{P_{\text{eff}}^{\text{OS/SS}}(x_i^M)}{\sum_{j=X^m\text{-bins}} P_{\text{eff}}^{\text{OS/SS}}(x_j^M)} \quad (\text{C.7})$$

For an event tagged as opposite-sign, with the measured visible proper decay length  $x^M$  falling into bin  $i$ , the likelihood at  $\Delta m_s$  is

$$\mathcal{L}_{\text{evt}}^{\text{OS}}(x^M) = \frac{P^{\text{OS}}(x_i^M)}{P^{\text{OS}}(x_i^M) + P^{\text{SS}}(x_i^M)}. \quad (\text{C.8})$$

Finally, the visible proper decay length for this specific event is determined as

$$x^M = L_{xy}^B \frac{m(B_s)c}{p_T(B_s)}, \quad (\text{C.9})$$

where  $m(B_s)$  is taken from the PDG [6] and the flight length  $L_{xy}^B$  and the visible transverse momentum  $p_T(B_s)$  are taken from data.

## Bibliography

- [1] E. P. Fischer, *Der Physiker – Max Planck und das Zerfallen der Welt*. Siedler-Verlag, 2007.
- [2] D. N. Spergel *et al.*, “Wilkinson Microwave Anisotropy Probe (WMAP) three year results: Implications for cosmology”, *Astrophys. J. Suppl.*, vol. **170**, p. 377, 2007.
- [3] J. H. Christenson, J. W. Cronin, V. L. Fitch, and R. Turlay, *Phys. Rev. Lett.*, vol. **13**, pp. 138–140, 1964.
- [4] M. Kobayashi and T. Maskawa, *Progress of Theoretical Physics*, vol. **49**, no. 2, pp. 652–657, 1973.
- [5] N. Cabibbo, *Phys. Rev. Lett.*, vol. **10**, no. 12, pp. 531–533, 1963.
- [6] W.-M. Yao, C. Amsler, D. Asner, R. Barnett, Beringer, *et al.*, *Journal of Physics G*, vol. **33**, pp. 1+, 2006.
- [7] O. Schneider, *Phys. Lett.*, vol. **B667**, p. 1, 2008.
- [8] H. Albrecht *et al.*, *Phys. Lett.*, vol. **B192**, p. 245, 1987.
- [9] B. Aubert *et al.*, *Nucl. Instrum. Meth.*, vol. **A479**, pp. 1–116, 2002.
- [10] A. Bondar, *Nucl. Instrum. Meth.*, vol. **A408**, pp. 64–76, 1998.
- [11] M. Okamoto, *POS*, vol. **LAT2005**, p. 013, 2005.
- [12] R. R. Wilson, *Phys. Today*, vol. **30N10**, pp. 23–30, 1977.
- [13] E. Noether, “Invariante Variationsprobleme”, *Nachr. d. König. Gesellsch. d. Wiss. zu Göttingen, Math-phys. Klasse*, 235–257, 1918.
- [14] J. D. Bjorken and E. A. Paschos, *Phys. Rev.*, vol. **185**, no. 5, pp. 1975–1982, 1969.
- [15] R. P. Feynman, *Phys. Rev. Lett.*, vol. **23**, pp. 1415–1417, Dec 1969.
- [16] M. Gell-Mann and Y. Neemam, *The Eightfold Way: a Review with a Collection of Reprints*. Benjamin, 1964.
- [17] S. Abachi *et al.*, *Phys. Rev. Lett.*, vol. **74**, no. 13, pp. 2422–2426, 1995.
- [18] F. Abe *et al.*, *Phys. Rev. Lett.*, vol. **74**, no. 14, pp. 2626–2631, 1995.
- [19] J. Callan, C. G., R. F. Dashen, and D. J. Gross, *Phys. Lett.*, vol. **B66**, p. 375, 1977.
- [20] K. Nishijima, *Progress of Theoretical Physics*, vol. **13**, no. 3, pp. 285–304, 1955.

- [21] M. Gell-Mann, *Nuovo Cim, Suppl*, vol. **4**, no. 848, 1956.
- [22] S. L. Glashow, *Nucl. Phys.*, vol. **22**, pp. 579–588, 1961.
- [23] A. Salam and J. C. Ward, *Nuovo Cim.*, vol. **19**, pp. 165–170, 1961.
- [24] P. W. Higgs, *Phys. Rev. Lett.*, vol. **13**, no. 16, pp. 508–509, 1964.
- [25] L3 Collaboration, *Physics Letters B*, vol. **508**, p. 225, 2001.
- [26] Tevatron New Phenomena, Higgs working group, and for the CDF and DØ collaborations, “Combined CDF and DØ Upper Limits on Standard Model Higgs-Boson Production with up to 4.2 fb<sup>-1</sup> of Data”, *arXiv:hep-ex/0903.4001 (preprint)*, 2009.
- [27] L. Evans and P. Bryant, *Journal of Instrumentation*, vol. **3**, no. 08, p. S08001, 2008.
- [28] F. J. Ynduráin, *Physics Letters B*, vol. **345**, no. 4, pp. 524–526, 1995.
- [29] N. Cabibbo, *Phys. Rev. Lett.*, vol. **10**, no. 12, pp. 531–533, 1963.
- [30] S. L. Glashow, J. Iliopoulos, and L. Maiani, *Phys. Rev.*, vol. **D2**, pp. 1285–1292, 1970.
- [31] J. J. Aubert *et al.*, *Phys. Rev. Lett.*, vol. **33**, no. 23, pp. 1404–1406, 1974.
- [32] J. E. Augustin *et al.*, *Phys. Rev. Lett.*, vol. **33**, no. 23, pp. 1406–1408, 1974.
- [33] S. W. Herb *et al.*, *Phys. Rev. Lett.*, vol. **39**, no. 5, pp. 252–255, 1977.
- [34] L. M. Lederman, *Scientific American*, vol. **239**, no. 4, pp. 60–68, 1978.
- [35] M. A. Shifman, “ITEP Lectures in Particle Physics”, *arXiv:hep-ph/9510397 (preprint)*, 1995.
- [36] M. Bona *et al.*, “First Evidence of New Physics in  $b \leftrightarrow s$  Transitions”, *arXiv:hep-ph/0803.0659v1 (preprint)*, 2008.
- [37] The CKMfitter Group, “<http://ckmfitter.in2p3.fr/>”.
- [38] M. Gell-Mann and A. Pais, *Phys. Rev.*, vol. **97**, no. 5, pp. 1387–1389, 1955.
- [39] K. Lande, E. T. Booth, J. Impeduglia, L. M. Lederman, and W. Chinowsky, *Phys. Rev.*, vol. **103**, no. 6, pp. 1901–1904, 1956.
- [40] K. Lande, L. M. Lederman, and W. Chinowsky, *Phys. Rev.*, vol. **105**, no. 6, pp. 1925–1927, 1957.
- [41] C. Albajar *et al.*, *Phys. Lett. B*, vol. **186**, p. 247, 1987.
- [42] B. Aubert *et al.*, *Phys. Rev. Lett.*, vol. **98**, p. 211802, 2007.
- [43] F. Chlebana, *AIP Conf. Proc.*, vol. **792**, pp. 380–383, 2005.
- [44] B. Andersson, G. Gustafson, G. Ingelman, and T. Sjöstrand, *Phys. Rep.*, vol. **97**, pp. 31–145, 1983.
- [45] C. Peterson, D. Schlatter, I. Schmitt, and P. M. Zerwas, *Phys. Rev. D*, vol. **27**, no. 1, pp. 105–111, 1983.
- [46] D. Buskulic *et al.*, *Phys. Lett. B*, vol. **699**, p. 699, 1995.
- [47] H. Albrecht *et al.*, *Z. Phys.*, vol. **C52**, pp. 353–360, 1991.
- [48] Heavy Flavor Averaging Group, E. Barberio, *et al.*, “Averages of b-hadron Properties at the End of 2005”, *arXiv:hep-ex/0603003 (preprint)*, 2006.
- [49] J. Rademacker, “B physics at CDF”, *arXiv:hep-ex/0406021 (preprint)*, 2004.
- [50] C. Amsler *et al.*, *Phys. Lett.*, vol. **B667**, p. 1, 2008.



- [51] R. J. Barlow, *Nucl. Instrum. Meth.*, vol. **A297**, pp. 496–506, 1990.
- [52] O. Nachtmann and F. Nagel, *Eur. Phys. J.*, vol. **C40**, pp. 497–503, 2005.
- [53] D. Abbaneo and G. Boix, *JHEP08*, vol. **004**, 1994.
- [54] V. M. Abazov *et al.*, *Phys. Rev. Lett.*, vol. **97**, p. 021802, 2006.
- [55] S. Willocq, “ $B_s^0$  Oscillation Results”, *arXiv:hep-ex/0208008v1 (preprint)*, 2002.
- [56] Visual Media Service FNAL, “<http://www-visualmedia.fnal.gov/>”.
- [57] Fermilab Beams Division, “RunII Handbook”, 1998.
- [58] J. Cockcroft and E. Walton, *Proc. R. Soc. London*, vol. **A137**, p. 229, 1932.
- [59] Status of DØ RunII Data Taking, “[http://d0server1.fnal.gov/Projects/Operations/D0RunII\\_DataTaking.htm](http://d0server1.fnal.gov/Projects/Operations/D0RunII_DataTaking.htm)”.
- [60] Status of CDF RunII Data Taking, “[http://www-cdfonline.fnal.gov/ops/opshelp/stores/kumac/store\\_tot.gif](http://www-cdfonline.fnal.gov/ops/opshelp/stores/kumac/store_tot.gif)”.
- [61] DØ Detector Drawings, “<http://www-d0.fnal.gov/Run2Physics/WWW/drawings.htm>”.
- [62] D. Collaboration, *Nucl. Instrum. Meth. A*, vol. **565**, p. 463, 2006.
- [63] M. Weber, *Nucl. Instrum. Meth. A*, vol. **566**, pp. 182–184, 2006.
- [64] W. Cooper, *Nucl. Instrum. Meth. A*, vol. **549**, no. 1-3, pp. 1 – 6, 2005. VERTEX 2003.
- [65] R. C. Ruchti, *Ann. Rev. Nucl. Part. Sci.*, vol. **46**, pp. 281–319, 1996.
- [66] R. Yamada, D. Eartly, J. Ostiguy, H. Jostlein, Y. Antipov, D. Denisov, and S. Chekulaev, *Magnetics, IEEE Transactions on*, vol. **28**, no. 1, pp. 520–523, 1992.
- [67] C. Barnes and R. Jesik, “Level 3 Triggers for  $B_s$  Mixing”, *DØ Note 4272 (internal note)*, 2003.
- [68] DØ Live Event status, “[http://d0.phys.washington.edu/Projects/live\\_event/](http://d0.phys.washington.edu/Projects/live_event/)”.
- [69] S. Snyder, “Coor documentation, <http://www-d0.fnal.gov/d0dist/dist/packages/coor/devel/doc/coorover.ps>”.
- [70] C. Leonidopoulos, “The Muon Trigger at DØ”, *DØ Note 4099 (internal note)*, 2003.
- [71] J. Temple, “Overview of Changes in L1 Muon Logic for Run IIB”, *DØ Note 5165 (internal note)*, 2006.
- [72] C. Barnes, “Development of Vertexing and Lifetime Triggers and a Study of  $B_s$  Mixing Using Hadronic Decays”, *PhD thesis, Imperial College London*, 2005.
- [73] M. Paulini, *Nucl. Phys. Proc. Suppl.*, vol. **120**, pp. 287–294, 2003.
- [74] L. Lueking, “Managing and Serving a Multiterabyte Data Set at the Fermilab DØ Experiment”, *Proceedings of the Fourteenth IEEE Symposium on Mass Storage Systems*, pp. 200–208, 1995.
- [75] DØ Algorithms Group, “<http://www-d0.fnal.gov/computing/algorithms/>”.
- [76] G. Borissov, S. Burdin, and A. Nomerotski, “BANA Analysis Package, [http://d0server1.fnal.gov/users/nomerot/Run2A/B\\_ANA.html](http://d0server1.fnal.gov/users/nomerot/Run2A/B_ANA.html)”.
- [77] H. Greenlee, “The DØKalman Track Fit”, *DØ Note 4303 (internal note)*, 2003.
- [78] M. S. Anzelc and S. Burdin, “Decay Length Resolution Studies: Application to  $B_s^0$  Mixing and p17 Calibration”, *DØ Note 5336 (internal note)*, 2007.
- [79] DØ Runjob project, “<http://www-d0.fnal.gov/computing/d0runjob/docs.html>”.

- [80] M. L. Mangano, M. Moretti, F. Piccinini, R. Pittau, and A. D. Polosa, *JHEP*, vol. **07**, p. 001, 2003.
- [81] T. Sjostrand *et al.*, *Comput. Phys. Commun.*, vol. **135**, pp. 238–259, 2001.
- [82] D. J. Lange, *Nucl. Instrum. Meth.*, vol. **A462**, pp. 152–155, 2001.
- [83] Y. Fisyak and J. Womersley, “DØstar DØ GEANT Simulation of the Total Apparatus Response”, *DØ Note 3191 (internal note)*, 1997.
- [84] R. Brun *et al.*, *CERN DD 78-2*, 1978.
- [85] DØ Collaboration, “DØsim User Manual”, *DØ Note 407 (internal note)*, 1986.
- [86] BANA Skims, “<http://d0server1.fnal.gov/users/nomerot/Run2A/BANA/Dskim.html>”.
- [87] C. Bernius, “Messung der Lebensdauer von B-Mesonen mit dem DØ–Detektor am Tevatron”, *Diplomarbeit, Johannes Gutenberg-Universität Mainz*, 2006.
- [88] C. Bernius, C. Ay, T. Kuhl, S. Tapprogge, and G. Weber, “Reconstruction of  $B_d^0 \rightarrow D^{*-}\pi^+$  Hadron Signals at DØ”, *DØ Note 5161 (internal note)*, 2006.
- [89] R. Brun *et al.*, “<http://root.cern.ch/>”.
- [90] S. Catani, Y. L. Dokshitzer, M. Olsson, G. Turnock, and B. R. Webber, *Phys. Lett.*, vol. **B269**, pp. 432–438, 1991.
- [91] T. Sjostrand, S. Mrenna, and P. Skands, “PYTHIA 6.4 Physics and Manual”, *JHEP*, vol. **05**, p. 026, 2006.
- [92] Trigger Board, “<http://d0trigdb.fnal.gov:8080/trigdb/>”.
- [93] V. M. Abazov *et al.*, “ $B_s$  Mixing in  $B_s \rightarrow D_s \nu, D_s \rightarrow \Phi \pi$  Decay Mode”, *DØ Note 5174-CONF (internal note)*, 2006.
- [94] V. M. Abazov *et al.*, *Phys. Rev. Lett.*, vol. **95**, p. 171801, 2005.
- [95] V. M. Abazov *et al.*, *Phys. Rev.*, vol. **D74**, p. 112002, 2006.
- [96] T. Moulik, “ $B_d$  mixing measurement using opposite side soft electron tagging”, *DØ Note 4822 (internal note)*, 2005.
- [97] H. Akaike, “Information Theory and an Extension of the Maximum Likelihood Principle”, in *International Symposium on Information Theory, 2 nd, Tsahkadsor, Armenian SSR*, pp. 267–281, 1973.
- [98] S. Lami, “Underlying Event Studies at CDF”, *arXiv:hep-ex/0311027 (preprint)*, 2003.
- [99] G. Borrisov, S. Burdin, and A. Nomerotski, “Measurement of Lifetime Ratio for Charged and Neutral B Mesons”, *DØ Note 4280 (internal note)*, 2003.
- [100] J. Radigan and W. Taylor, “The  $k$ -Factor in Semileptonic  $B_s$  Decays using the  $D_s^- \rightarrow \phi \pi^-$  Decay Mode”, *DØ Note 5221 (internal note)*, 2006.
- [101] G. Borrisov and A. Rakitin, “Flavor Tagging Technique for  $B_s$  Mesons”, *DØ Note 5210, v5 (internal note)*, 2006.
- [102] J. Abdallah *et al.*, *Eur. Phys. J.*, vol. **C32**, pp. 185–208, 2004.
- [103] T. M. P. Baringer, D. Coppage, “Central Preshower validation and Soft Electron Identification”, *DØ Note 4920 (internal note)*, 2005.
- [104] M. Battaglia *et al.*, “The CKM Matrix and the Unitarity Triangle”, *arXiv:hep-ph/0304132 (preprint)*, 2003.

- [105] M. Anzelc, C. Ay, G. Borissov, S. Burdin, H. Evans, R. Jesik, T. Moulik, A. Nomerotski, P. Lewis, D. Strom, W. Taylor, D. Tsybychev, and R. van Kooten, “A Study of Mixing in the Bs System Using the Bs to DsMuX, Ds to PhiPi Decay Mode, Opposite-Side Flavor Tagging and Unbinned Fit”, *DØ Note 5045 (internal note)*, 2006.
- [106] M. Anzelc, S. Beale, G. Borissov, S. Burdin, H. Evans, T. Kuhl, T. Moulik, M. Naimuddin, J. Radigan, A. Rakitin, W. Taylor, D. Tsybychev, G. Weber, and S. Youn, “Measurement of Flavor Oscillation Frequency of  $B_s^0$  Mesons at D0”, *DØ Note 5474 (internal note)*, 2007.
- [107] M. Anzelc, S. Beale, G. Borissov, S. Burdin, H. Evans, D. Krop, T. Kuhl, T. Moulik, M. Naimuddin, A. Rakitin, W. Taylor, D. Tsybychev, R. V. Kooten, G. Weber, and S. Youn, “ $DØB_s^0$  Oscillation Combination for Summer 2007”, *DØ Note 5618 (internal note)*, 2008.
- [108] A. Abulencia *et al.*, *Phys. Rev. Lett.*, vol. **97**, p. 242003, 2006.
- [109] M. Bona, M. Ciuchini, E. Franco, V. Lubicz, G. Martinelli, F. Parodi, M. Pierini, C. Schiavi, L. Silvestrini, V. Sordini, A. Stocchi, C. Tarantino, and V. Vagnoni, “<http://www.utfit.org/>”.
- [110] V. Vagnoni, “LHCb Impact on CKM fits”, *Proceedings on the 4th Workshop on the CKM Unitarity Triangle (CKM2006)*, 2006.
- [111] J. Radigan and W. Taylor, “The K Factor in Semileptonic  $B_s$  Decays Using the  $D_s \rightarrow \Phi\pi$  Decay Mode”, *DØ Note 5221 (internal note)*, 2006.
- [112] T. A. Collaboration, G. Aad, *et al.*, *Journal of Instrumentation*, vol. **3**, no. 08, p. S08003, 2008.
- [113] T. C. Collaboration, S. Chatrchyan, *et al.*, *Journal of Instrumentation*, vol. **3**, no. 08, p. S08004, 2008.
- [114] The LHCb Collaboration, A. A. A. Jr, *et al.*, “The LHCb Detector at the LHC”, *Journal of Instrumentation*, vol. **3**, no. 08, p. S08005, 2008.
- [115] G. Sciolla, *Nucl. Phys. Proc. Suppl.*, vol. **156**, pp. 16–20, 2006.
- [116] T. Gershon, “On the Measurement of the Unitarity Triangle Angle Gamma from  $B^0 \rightarrow DK^{*0}$  Decays”, *arXiv:hep-ph/0810.2706 (preprint)*, 2008.
- [117] T. Browder *et al.*, *JHEP*, vol. **02**, p. 110, 2008.



## List of Figures

1.1. Symmetries in nature . . . . .	4
1.2. Higgs potential . . . . .	8
1.3. Unitarity triangles . . . . .	12
1.4. Unitarity triangle from the CKM fitter group . . . . .	13
1.5. ARGUS event display, showing $B_s\bar{B}_d$ mixing . . . . .	14
1.6. Feynman graphs for $B_{d,s}^0\bar{B}_{d,s}^0$ mixing . . . . .	14
1.7. Comparing the mixing frequency of $B_d$ and $B_s$ mesons . . . . .	16
1.8. $b\bar{b}$ quark production in leading order . . . . .	18
1.9. $b\bar{b}$ quark production at next-to-leading order level . . . . .	18
1.10. Hadronization . . . . .	19
2.1. Signal topology $B_s \rightarrow \pi D_s(\phi\pi)X$ . . . . .	22
2.2. Oscillation probabilities with $k$ -Factor, resolution and selection efficiency . . . . .	24
2.3. Loglikelihood fit . . . . .	26
2.4. Amplitude Scan . . . . .	27
3.1. View of the Fermilab Tevatron Collider . . . . .	30
3.2. Integrated luminosity accumulated with the DØ detector . . . . .	32
3.3. Schematic view of the DØ detector . . . . .	32
3.4. Magnified view of the DØ tracking system . . . . .	33
3.5. 3-d view of the SMT . . . . .	34
3.6. Performance of Layer0 . . . . .	35
3.7. Front view of CFT fibers . . . . .	36
3.8. Illustration of the DØ muon system . . . . .	37
3.9. Time resolution and detection eff. of muon trigger scintillation counters . . . . .	38
4.1. $B_d$ decay and minimum bias $p_T$ spectra Monte Carlo . . . . .	40
4.2. DØ event display . . . . .	40
4.3. Three level trigger system . . . . .	41
4.4. Level 1 and Level 2 trigger flowchart . . . . .	42
4.5. Overview of the central track trigger . . . . .	42
4.6. Level 3 flowchart . . . . .	44

4.7. Trigger rates for all three trigger levels . . . . .	45
4.8. Level 2 muon trigger studies . . . . .	48
4.9. Level 3 impact parameter trigger studies . . . . .	50
5.1. Functional principle of the track hypothesis of the AA tracking algorithm . . . . .	53
5.2. Particle track projection into $x$ - $y$ and $r$ - $z$ plane . . . . .	53
6.1. Distributions for the $\phi$ candidate selection . . . . .	62
6.2. Distributions for the $D_s^-$ candidate selection . . . . .	63
6.3. Distributions for the $B_s$ candidate selection . . . . .	64
6.4. Definition of the signal and background regions for the likelihood selection optimization	67
6.5. Distribution of the helicity angle variable . . . . .	68
6.6. Distribution of the isolation variable . . . . .	68
6.7. Distribution of the transverse momentum of the $\phi$ candidate . . . . .	68
6.8. Distribution of the $\chi^2$ of the fit for the $D_s^-$ . . . . .	69
6.9. The invariant mass of the $\phi$ meson . . . . .	69
6.10. Likelihood distribution . . . . .	70
6.11. Impact of the likelihood selection (RunIIa) . . . . .	70
6.12. Impact of the likelihood selection (RunIIb) . . . . .	70
6.13. Plots of the invariant $K^+K^-\pi^+\pi^-$ mass. . . . .	71
6.14. Plots of the invariant $K^+K^-\pi^+\pi^-$ mass with Monte Carlo. . . . .	72
6.15. Comparison of the background decay channels . . . . .	75
7.1. Principle of lifetime measurement . . . . .	78
7.2. $k$ -Factor distributions . . . . .	80
7.3. Background distributions . . . . .	82
7.4. Selection efficiency vs. the visible proper decay length . . . . .	83
7.5. Lifetime measurement Monte Carlo . . . . .	83
7.6. Lifetime measurement $B_d$ . . . . .	84
7.7. Lifetime measurement $B_s$ . . . . .	84
8.1. Invariant $K\pi$ masses for the $D^0$ and $D^*$ candidates . . . . .	90
8.2. Normalized distributions of tagging methods . . . . .	91
8.3. Distribution of the combined tagging variable $d$ . . . . .	91
9.1. Dilution calibration curve . . . . .	94
9.2. Likelihood Fit for $B_d$ Monte Carlo . . . . .	95
9.3. Likelihood Fit for $B_s$ Monte Carlo . . . . .	96
9.4. Likelihood Fits for hadronic $B_d$ decays . . . . .	97
9.5. Likelihood Fits for hadronic $B_s$ decays . . . . .	98
9.6. Dilution calibration curve . . . . .	99
9.7. Amplitude scan for $B_d$ mesons . . . . .	101
9.8. Amplitude scan for $B_s$ mesons . . . . .	102
10.1. Comparison of the obtained $\Delta m_s$ results with existing measurements . . . . .	105
10.2. Evolution of the unitarity triangle . . . . .	105

## List of Tables

1.1. Fermion table . . . . .	5
1.2. Overview of mesons . . . . .	10
1.3. Production cross section of $b\bar{b}$ pairs . . . . .	17
3.1. Typical parameters for the Tevatron in RunII. . . . .	31
3.2. Overview of the components of the silicon microstrip tracker . . . . .	34
3.3. Number of fibers and location of all eight layers of the CFT . . . . .	36
4.1. Level 1 muon trigger studies. . . . .	47
4.2. Level 2 muon trigger studies. . . . .	48
4.3. Level 3 triggers. . . . .	49
4.4. Level 3 trigger efficiencies . . . . .	50
5.1. Overview of muon qualities . . . . .	55
5.2. Generated Monte Carlo samples for $B_d$ decay studies . . . . .	56
5.3. Generated Monte Carlo samples for $B_s$ decay studies . . . . .	56
5.4. Collected events in data sample . . . . .	57
6.1. Preselection cuts $B_s$ . . . . .	66
6.2. RunIIa, RunIIb data and Monte Carlo event selection summary . . . . .	72
6.3. Events passing the final selection. . . . .	72
6.4. Preselection cuts $B_d$ . . . . .	74
6.5. Events passing the final selection . . . . .	74
7.1. Fitting parameters for the k-Factor . . . . .	81
7.2. Fitting parameters for the background fraction . . . . .	81
7.3. Overview of the fitting parameters for the selection efficiency . . . . .	82
7.4. Systematic uncertainties of the lifetime fit . . . . .	85
9.1. Fitting parameters for the dilution calibration curve . . . . .	94
9.2. Systematic uncertainties of the Likelihood Fit . . . . .	99
9.3. $\Delta m_d$ Systematic uncertainties from the Amplitude Scan . . . . .	101
9.4. $\Delta m_s$ Systematic uncertainties from the Amplitude Scan . . . . .	102





## Acknowledgements

It takes a long time to write a PhD thesis, though not as long as it takes to build the Tevatron, surprisingly. I would here like to express my thanks to the people who have been very helpful to me during the time it took me to write this thesis.

This thesis would not have been possible without the help, support and patience of my principal supervisor, Prof. Stefan Tapprogge, not to mention his advice and unsurpassed knowledge. Most of the times his ideas and helpful suggestions helped me out of hopeless situations. Of course, this all would have not been possible without Konrad Kleinknecht. He founded our well established group several years ago and it was always very interesting (and sometimes funny) to listen to his stories about the incipencies of particle physics. Furthermore, I would like to thank Thorsten Kuhl for the constant reminders and the help with my analysis. Our secretary, Silvia Müller had always the right encouraging words on bad days. A special thanks has to go to Marius Groll – I made him to read my thesis so often, that he probably knows it better, than I do. Also the rest of the DØ Mainz group Catrin Bernius and Cano Ay provided me with input for my thesis and made sure of a good atmosphere in our office. Additionally, I bugged so many people, who never hesitated to read my thesis. Marc Hohlfeld as DØ trigger expert, Rainer Wanke with his unbeatable knowledge on  $B$  mixing (this might be related to his PhD thesis...) and Mohammed Aharrouche. I shared my office with Stefan Rieke for quite a long time – he made some non-workable days go by. Rainer Othegraven always made me laugh, when I had to struggle again with our printers.

Of course, also my international colleagues at DØ were very helpful and made my stay at Fermilab enjoyable. Particularly, the whole  $B$  physics group provided me with much valuable input. Additionally, they spent the confidence in me to present our results at very reputational events, like the CKM workshop in Nagoya (Japan) and Moriond (Italy). But I would like to name a few persons personally. During the last few months I gained a lot from the experience and knowledge of Hal Evans. I'm not sure, whether I would have been able to get the “lifetime fit” working without his help. Furthermore, he was willing to read throughout my thesis as a native speaker. Brendan Casey's expert judgement was really helpful, when our results had to make it through the editorial board at DØ. Guennadi Borissov and Sergey Burdin provided me with so much background knowledge about the  $B$  physics framework. Whenever there was a question – they knew the answer. Rick Jesik and Marco Verzocchi were very supportive during my trigger studies.

But I must admit, that I didn't spend all day in the office and I made many good friends. I'm still in contact with Andreas Wenger, with whom I had a lot of fun during the weekends and in fact, he was even a roomie to me for a short time, when I moved to Switzerland after my time in Mainz. Su-Jung and Olav Mundal and the never forgetable Tirmasu-contest. Next time I'm going to beat you ;) Matthias Kirsch is still a valuable friend to me. But I would also like to mention the main actor of "Die kalte Wut des Makalu" – Christian Schwanenberger. You should have received an Oscar for this. Björn Penning – he never refused to look after our computers, when everybody else already left Fermilab and Alexander Grohsjean – you should have come to Mainz, though. Furthermore, I would like to say a big thank you to Daniel Neeb. I know him for almost all the time of my studies and we had quite a few funny times (even, when preparing for our diploma exams). He was and is always a good counsel – especially in non-physics questions... The list is not at an end for a long time yet, as I have been fortunate to come across many funny and good friends, without whom life would be bleak. My dearest friends Jan Dehoust and Bertrand Straub. Jan, I can always count on you and you helped me through difficult times. Berti, I'm so glad, that we finally work in the same city again. Last, but by no means least, I would like to thank my girl-friend Andrea. She had to put up with all my moods during the last couple of months and always found a way to cheer me up, when I was frustrated about the status of my thesis.

For my family it is not just a thank you. In fact, I would like to dedicate this thesis to you. My brother Gunther, who encouraged me to study physics and to go for my PhD. My dad, who was so supportive during my whole life to the last extends and my mother, who lost her fearless fight against breast cancer much to early. I can't think of a better family.

I'm sure there are more people who need thanking, and one day – I'm sure I'll get around to it. For any errors or inadequacies that may remain in this work the responsibility is entirely, of course, my own.

Like the swiss people tend to say: "Merci vielmal".

A handwritten signature in blue ink, reading "Gunter A. Voth". The signature is stylized, with the first name "Gunter" written in a cursive script and the last name "Voth" in a more upright, blocky style.

# CURRICULUM VITAE

## CONTACT INFORMATION

---

Gernot A. Weber  
Bergstr. 8a  
8953 Dietikon  
Switzerland  
Tel.: +41 78 770 4847  
email: gernot.weber@quantumnet.de

## EDUCATION

---

- since 10/2008      **Analyst engineer in gas turbine research and development**  
at Alstom Switzerland AG
- since 08/2004      **Ph. D. student**  
at the “Johannes Gutenberg-Universität Mainz”,  
“Measurement of the Mixing Frequency of  $B_s$  Mesons Through the Hadronic Decay  
Mode  $B_s \rightarrow \pi D_s(\phi\pi)X$  with the DØ Detector at the Fermilab Tevatron Collider”
- 12/2003      **Graduation**, Grade: 1,6
- 10/2002 - 12/2003      **Diploma thesis:** “Erstellung eines Datenaufnahmesystems für das  
Compton-Polarimeter”, Grade: 1,3
- 10/1997 - 12/2003      Studies in **physics** at the “Johannes Gutenberg-Universität Mainz”

## RESEARCH PERIODS

---

- 10/2005 - 06/2006      **Fermilab, Chicago, IL, USA**  
Research at the Fermilab Tevatron Collider for the DØ experiment
- 08/2004 - 10/2004      **CERN, Geneva, Switzerland**  
Testbeam measurements for the ATLAS collaboration at CERN

## CONFERENCES

---

- 03/2008      Annual conference of the “Deutsche Physikalische Gesellschaft” (German Physical  
Society), Freiburg, Germany  
– Hadronische  $B_s$ -Zerfälle bei DØ
- 03/2008      Rencontres de Moriond – QCD and High Energy Interactions, La Thuile, Italy  
– Measurements of  $B_s$  Oscillations at the Tevatron

- 03/2007      Annual conference of the “Deutsche Physikalische Gesellschaft” (German Physical Society), Heidelberg, Germany  
                  – Messung der  $B_s$ -Oszillationsfrequenz  $\Delta m_s$  mit dem DØ-Detektor
- 12/2006      CKM Workshop 2006, Nagoya, Japan  
                  – DØ-Results on Neutral B Meson Flavor Oscillations  
                  –  $\Delta\Gamma$  and  $\phi_s$  at Tevatron (on behalf of Brendan Casey)
- 04/2006      American Physical Society, Dallas, TX, USA  
                  – Hadronic Decays for the  $B_s$  Oscillation Measurement at DØ  
                  – A Precise Measurement of the  $B_s^0$  Lifetime (on behalf of Alberto Sanchez)
- 03/2006      Annual conference of the “Deutsche Physikalische Gesellschaft” (German Physical Society), Dortmund, Germany  
                  – DØ-Trigger für hadronische  $B_s$ -Zerfälle
- 03/2005      Annual conference of the “Deutsche Physikalische Gesellschaft” (German Physical Society), Berlin, Germany  
                  – Einsatz des Level-1 Calorimeter Triggers Jet/Energiesummen Moduls bei ATLAS Testmessungen am CERN

## PUBLICATIONS

---

- 2007      The DØ Collaboration, “(Combined) Measurement of the Flavor Oscillation Frequency of  $B_s$  Mesons”, DØnote 5474-conf
- 2006      R. Achenbach *et al.*, “Pre-production validation of the ATLAS level-1 calorimeter trigger system”, IEEE Trans. Nucl. Sci. **53** (2006) 859

Dietikon, March 31, 2009

